2-6-2017

The Dusty Tori of Nearby QSOs as Constrained by High-Resolution Mid-IR Observations

M. Martínez-Paredes
Instituto Nacional de Astrofísica, Mexico

I. Aretxaga
Instituto Nacional de Astrofísica, Mexico

A. Alonso-Herrero
Centro de Astrobiología, Spain

O. González-Martín
Instituto de Radioastronomía y Astrofísica, Mexico

E. Lopéz-Rodríguez
NASA Ames Research Center

See next page for additional authors

Monthly Notices of the ROYAL ASTRONOMICAL SOCIETY

MNRAS **468,** 2–46 (2017) doi:10.1093/mnras/stx307
Advance Access publication 2017 February 6

The dusty tori of nearby QSOs as constrained by high-resolution mid-IR observations

M. Martínez-Paredes,[1,2★] I. Aretxaga,[1] A. Alonso-Herrero,[3,4,5] O. González-Martín,[2] E. Lopéz-Rodríguez,[6,7,8] C. Ramos Almeida,[9,10] A. Asensio Ramos,[9,10] T. Diaz Santos,[11] M. Elitzur,[12,13] P. Esquej,[3] A. Hernán-Caballero,[14] K. Ichikawa,[5,15] R. Nikutta,[16] C. Packham,[5] M. Pereira-Santaella[17] and C. Telesco[18]

[1]*Instituto Nacional de Astrofísica, Óptica y Electrónica (INAOE), Luis Enrique Erro 1, Sta. Ma. Tonantzintla, Puebla, Mexico*
[2]*Instituto de Radioastronomía y Astrofísica UNAM, Apartado Postal 3-72 (Xangari), 58089 Morelia, Michoacán, Mexico*
[3]*Centro de Astrobiología (CAB, CSIC-INTA), ESAC Campus, E-28692 Villanueva de la Cañada, Madrid, Spain*
[4]*Department of Physics, University of Oxford, Oxford OXI 3RH, UK*
[5]*Department of Physics and Astronomy, University of Texas at San Antonio, San Antonio, TX 78249, USA*
[6]*SOFIA/USRA, NASA Ames Research Center, Moffett Field, CA 94035, USA*
[7]*Department of Astronomy, University of Texas at Austin, 1 University Station C1400, Austin, TX 78712, USA*
[8]*McDonald Observatory, University of Texas at Austin, Austin, TX 78712, USA*
[9]*Instituto de Astrofísica de Canarias (IAC), E-38205 La Laguna, Tenerife, Spain*
[10]*Departamento de Astrofísica, Universidad de La Laguna, E-38206, Tenerife, Spain*
[11]*Núcleo de Astronomía de la Facultad de Ingenería, Universidad Diego Portales, Av. Ejército Libertador 441, Santiago, Chile*
[12]*Astronomy Department, University of California, Berkeley, CA 94720, USA*
[13]*Physics & Astronomy, University of Kentucky, Lexington, KY 40506, USA*
[14]*Departamento de Astrofísica, Facultad de CC. Físicas, Universidad Complutense de Madrid, E-28040 Madrid, Spain*
[15]*National Astronomical Observatory of Japan, 2-21-1 Osawa, Mitaka, Tokyo 181-8588, Japan*
[16]*National Optical Astronomy Observatory, 950 N Cherry Ave, Tucson, AZ 85719, USA*
[17]*Department of Physics, University of Oxford, Keble Road, Oxford OX1 3RH, UK*
[18]*Department of Astronomy, University of Florida, Gainesville, FL 32611, USA*

Accepted 2017 February 1. Received 2017 February 1; in original form 2016 November 9

ABSTRACT

We present mid-infrared (MIR; 7.5–13.5 μm) imaging and spectroscopy observations obtained with the CanariCam (CC) instrument on the 10.4-m Gran Telescopio CANARIAS for a sample of 20 nearby, MIR bright and X-ray luminous quasi-stellar objects (QSOs). We find that for the majority of QSOs the MIR emission is unresolved at angular scales ∼0.3 arcsec, corresponding to physical scales $\lesssim$600 pc. We find that the higher-spatial resolution CC spectra have similar shapes to those obtained with *Spitzer/IRS*, and hence we can assume that the spectra are not heavily contaminated by extended emission in the host galaxy. We thus take advantage of the higher signal-to-noise ratio *Spitzer/IRS* spectra, as a fair representation of the nuclear emission, to decompose it into a combination of active galactic nuclei (AGN), polycyclic aromatic hydrocarbon (PAH) and stellar components. In most cases, the AGN is the dominant component, with a median contribution of 85 per cent of the continuum light at MIR (5–15 μm) within the *IRS* slit. This IR AGN emission is well reproduced by CLUMPY torus models. We find evidence for significant differences in the parameters that describe the dusty tori of QSOs when compared with the same parameters of Seyfert 1 and 2 nuclei. In particular, we find a lower number of clouds ($N_0 \lesssim 12$), steeper radial distribution of clouds ($q \sim 1.5$–3.0) and clouds that are less optically thick ($\tau_V \lesssim 100$) than in Seyfert 1, which could be attributed to dusty structures that have been partially evaporated and piled up by the higher radiation field in QSOs. We find that the combination of the angular width $\sigma_{\rm torus}$, viewing angle i, and number of clouds along the equatorial line, N_0, produces large escape probabilities ($P_{\rm esc} > 2$ per cent) and low geometrical covering factors ($f_2 \lesssim 0.6$), as expected for AGN with broad lines in their optical spectra.

Key words: galaxies: active – quasars: general – infrared: galaxies.

★ E-mail: m.martinez@crya.unam.mx

1 INTRODUCTION

The dusty torus (e.g. Rowan-Robinson 1977; Krolik & Begelman 1988) is the cornerstone of the unified scheme for active galactic nuclei (AGN; e.g. Antonucci 1993; Urry & Padovani 1995). This framework attributes the differences between type 1 and type 2 AGN to the orientation of a putative dusty torus that surrounds the central engine around the supermassive black hole. Type 1 AGN show broad permitted optical emission lines [with full-width at half-maxima (FWHM) $\sim 10^3 - 10^4$ km s^{-1}] and narrow permitted and forbidden emission lines (FWHM $\sim$ 500 km s^{-1}), while type 2 AGN only show permitted and forbidden narrow emission lines (FWHM $\sim$ 400–500 km s^{-1}), as the broad line region is obscured by the torus under this framework. The torus absorbs the emission of the central engine and re-radiates it in the mid-infrared (MIR), such that at $\sim$5–35 μm it is the dominant component (e.g. Urry & Padovani 1995; Urry 2003; Packham et al. 2005; Radomski et al. 2008). Hence the shape of the MIR spectral energy distribution (SED) depends crucially on the configuration, providing a clean insight into its geometry and composition. If the dust is homogeneously distributed in the torus, the IR emission that arises from the inner region of the torus (hot and optically thin region) should be larger than the emission observed through the torus, which is optically thick, resulting in a steeper SED (e.g. Pier & Krolik 1992; Granato & Danese 1994; Efstathiou & Rowan-Robinson 1995). On the other hand, if the dust is in a clumpy distribution of optically thick clouds that do not fill all the volume, then the dependence of the luminosity with the viewing angle decreases and the SED becomes flatter (e.g. Nenkova et al. 2008a,b; Stalevski et al. 2012). However, Feltre et al. (2012), in a detailed comparison of smooth and clumpy models, find that both configurations can predict similar MIR continuum shapes for different model parameters, but their predicted NIR slopes are different.

MIR observations acquired with 8-m-class ground-based telescopes provide high spatial resolution data ($\lesssim$0.3 arcsec) crucial to isolate the emission of the dusty torus and the AGN from its host (e.g. Krabbe, Böker & Maiolino 2001; Horst et al. 2006, 2008; Mason et al. 2006; Gandhi et al. 2009; Levenson et al. 2009). During the last decades these MIR observations have constrained the spatial extension of tori in nearby Seyfert galaxies to be $\lesssim$5 pc (e.g. Jaffe et al. 2004; Packham et al. 2005; Tristram et al. 2007; Radomski et al. 2008), giving support to models where the torus is fragmented into clouds that form a clumpy obscuring medium.

One of the largest sample of Seyfert galaxies studied so far with ground-based MIR observations suggests that their classification as type 1 or 2 does not only depend on the viewing angle but also on the intrinsic geometry of the cloud distribution (e.g. Ramos Almeida et al. 2009, 2011; Alonso-Herrero et al. 2011; Mateos et al. 2016). In a previous work, Ichikawa et al. (2015) studied a sample of type 1 and 2 Seyfert galaxies, with and without the signs of broad polarized lines, and found that the intrinsic properties of the tori are also intrinsically different. In a recent study, García-Burillo et al. (2016) modelled the torus in the nearby Seyfert galaxy NGC1068 using ALMA plus nuclear NIR and MIR data. They found that the nuclear emission at submillimetre wavelengths (432 μm) is consistent with a clumpy distribution of the dust.

While much effort has been devoted to characterize the dusty torus of Seyfert galaxies using high angular resolution data (e.g. Hönig et al. 2010; Alonso-Herrero et al. 2011; Ramos Almeida et al. 2011; Ichikawa et al. 2015) and low angular resolution data (e.g. Lutz et al. 2004; Schweitzer et al. 2006; Ramos Almeida et al. 2007; Ichikawa et al. 2012; González-Martín et al. 2015), the study of the dusty torus in quasi-stellar objects (QSOs) has been limited to low resolution data ($\sim$3 arcsec; e.g. Mor, Netzer & Elitzur 2009; Nikutta, Elitzur & Lacy 2009; Mateos et al. 2016; Ichikawa et al. 2017). This is mainly due to their compactness and sparseness in the local Universe. The point-like morphology of QSOs does not allow us to disentangle the extended emissions from the host galaxy in the immediate vicinity of the central engine, which can be an important contaminant that impacts greatly the results on the properties of the torus. Therefore, MIR high angular resolution observations offer a good opportunity to step forward in their understanding.

Previous studies in the IR reveal that the majority of Palomar-Green (PG) QSOs (Green, Schmidt & Liebert 1986) present signs of a recent galactic interaction (e.g. Veilleux et al. 2009a) and show polycyclic aromatic hydrocarbon (PAHs) emission in the *Spitzer/IRS* spectrum (Schweitzer et al. 2006) indicating the presence of starbursts at scales of a few kpc for the nearest objects ($z < 0.1$). Moreover, it is also well known that these objects present prominent 10 μm silicate emission features, suggesting the presence of a dusty torus. Although, it is not entirely clear whether all this emission actually arises from the inner regions of a face-on torus or whether part of it comes from an extended silicate region towards the Narrow Line Region (NLR) (Netzer 2008). The study of the IR emission in this class of AGN requires a complex combination of components (e.g. a combination of the torus, NLR and/or starburst). Some works have also included an additional component of hot dust emission from the inner region of the torus in order to find a successful SED fitting of large aperture observations, especially between 1 and 8 μm (e.g. Schweitzer et al. 2008; Hönig et al. 2010; Mor & Netzer 2012).

In this work we present MIR high angular (0.3–0.4 arcsec) resolution imaging and spectroscopy obtained with CanariCam (CC; Telesco et al. 2003; Packham et al. 2005) in the 10.4-m Gran Telescopio CANARIAS (GTC) of a sample of 20 nearby QSOs, with the aim to constrain the geometrical parameters of their dusty tori and compare them with those found in Seyfert galaxies that have been studied with similar techniques. In Section 2 we present the QSO sample. In Section 3 we show our new high angular resolution observations and in Section 4 the ancillary data we will use in the modelling. Section 5 presents some basic analysis of the data; in Section 6 we present the spectral decomposition into AGN and starburst components, and in Section 7 we perform spectral fitting of the unresolved IR SED and MIR spectroscopy using CLUMPY models. We discuss the main results in Section 8.2 and our conclusions are given in Section 9. We adopt a cosmology with $H_0 = 73$ km s^{-1} Mpc^{-1}, $\Omega_M = 0.27$ and $\Omega_\Lambda = 0.73$.

2 THE SAMPLE

We select a representative sample of 20 X-ray luminous and MIR-bright nearby QSOs from the latest version of the Véron-Cetty & Véron (2010) catalogue and the NASA/IPAC Extragalactic Database[1] (NED), that meet the following criteria: (1) redshift $z < 0.1$ to obtain a minimum spatial scale of $\sim$1.8 kpc arcsec^{-1}, so that for our projected nearly difraction-limited observations ($\lesssim$0.3 arcsec) we sample spatial scales $\lesssim$600 pc; (2) flux density at N band $f_N > 0.02$ Jy to be able to detect them with CC on the 10.4 m GTC; and (3) intrinsic X-ray luminosity $L_{X(2-10keV)} > 10^{43}$ erg s^{-1}, to focus on the most powerful AGN.

[1] https://ned.ipac.caltech.edu/

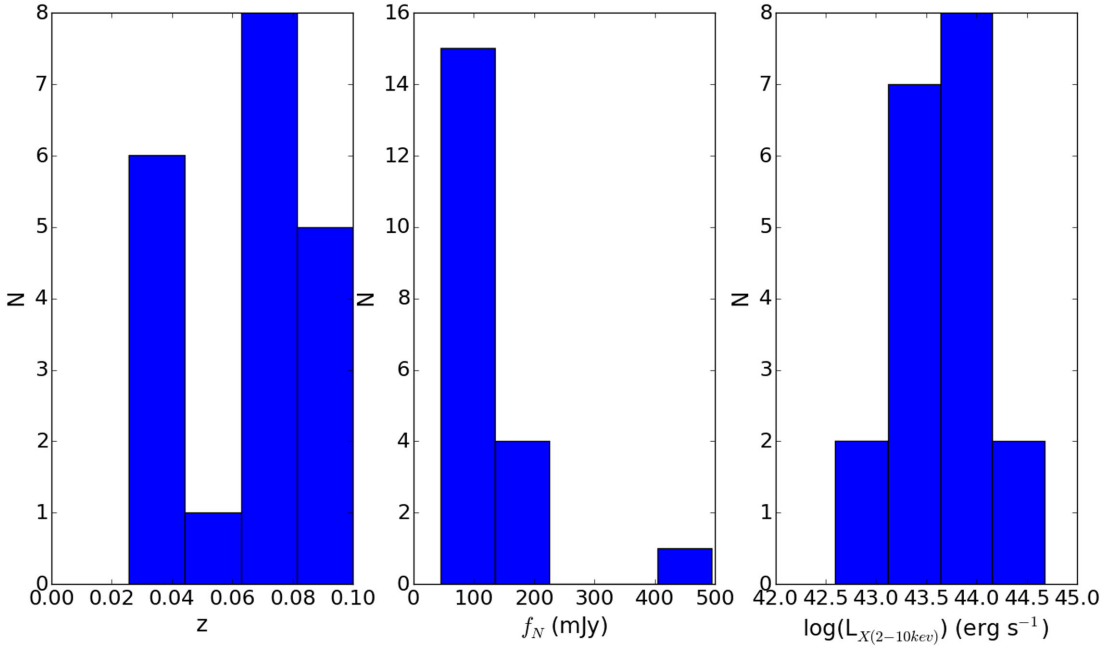

Figure 1. From left to right, distributions of redshift, *N*-band flux-density and 2–10 keV X-ray luminosity for the QSOs in our sample.

Table 1. QSO sample. Column 1 gives the name and classification as type 1, 2 or narrow-line type 1 (NL1) AGN; columns 2 and 3 the coordinates in right ascension and declination; columns 4, 5 and 6 the redshift, angular scale and the comoving radial distance; column 7 the absolute magnitude; column 8 the radio classification as radio-quiet (Q) or radio-loud (L) AGN, and column 9 the hard X-ray (2–10 kev) luminosity.

Name (AGN-type)	RA (2000) (h:m:s)	Dec. (2000) (h:m:s)	z^a	Scale (kpc arcsec^{-1})	d (Mpc)	M_V^b (mag)	Radio^c	$L^e_{\rm X(2-10keV)}$ (erg s^{-1})
PG 0003+199/Mrk 335 (1)	00:06:19.5	20:12:10	0.03	0.498	122	−19.0	Q^{d1}	1.9×10^{43}
PG 0007+106/Mrk 1501 (1.2)	00:10:31.0	10:58:30	0.09	1.602	363	−22.9	L^{d2}	$1.4^{e1} \times 10^{44}$
PG 0050+124/IZw1 (1)	00:53:34.9	12:41:36	0.06	1.094	243	−22.7	Q	7.1×10^{43}
PG 0804+761 (1)	08:10:58.6	76:02:43	0.10	1.772	402	−23.2	Q	2.9×10^{44}
PG 0844+349 (1)	08:47:42.4	34:45:04	0.06	1.182	243	−22.4	Q	5.5×10^{43}
PG 0923+129/Mrk 705 (1.2)	09:26:03.3	12:44:04	0.03	0.562	122	−20.9	Q^{d3}	$2.6^{e2} \times 10^{43}$
PG 1211+143 (NL1)	12:14:17.7	14:03:13	0.08	1.465	323	−23.3	Q	5.0×10^{43}
PG 1229+204/Mrk 771 (1)	12:32:03.6	20:09:29	0.06	1.165	243	−20.0	Q	3.1×10^{43}
PG 1351+640 (1.5)	13:53:15.7	63:45:46	0.09	1.584	363	−23.3	Q	$1.2^{e3} \times 10^{43}$
PG 1411+442 (1)	14:13:48.3	44:00:14	0.09	1.607	363	−23.9	Q	2.5×10^{43}
PG 1426+015/Mrk 1383 (1)	14:29:06.6	01:17:06	0.09	1.558	363	−22.7	Q	1.3×10^{44}
PG 1440+356/Mrk 478 (NL1)	14:42:07.4	35:26:23	0.08	1.436	323	−22.7	Q	5.8×10^{43}
PG 1448+273 (NL1)	14:51:08.8	27:09:27	0.07	1.199	283	−22.2	Q^{d4}	2.0×10^{43}
PG 1501+106/Mrk 841 (1.5)	15:04:01.2	10:26:16	0.04	0.694	163	−20.9	Q^{d5}	7.8×10^{43}
PG 1534+580/Mrk 290 (1.5)	15:35:52.3	57:54:09	0.03	0.569	122	−18.5	Q^{d1}	1.8×10^{43}
PG 1535+547/Mrk 486 (1)	15:36:38.3	54:33:33	0.04	0.740	163	−20.8	–	$4.0^{e4} \times 10^{42}$
PG 2130+099/IIZw136 (1.5)	21:32:27.8	10:08:19	0.06	1.165	243	−18.5	Q	3.2×10^{43}
PG 2214+139/Mrk 304 (1)	22:17:12.2	14:14:21	0.07	1.213	283	−22.3	Q	6.6×10^{43}
Mrk 509 (1.5)	20:44:09.7	−10:43:25	0.03	0.657	122	−22.5	Q^{d4}	4.8×10^{44}
MR 2251−178 (1.5)	22:54:05.9	−17:34:55	0.06	1.182	243	−22.2	–	2.9×10^{44}

References.[a]NED, [b]Véron-Cetty & Véron (2010), [c]Kellermann et al. (1994), [d1]Zhou & Zhang (2010), [d2]Laurent-Muehleisen et al. (1997), [d3]Bicay et al. (1995), [d4]Barvainis, Lonsdale & Antonucci (1996), [d5]Edelson (1987),[e]Zhou & Zhang (2010), [e1]Piconcelli & Guainazzi (2005), [e2]Shu, Yaqoob & Wang (2010), [e3]Bianchi et al. (2009), [e4]Gallo (2006).

All objects in our sample, except Mrk 509 and MR 2251−178, are also part of the Bright Quasar Survey (Schmidt & Green 1983) and Palomar Green survey (Neugebauer et al. 1987). Mrk 509 is usually classified as a type 1 Seyfert nucleus. However, this object fits all our selection criteria and has an absolute magnitude ($M_B = -22.5$) consistent in the optical with the QSO definition (Véron-Cetty & Véron 2010). MR 2251–178 has not been widely studied in the literature. However, this object also fit our selection criteria, and its X-ray luminosity places it among the most powerful AGN with $M_B = -22.2$ (Véron-Cetty & Véron 2010). Note that all the objects in our sample have *Spitzer/IRS* spectra, except for MR 2251−178.

The redshift, *N*-band flux density and X-ray luminosity distributions for the sample are shown in Fig. 1, and the list of QSOs and their literature-compiled properties is given in Table 1.

Table 2. Log of GTC/CC imaging observations in Si2 band (8.7 μm). Column 1 gives the name of the QSO; column 2 the date of observations; column 3 the on-source time integration; column 4 the name of the standard star (Cohen 1999); column 5 the time elapsed between standard star and science target acquisition; column 6 the FWHM of the standard star; columns 7 and 8 the airmass and precipitable water vapour during the observations; column 9 the position angle that indicates the orientation of the detector on the sky and column 10 the programme for which the data were acquired, where GT stands for Guaranteed Time, ESO-GTC for European Southern Observatory-GTC large programme and MEX for open Mexican time.

Name	Date	t_{on} (s)	STD (s)	t_{offset} (min)	$FWHM_{STD}$ (arcsec)	Airmass	PWV (mm)	PA (deg)	Programme
PG 0003+199	2013.09.15	904	HD 2436	8	0.27	1.18	11.3	0	GT
PG 0007+106	2013.09.27	973	HD 2436	9	0.30	1.20	13.6–14.0	0	MEX
PG 0050+124	2013.09.14	904	HD 2436	9	0.35	1.3	9.8–10.3	0	GT
PG 0804+761	2014.01.03	3 × 209	HD 64307	42	0.33	1.47	9.4	360	ESO-GTC
PG 0844+349	2014.01.06	3 × 216	HD 81146	17	0.34	1.05	7.3–7.1	360	ESO-GTC
PG 0923+129	2015.04.03	695	HD 82381	9	0.34	1.04	5.0–5.5	0	MEX
PG 1211+143	2014.03.14	3 × 209	HD 107328	26	0.31	1.04	<10	0	ESO-GTC
PG 1229+204	2014.06.08	1251	HD 111067	8	0.27	1.04	6.3–6.4	360	ESO-GTC
PG 1351+640	2014.05.20	1112	HD114326	8	0.28	1.08	4.6	360	MEX
PG 1411+442	2014.03.16	2 × 209	HD128902	2	0.27	0.96	4.0–3.5	360	ESO-GTC
PG 1426+015	2012.03.09	3 × 220	HD126927	58	0.40	1.15	3.0	0	ESO-GTC
PG 1440+356	2014.03.16	209	HD128902	4	0.25	1.13	4.8	0	ESO-GTC
PG 1448+273	2014.06.08	1112	HD138265	11	0.27	1.35	8.1–5.1	360	MEX
PG 1501+106	2013.08.30	3 × 209	HD 140573	7	0.27	1.48	5.3	360	ESO-GTC
PG 1534+580	2015.04.04	695	HD 138265	6	0.33	1.28	1.8–2.5	360	MEX
PG 1535+547	2014.05.16	1112	HD138265	6	0.30	1.61	4.8–5.0	360	MEX
PG 2130+099	2014.06.10	904	HD206445	8	0.28	1.13	7.4–7.5	0	GT
PG 2214+139[a]	2013.09.17	1042	HD220363	13	0.8	1.32	9.0	0	MEX
MR 2251−178	2013.09.17	1043	HD220363	7	0.3	1.30	<10	0	MEX

Note. [a]Bad quality image.

3 OBSERVATIONS AND DATA REDUCTION

3.1 GTC/CC 8.7 μm imaging

A total of 12 QSOs in our sample were observed within the European Southern Observatory-GTC (PI: A. Alonso-Herrero, ID: 182.B-2005) and the CC Guaranteed Time (PI: C. Telesco) large programmes, which also include a large sample of other AGN with X-ray luminosities between $L_{2-10\,keV} \sim 3 \times 10^{38}$ and 3×10^{45} erg s^{-1} (Alonso-Herrero et al. 2016a). The other eight objects were observed with Mexican time on this facility (PIs: I. Aretxaga and M. Martínez-Paredes).

All QSOs in the sample, except for Mrk 509, were observed with GTC/CC in imaging mode with the Si2 filter ($\lambda_c = 8.7$ μm, $\Delta\lambda = 1.1$ μm) between 2012 March and 2015 April. Note that we excluded Mrk 509 because it has unresolved emission at MIR, as reported by Hönig et al. (2010). On average, the images were acquired with a precipitable water vapour (PWV) ∼7.1 mm and typical air mass of ∼1.2. The log of the imaging observations is compiled in Table 2.

In order to flux-calibrate and estimate the image quality, a standard star was imaged with the same filter just before or after the science target. Considering that the theoretical diffraction-limited FWHM[2] (Packham & Telesco 2007) of the point spread function (PSF) of CC in the Si2 band is 0.19 arcsec, the majority of QSOs have good image quality (<FWHM > ∼0.3 arcsec), except for PG 2214+139, which was observed with FWHM ∼0.8 arcsec.

We use the CC pipeline RedCan developed by González-Martín et al. (2013) for the reduction and analysis of ground-based MIR CC and T-ReCS imaging and spectroscopy. The image reduction starts with sky subtraction, stacking of individual images, and rejection of bad images. Next, flux calibration is performed using the standard star. These were selected from the catalogue of spectrophotometric standard stars published by Cohen (1999). The final step for image reduction is aperture photometry of the target inside a default aperture radius of 0.9 arcsec, which is a good estimate of the total flux for point-like sources.

3.2 GTC/CC 7.5–13.5 μm spectroscopy

We observed 10 QSOs within the guaranteed and ESO-GTC time in low-resolution spectroscopy ($R = 175$) at N band ($\lambda_c = 7.5 - 13.5$ μm). These data were acquired between 2013 September and 2014 December with a slit width of 0.52 arcsec. Furthermore, Mrk 509 and PG 0050+124 (IZw1) were already observed with VISIR/VLT by Hönig et al. (2010) and Burtscher et al. (2013), respectively (see Section 4), and we used their high-resolution spectroscopy in our analysis. We also observed MR 2251−178 within the Mexican time because this is the only object in the sample without *Spitzer/IRS* spectra. The low-resolution spectroscopy for this object was obtained in 2015 July with a slitwidth of 0.52 arcsec. Altogether, spectroscopy was acquired in 8- to 10-m-class telescopes for 13 out of the 20 objects.

On average, CC spectroscopy was obtained with a $PWV \sim 6.6$ mm and airmass ∼1.27. We estimate the image quality from the image of the standard star obtained at Si2 band just before the acquisition of the science target (<FWHM > ∼0.4 arcsec). The log of CC spectroscopic observations is shown in Table 3.

The spectroscopic observations were also reduced with RedCan. The first steps of the reduction process are similar to those for imaging, followed by two-dimensional wavelength calibration of the target and standard star using sky lines. Then, we define the trace of a PSF using the observations of the standard star. Finally, a point-like extraction was made and we applied both slit-loss correction and aperture correction. For more details on the MIR data reduction pipeline see González-Martín et al. (2013).

[2] http://www.gtc.iac.es/instruments/canaricam/canaricam.php#Imaging

Table 3. Log of GTC/CC spectroscopic observations in *N* band (7.5–13.5 μm). Column 1 gives the name of the QSO, column 2 the date of observations, column 3 the on-source time integration, column 4 the name of the spectrophotometric standard star, column 5 the FWHM of the standard star, columns 6 and 7 the airmass and the precipitable water vapour during the observations, column 8 the position angle of the slit and column 9 the observational programme for which the data were acquired.

Name	Date	t_{on} (s)	STD	$FWHM_{STD}$ (arcsec)	Airmass	PWV (mm)	PA (deg)	Programme
PG 0003+199	2013.09.22	2 × 766	HD 2436	0.24	1.25	NA	65	GT
PG 0804+761	2014.03.15	3 × 354	HD 64307	0.33	1.48	7.7	360	ESO-GTC
	2014.01.03	3 × 354	HD 64307	0.33	1.56	7.6	360	
PG 0844+349	2014.12.03	1238	HD 81146	0.28	1.45	4.5–4.1	0	ESO-GTC
	2014.12.05	1238	HD 81146	0.34	1.15	7.2	360	
PG 1211+143	2014.03.14	3 × 295	HD 113996	0.34	1.07	8	0	ESO-GTC
	2014.06.18	943	HD 109511	0.24	1.31	8.1	360	
PG 1229+204	2014.06.20	1238	HD 111067	0.42	1.35	7.1	360	ESO-GTC
	2014.06.20	1238	HD 111067	0.42	1.31	8.1	360	
PG 1411+442	2014.05.30	1238	HD 128902	1.05	6.9	6.9	360	ESO-GTC
	2014.05.31	1238	HD 128902	0.36	1.35	5.9	360	
PG 1426+015	2014.05.19	943	HD 126927	0.34	1.16	3.8–3.7	360	ESO-GTC
	2014.06.09	943	HD 126927	0.30	1.33	8.7		
PG 1440+356	2014.06.07	1238	HD 128902	0.30	1.03	5.8–6.9	360	ESO-GTC
	2014.06.07	1238	HD 128902	0.26	1.12	6.1–6.5	360	
PG 1501+106	2014.05.27	943	HD 133165	0.37	1.12	4.8	360	ESO-GTC
	2014.05.01	943	HD 133165	0.28	1.33	6.0	360	
PG 2130+099	2014.09.21	2 × 766	HD 206445	0.31	1.05	4.2–5.6	90	GT
MR 2251−178	2015.07.06	1120	HD219449	0.52	1.52	7.0	90	MEX

Table 4. NIR unresolved fluxes from the literature. Column 1 gives the names of the QSOs, column 2 the unresolved flux at *H* band from *HST*/NICMOS (Veilleux 2006; Veilleux et al. 2009b) and columns 3 and 4 the upper limits at *K* and *H* bands (Surace, Sanders & Evans 2001), respectively.

Name	F160W-*HST*/NICMOS (PSF) f_ν (mJy)	K′-QUIRC/Gemini (PSF) f_ν (mJy)	H-QUIRC/Gemini (PSF) f_ν (mJy)
PG 0007+106	2.9	<19.3	...
PG 0050+124	11.4	<39.6	...
PG 0804+761	...	<26.2	<13.2
PG 0844+349	5.9	...	...
PG 1211+143	...	...	<11.51
PG 1229+204	2.7	<7.0	...
PG 1351+640	...	<9.3	<6.4
PG 1411+442[a]	7.1	<15.8	...
PG 1426+015	5.8	<18.1	...
PG 1440+356	9.1	<17.6	...
PG 2130+099	9.2	<25.5	...
PG 2214+139	6.5	...	...
Mrk 509[b]	...	...	...

Note. [a]This object presents an unresolved flux at *J* band <6.44 mJy from QUIRC/Gemini. [b]This object presents fluxes measured in an aperture diameter of 3 arcsec at *J* (<10.7 mJy), *H* (<14.1 mJy) and *K* (<22.3 mJy) bands from ISAAC/VLT, which have been used in the present work as upper limits (Fischer et al. 2006).

4 ANCILLARY DATA

We compile high angular resolution NIR (1–3 μm), MIR (5–35 μm) imaging and spectroscopy from the literature with estimates of unresolved emission, when available, in order to build complete nuclear NIR-to-MIR SEDs of the QSOs in the sample. The unresolved fluxes are the result of removing, using various methods, the underlying NIR and MIR emission related to the host galaxy, and not directly linked to AGN and dusty torus emission. In Table 4 we list the data gathered from previous studies.

4.1 *HST*/NICMOS data

Veilleux (2006) and Veilleux et al. (2009b) observed with NICMOS/*HST* at *H* band (F160W, $\lambda_c = 1.60$ μm) a sample of 28 QSOs as part of the Quasar/ULIRG Evolution Study (QUEST), nine of which are in our sample. The high angular resolution (∼0.3 arcsec) and pixel size (∼0.076 arcsec pixel^{-1}) of NICMOS allow us to have a good estimate of the unresolved emission (FWHM = 0.14 arcsec). In the present work we have used the unresolved emission reported in this band. The photometric errors are ∼10 per cent.

4.2 Upper limits from QUIRQ on Gemini North and ISAAC/VLT

Guyon, Sanders & Stockton (2006) report unresolved emission at K' band ($\lambda_c = 2.12$ μm, $\Delta_\lambda = 0.41$ μm), and at *H* band ($\lambda_c = 1.65$, $\Delta_\lambda = 0.30$ μm) for several of our QSOs (see Table 4). These data

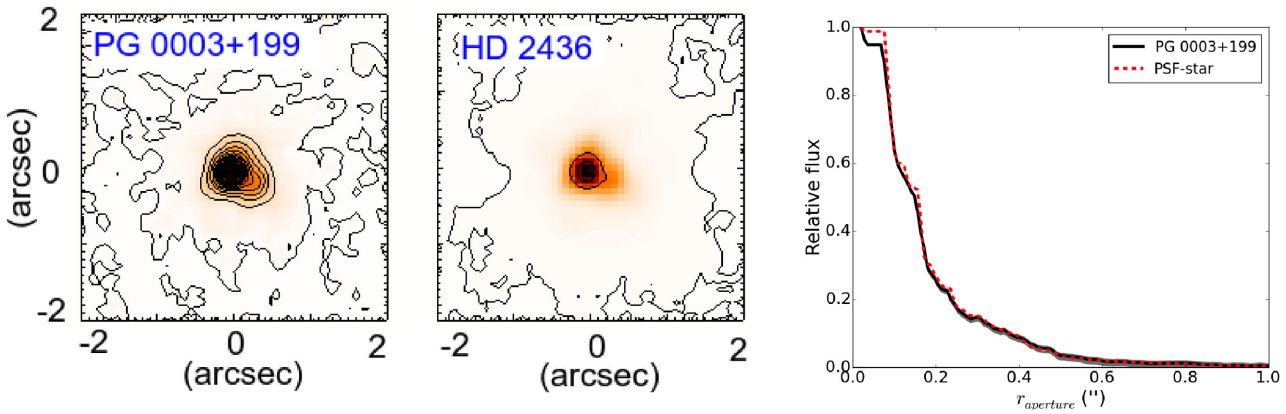

Figure 2. Left and middle panels: Si2 images of PG 0003+199 and its standard star. The lowest contour is 3σ over the background and the next contours are traced in 2σ steps (except in the PSF image). Right panel: radial profiles of PG 0003+199 in black solid line, and its standard star in red dotted line.

were obtained with the IR camera QUIRC (Hodapp et al. 1996) on the Gemini North telescope, with an angular resolution ∼0.2 arcsec.

Mrk 509 has nuclear fluxes at *Js* (λ_c = 1.25 μm), *H* (λ_c = 1.65 μm) and *Ks* (λ_c = 2.16 μm) bands measured with the IR camera ISAAC on the Very Large Telescope (VLT), with a spatial resolution of 0.6–1 arcsec. The nuclear flux was, however, measured in an aperture diameter of 3 arcsec (Fischer et al. 2006), and hence, we use these fluxes as upper limits.

4.3 VISIR/VLT nuclear spectroscopy at N band

PG 0050+124 and Mrk 509 have *N*-band (λ_c = 10 μm) low-resolution (R = 300) spectroscopy acquired with VISIR, with a spatial resolution ∼0.3 arcsec (Hönig et al. 2010; Burtscher et al. 2013). The slitwidth was 0.75 arcsec and the spectra cover a wavelength of between ∼7.5 and 13.5 μm.

4.4 *Spitzer/IRS* spectroscopy

Most QSOs in our sample are part of the *Spitzer/IRS* telescope spectroscopic survey QUEST (PID: 3187; PI: Veilleux). In general, they have been observed with the following low-resolution modes:[3] SL1∼7.4–14.5 μm, SL2∼5.2–7.7 μm, LL1∼19.9–39.9 μm and LL2∼13.9–21.3 μm. The slit widths range from 3.6 to 11.1 arcsec (Werner et al. 2004; Houck et al. 2004).

Fully reduced and calibrated spectra were downloaded from the Cornell Atlas data base of *Spitzer/IRS* CASSIS (v6; Lebouteiller et al. 2011), which provides optimal extraction regions to ensure the best signal-to noise ratio. We stitch the different module spectra together using module SL2 as a reference spectrum for flux scaling using our own PYTHON routines.

5 ANALYSIS

5.1 MIR imaging photometry at Si2 band (λ_c = 8.7 μm)

In order to estimate if the QSOs have extended emission over the stellar PSF, we perform aperture photometry on the QSOs and their corresponding standard stars with increasing apertures using the PHOT and APHOT tasks of the image analysis package IRAF. We combine these measurements to build radial profiles. Fig. 2 shows the images of PG 0003+199, its standard star and their radial profiles, in which it is clearly seen that the QSO is dominated by unresolved emission. In Fig. 3 we show the data and analysis for PG 0050+124, which presents a clear extended component. For this object we also show the GALFIT model and its residual (see Appendix A for more details on the analysis of the extended component with GALFIT). The images and analysis for the rest of the QSOs can be seen in Appendix B.

The uncertainties in the radial profiles include photometric errors, which are estimated as $\sqrt{\sigma^2_{\rm back} N_{\rm pix} + \sigma^2_{\rm back} N^2_{\rm pix}/N_{\rm pix-ring}}$, where $N_{\rm pix}$ is the number of pixels inside the aperture considered, $N_{\rm pix\text{-}ring}$ is the number of pixels inside an 80 pixel-width ring around the source, used to estimate the background level and its standard deviation $\sigma_{\rm back}$ (see Reach et al. 2005). The second term of the error equation is almost negligible because the backgrounds in our images are flat. In addition, we also consider a six per cent uncertainty due to time-variability of the sky transparency and adopt a 13 per cent uncertainty due to PSF-variability.[4]

In order to estimate variations of the PSF due to variable sky conditions, we use observations of the same standard star acquired consecutively. For two of the QSOs (PG 1426+015 and PG 1229+204) we acquired several observations of the standard star just before or after the target. We find that the FWHM of the PSF varies ∼15 per cent in time-scales of a few minutes, consistent with the results of Mason et al. (2012). This is likely the reason why several QSOs (e.g. PG 0804+761, PG 0844+349, PG 0923+129, PG 1229+204, PG 1351+640, PG 2130+099) show radial profiles with FWHM slightly narrower than their corresponding standard stars (see figures in Appendix B).

Allowing for these mild FWHM variations, the radial profile of the standard stars represents the maximum contribution to the emission due to an unresolved source. Therefore, taking into account all the uncertainties, all QSOs, except PG 0050+124, are unresolved in our MIR imaging (see figures in Appendix B). In Table 5 we list the flux at Si2 band measured inside an aperture radius of 1 arcsec, plus the ratio between the FWHM of the QSO and its standard star, which shows that the majority of the objects in the sample are indeed unresolved. The errors are estimated adding in quadrature

[3] http://irsa.ipac.caltech.edu/

[4] This has been calculated from the analysis of several standard stars observed during the same night at MIR with T-ReCS on Gemini (Mason et al. 2012).

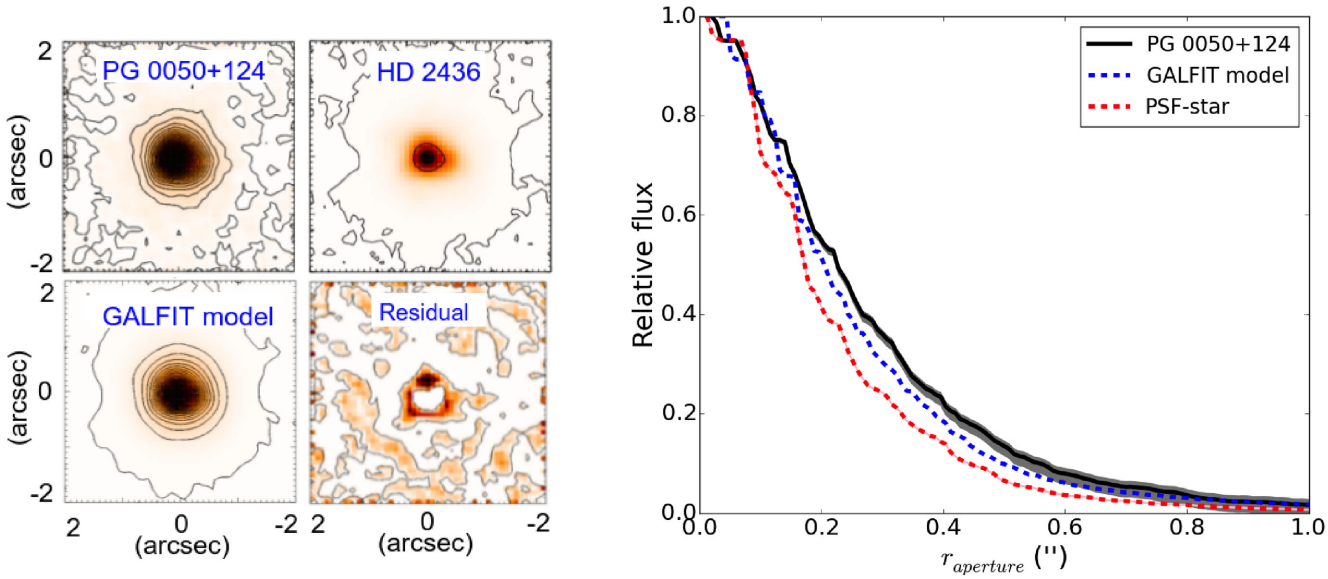

Figure 3. Left to middle panels: Si2 images of PG 0050+124 and its standard star, GALFIT model and its residual image. Right panel: radial profile of PG 0050+124 in black solid line, its standard star in red dotted line and best GALFIT model in blue dotted line.

Table 5. Results of the imaging analysis. Column 1, name of the QSO; column 2, unresolved flux at Si2 (8.7 μm) band; column 3, ratio between the QSO and standard star FWHM.

Name	f_ν ($r = 1$ arcsec) (mJy)	$\frac{\text{FWHM}_{\text{target}}}{\text{FWHM}_{\text{STD}}}$
PG 0003+199	159.2 ± 0.1	1.0
PG 0007+106	40.8 ± 0.2	1.2
PG 0050+124	249.1 ± 0.2	1.3
PG 0804+761	105.1 ± 0.2	1.0
PG 0844+349	29.4 ± 0.7	0.9
PG 0923+129	92.6 ± 0.2	0.9
PG 1211+143	89.3 ± 0.2	1.1
PG 1229+204	31.5 ± 0.2	1.0
PG 1351+640	67.2 ± 0.2	0.9
PG 1411+442	65.7 ± 0.4	1.0
PG 1426+015	56.0 ± 0.1	1.1
PG 1440+356	67.200 ± 0.004	1.3
PG 1448+273	25.0 ± 0.2	1.1
PG 1501+106	92.2 ± 0.1	1.0
PG 1534+580	111.9 ± 0.9	1.2
PG 1535+547	43.7 ± 1.0	1.1
PG 2130+099	118.7 ± 0.1	0.9
MR 2251−178	49.2 ± 0.2	1.3

the photometric error, the flux calibration, the time-variability and the PSF-variability uncertainties.

5.2 *Spitzer/IRS* and GTC/CC spectroscopy

We compare the nuclear GTC/CC and *Spitzer/IRS* spectra for the 10 QSOs with both types of data (namely PG 0003+199, PG 0804+761, PG 0844+349, PG 1211+143, PG 1229+204, PG 1411+442, PG 1426+015, PG 1440+356, PG 1501+106 and PG 2130+099; see Fig. 4 and figures in Appendix C). We observe that, within the uncertainties, the shapes of both spectra are similar. The most notable differences are at the edges of the GTC/CC spectra (∼7.5 and ∼13.5 μm) and in the ∼9.0–9.7 μm

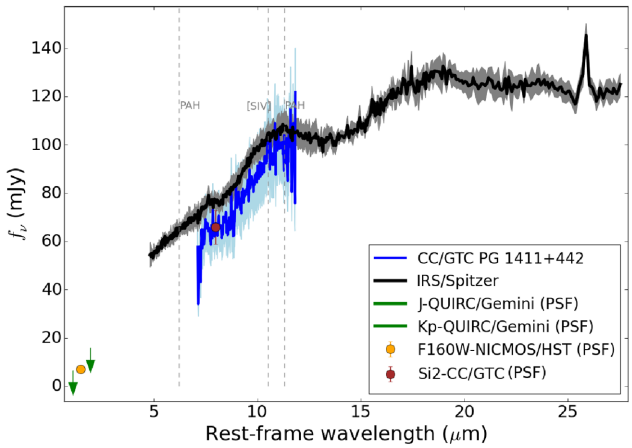

Figure 4. SED of the unresolved component of PG 1411+442, using our GTC/CC unresolved emission, the ancillary photometry, the GTC/CC spectrum (nuclear, width slit ∼0.5 arcsec) and the *Spitzer/IRS* spectrum (width slit ∼3 arcsec).

rest-frame range. We attribute these differences to low atmospheric transmission[5] (Lord 1992, see Fig. 4).

In general, the flux measured in the Si2 band within 1 arcsec apertures is consistent with both the nuclear GTC/CC and *Spitzer/IRS* spectra. For MR 2251−178, the only QSO that does not have *Spitzer/IRS* spectrum, the unresolved emission in Si2 band is consistent with the spectral flux at 8.7 μm. As an example, in Fig. 4 we show the observed NIR to MIR unresolved SED and spectroscopy of PG 1411+442, and the rest of the QSOs are shown in Appendix C.

For the QSOs that do not have nuclear GTC/CC spectra we compare the flux of the unresolved emission in Si2-band image with that derived from the *Spitzer/IRS* spectra. PG 1351+640 and PG 1535+547 have Si2 unresolved emission consistent with their *Spitzer/IRS* spectra at 8.7 μm (see Fig. C1). PG 0007+106 and

[5] http://www.gtc.iac.es/instruments/canaricam/MIR.php

PG 1448+273 have unresolved emission fainter than their spectra at 8.7 μm, suggesting the presence of an extended component within the *Spitzer* aperture (see Fig. C1). Finally, PG 0923+129 and PG 1534+580 have unresolved emission estimated from the image that is brighter than that of its spectrum at 8.7 μm (see Fig. C1), probably due to uncertainties in the flux loss correction (Alonso-Herrero et al. 2016a). PG 2214+139 has a bad-quality image at Si2 band and it is not possible to measure the flux to compare it with its *Spitzer/IRS* spectrum.

For PG 0050+124 and Mrk 509 we compare the nuclear VISIR/VLT spectra with the *Spitzer/IRS* spectra and the unresolved emission at Si2 band from CC. In both cases the flux of the nuclear VISIR/VLT spectra is lower than the *Spitzer/IRS* ones, while the CC unresolved emission is consistent with the nuclear VISIR/VLT spectra (see Fig. C1 in Appendix C). The spectral shapes of VISIR/VLT and *Spitzer/IRS* spectra are also similar.

The nuclear and *Spitzer/IRS* spectral shapes are similar and the unresolved emission at Si2 band is consistent with the nuclear and *Spitzer/IRS* spectra. Thus, we assume that the *Spitzer/IRS* spectra of all QSOs in our sample are mostly dominated by emission due to the AGN and its surrounding torus.

6 *SPITZER/IRS* SPECTRAL DECOMPOSITION: ISOLATING THE AGN EMISSION

Evidence for star formation through the detection of PAH features in the *Spitzer/IRS* spectra is present in 40 per cent of the QSOs studied by Schweitzer et al. (2006), and also in the stacked spectrum of those that lacked individual detections, implying that starbursts are present in most QSOs. We use the tool DEBLENDIRS (Hernán-Caballero et al. 2015) to decompose the *Spitzer/IRS* spectra of the QSOs into their starburst (PAH and stellar) and AGN components. DEBLENDIRS uses a set of *Spitzer/IRS* templates of galaxies dominated by AGN emission, PAH emission (interstellar medium, ISM) and stellar emission (passive population of the host galaxy) and follows a χ^2 minimization method to find the combination of templates that best reproduces the spectrum of the source under study. Additionally, the rms-variation coefficient is also used as a second criterion to select the best combination of templates (Hernán-Caballero et al. 2015).

Using Bayesian inference, DEBLENDIRS estimates the probability distribution of the fractional contribution to the integrated MIR emission for the stellar, PAH and AGN components, the AGN luminosity contribution at 12 and 6 μm, and the starburst luminosity contribution at 12 μm. It also calculates the MIR spectral index α and the silicate strength $S_{\rm sil}$ for the AGN component, where α is calculated between 6 and 12 μm assuming a power law $f_\nu = \nu^\alpha$, and the silicate strength is defined as

$$S_{\rm sil} = \ln \frac{F(\lambda_{\rm p})}{F_C(\lambda_{\rm p})}, \quad (1)$$

where $F(\lambda_{\rm p})$ and $F_C(\lambda_{\rm p})$ are the flux densities at the peak of the silicate feature and its underlying continuum, respectively. See Hernán-Caballero et al. (2015) for details.

The spectral decomposition is done between ∼5 and 15 μm in the rest frame. All spectra were re-sampled to a common wavelength resolution $\Delta\lambda = 0.1$ μm. In Figs 5 and 6 we show the spectral decomposition of a QSO dominated by the AGN component (Mrk 478) and one with significant contributions by PAH and stellar components (PG 1211+143). Table 6 lists the results of the median and 68 per cent confidence intervals of the integrated MIR luminosity at 5–15 μm, and within the *Spitzer/IRS* slit, attributed to the three components, and the best templates used to decompose each QSO. Table 7 lists the AGN luminosity contribution at 12 and 6 μm, the starburst luminosity contribution at 12 μm, the MIR spectral index α and the silicate strength $S_{\rm sil}$. PG 0050+124 and PG 1351+640 were poorly fitted around the silicate feature, and hence we measure the feature on the spectra directly.

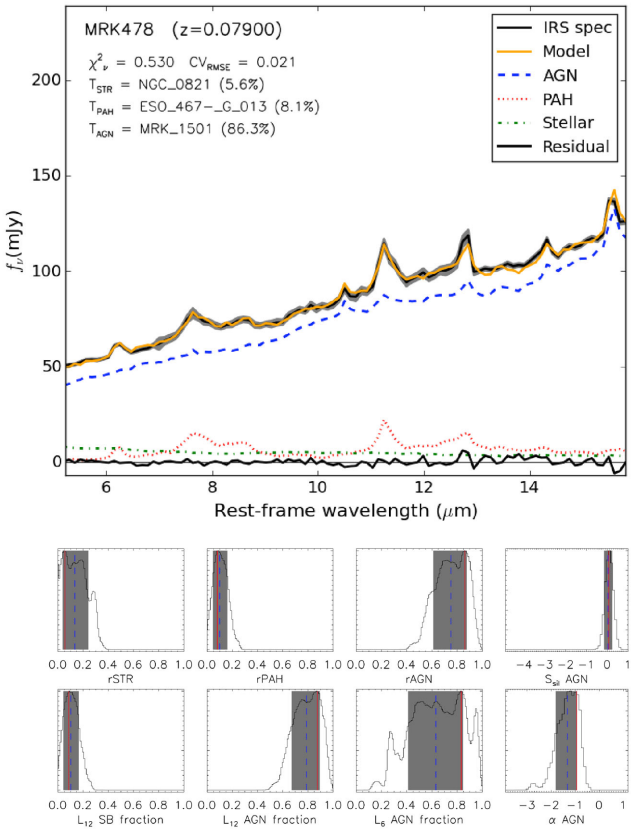

Figure 5. Output of the DEBLENDIRS spectral decomposition of PG 1440+356. Upper panel: the black line shows the *Spitzer/IRS* spectrum and the grey area its 1σ uncertainty. The orange line shows the best-fitted model, which is the sum of the AGN (blue dashed line), PAH (red dashed line) and stellar templates (dashed green line). We also show the residual of the fit as a black solid line around zero flux density. Lower panels: probability distributions of the eight parameters obtained from the spectral decomposition, rSTR, rPAH and rAGN stand for fractional contributions of the stellar, PAH and AGN components, respectively; $S_{\rm Sil}$ AGN for silicate strength; L_{12} SB fraction, L_{12} AGN fraction, L_6 AGN fraction for the starburst and AGN fractional luminosities at 12 and 6 μm; and α AGN MIR spectral index of the AGN component.

We cannot find a combination of templates to reproduce the spectrum of PG 1351+640 (see Fig. D1), probably because this object presents prominent silicate feature in emission. This object, together with PG 0050+124, PG 1211+143 and PG 0804+761, is among the first objects in which prominent emission of silicates at 10 and 18 μm was observed (e.g. Sturm et al. 2002; Hao et al. 2005; Dudik et al. 2007).

We find that within the *Spitzer/IRS* aperture of ∼3.6 arcsec (1–6 kpc), on average the starburst component contributes ∼15 per cent (∼3 per cent PAH and 12 per cent stellar) and the AGN component 85 per cent to the integrated luminosity of the system in the MIR. These results are consistent with the fact that the nuclear MIR emission reported in the present work is mostly dominated by the AGN (Section 5.1).

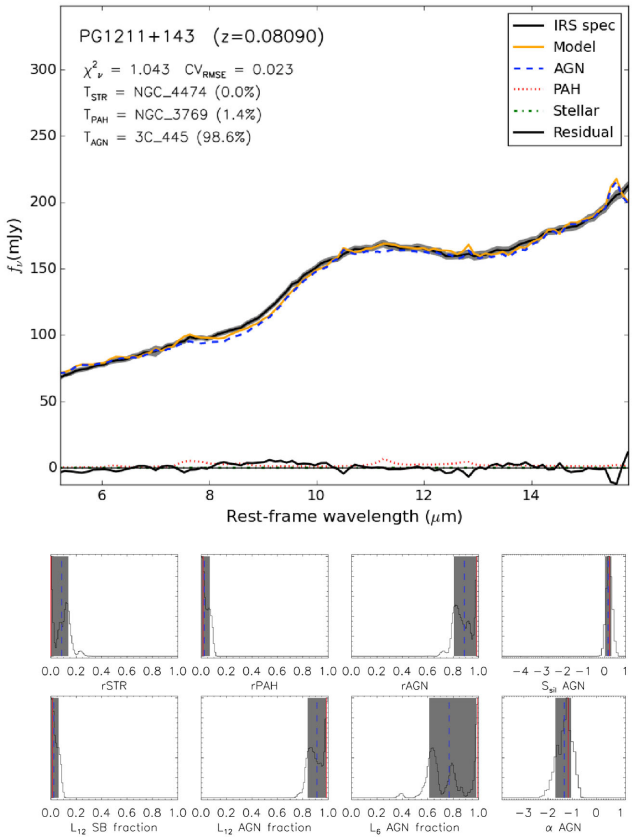

Figure 6. As Fig. 5 but for PG 1211+143. Note that in this case the *Spitzer*/IRS is completely dominated by the AGN component (blue line), while the stellar and PAH components are negligible (green and red lines, respectively).

7 DUSTY TORUS MODELLING

7.1 CLUMPY models

In this section we adopt the CLUMPY models of Nenkova, Ivezić & Elitzur (2002), Nenkova et al. (2008a,b) as a description of the distribution of clouds that form the dusty torus. Within this framework the distribution of clouds is described by a set of six free parameters (see Fig. 7). The clouds that surround the central engine have the same optical depth, τ_V. The inner radius of the cloud distribution is defined by the dust sublimation temperature ($T_{\rm sub} \approx$ 1500 K for silicates), with $R_{\rm d} = 0.4$ (1500 K $T_{\rm sub}^{-1})^{2.6}(L/10^{45}$erg s$^{-1})^{0.5}$ pc, while the radial extent Y is defined as the ratio between the outer ($R_{\rm o}$) and inner radius ($R_{\rm d}$). The radial distribution of clouds is parametrized as r^{-q}, where q is a free parameter. Additionally, there are other three free parameters that describe the geometry of the torus: the viewing angle i, the angular size $\sigma_{\rm torus}$ and the average number of clouds along a radial equatorial line N_0, which can be used to calculate the number of clouds along the line of sight (LOS) as $N_{\rm LOS}(i) = N_0 e^{(-(i-90)^2/\sigma^2_{\rm torus})}$. According to this description the classification of an AGN as type 1 or type 2 does not depend only on the viewing angle i but the probability that AGN photons be able to escape through the torus without being absorbed by an optical thick cloud along the LOS. This is called the escape probability of AGN-produced photons, $P_{\rm esc} \simeq e^{-N_{\rm LOS}}$. Therefore, it is possible to obtain a type 1 AGN even at viewing angles close to the equatorial plane (Nenkova et al. 2002, 2008a,b).

The emission of CLUMPY clouds is the angle-averaged emission of all slab orientations. For the models we are using, τ_V, corresponds to the optical depth along the normal of the slab. There is a new version of CLUMPY models[6] (Heymann, Nikutta & Elitzur 2014) which uses spherical clouds with three-dimensional radiative transfer.

In order to be able to compare our results with the previous modelling performed in lower luminosity AGN (e.g. González-Martín et al., in preparation; Alonso-Herrero et al. 2011, 2016b; Ramos Almeida et al. 2011; González-Martín et al. 2013; Ichikawa et al. 2015; Martínez-Paredes et al. 2015; Fuller et al. 2016; García-Burillo et al. 2016; Mateos et al. 2016), we chose to use the 2008 CLUMPY models (Nenkova et al. 2002, 2008a,b).

We model the QSOs with the BAYESCLUMPY tool (Asensio Ramos & Ramos Almeida 2009), which uses Bayesian inference to fit the observed nuclear IR SEDs and MIR spectroscopy of AGN. The output is the probability distribution of the six free parameters of the model ($\sigma_{\rm torus}$, Y, N_0, q, i and τ_V) assuming flat prior information. BAYESCLUMPY allows us to fix (or fit) the redshift and the vertical shift too, i.e. the flux scaling factor of the model spectrum. In addition, it is also possible to include foreground extinction, parametrized by A_V, when we are modelling type 2 AGN (see Alonso-Herrero et al. 2011). For type 1 AGN it is possible to add the AGN (accretion disc) emission in the form of a power-law contribution as described by Nenkova et al. (2002). The method uses a Metropolis–Hastings Markov Chain Monte Carlo (MCMC) sampling technique to determine the posterior distributions of the free CLUMPY torus model parameters. These are used in turn to calculate the escape probability distribution ($P_{\rm esc}$) and the distribution of the geometrical covering factor, $f_2 = 1 - \int_0^{\pi/2} P_{\rm esc}(\beta)\cos(\beta)d\beta$ (e.g. Alonso-Herrero et al. 2011). For more details on BAYESCLUMPY, see Ramos Almeida et al. (2014).

In order to fit the models, we start by using the unresolved NIR and MIR starburst-subtracted spectrum between ∼5 and 15 μm for all QSOs except PG 1211+143, PG 1351+640, PG 1501+106, and PG 0050+124. The MIR emission of these three QSOs appears to be completely dominated by dust heated by the AGN (see Section 6), with negligible starburst contributions. In these cases we use the IRS spectrum (observed wavelength between ∼5 and 30 μm) extracted from the data base. For three QSOs (PG 0050+124, PG 1211+143 and PG 1501+106) the spectral range between ∼5 and 8 μm was excluded (as discussed in Sections 7.2 and 8.2).

In the case of PG 0050+124 the flux density of the unresolved component at 8.7 μm is fainter than the corresponding flux density of the spectrum (see Section 5.2 and Fig. C1), suggesting the presence of an extended component in the spectrum larger than the expected uncertainties in flux calibration. Hence, we scale the *Spitzer/IRS* spectrum to the 8.7 μm photometry data point. For this QSO we use the spectral range between ∼8 and 20 μm, where the emission is strongly dominated by the dusty torus. For MR 2251−178 we used the GTC/CC spectrum.

We remove the emission lines ([S IV] 10.4 μm, [Ne II] 12.81 μm, [Ne V] 14.32 μm and [Ne III] 15.56 μm) from the spectra before fitting the models, since the emission lines are not modelled. We adopt non-informative priors as flat distributions within the range of values shown in Table 8 for the six free parameters, and vertical shift values between −4 and 4. For all QSOs we include the direct-light power-law AGN component and do not include a screen of extinction.

[6] www.clumpy.org

Table 6. Spectral decomposition. Column 1 gives the name of the QSO, columns 2 and 3 the name of the PAH template and its contribution, columns 4 and 5 the name of the AGN template and its contribution between 5 and 15 μm within the IRS slit, columns 6 and 7 the name of the stellar template and its contribution, and columns 8 and 9 the reduced χ^2_ν and the rms error coefficient for the best-fitting model. The fractional contribution is measured between 5 and 15 μm.

Name	PAH	Per cent	AGN	Per cent	Stellar emission	per cent	χ^2_ν	$CV_{\rm RMSE}$
PG 0003+199	NGC 3769	0.3	PG 1114+445	83.6	M 85	16.0	0.071	0.019
PG 0007+106	NGC 3187	3.1	PG 1114+445	88.4	NGC 5812	8.5	0.226	0.030
PG 0050+124	NGC 2993	0.0	[HB89] 1402+436	99.5	M 85	0.5	0.45	0.042
PG 0804+761	NGC 3769	0.1	J143220.15+331512.2	75.2	NGC 1700	24.7	0.315	0.042
PG 0844+349	NGC 5996	3.3	J131217.7+351521	89.3	NGC 1374	7.5	0.289	0.036
PG 0923+129	UGC 09618	7.0	PG 1149−110	88.8	M 85	4.2	0.279	0.031
PG 1211+143	NGC 3769	1.4	3C 445	98.6	NGC 4474	0.0	1.043	0.023
PG 1229+204	NGC 2993	0.0	PG 1149−110	87.5	NGC 1700	12.5	0.227	0.031
PG 1351+640	NGC 2993	0.0	2MASX J02343065+2438353	97.1	NGC 1700	2.9	4.33	0.146
PG 1411+442	J14361112+6111265	1.7	J1640100+410522	80.2	NGC 1700	18.1	0.096	0.019
PG 1426+015	ESO 557-G-001	1.0	VII Zw 244	86.0	NGC 1700	13.0	0.120	0.027
PG 1440+356	ESO 467 G 013	8.1	Mrk 1501	86.3	NGC 0821	5.6	0.530	0.021
PG 1448+273	NGC 3310	3.4	J160222.38+164353.7	83.7	NGC 5812	12.9	0.333	0.048
PG 1501+106	MCG +08-11-002	0.0	PG 1149−110	99.2	NGC 5831	0.7	0.2	0.029
PG 1534+580	ESO 244-G-012	2.5	VII Zw 244	93.8	NGC 5831	3.7	0.271	0.032
PG 1535+547	NGC 3769	2.4	J1640100+410522	80.1	NGC 1700	17.5	0.203	0.028
PG 2130+099	NGC 3187	0.6	J14492067+4221013	89.1	NGC 4570	10.3	0.107	0.025
PG 2214+139	NGC 2993	0.0	HB89-1435-067	84.8	NGC 4570	15.2	0.062	0.016
Mrk 509	NGC 3310	8.1	3C 390.3	84.0	NGC 1549	7.9	0.068	0.023

Table 7. Parameters of the AGN component obtained for the *Spitzer/IRS* spectral decomposition. Column 1: name of the QSO. Column 2: AGN luminosity at 6 μm. Column 3: AGN luminosity at 12 μm. Column 4: MIR spectral index (8.1–12.5 μm). Column 5: silicate strength index.

Name	$\log L_{6\,\mu\rm m} = L_6$ (erg s^{-1})	$\log L_{12\,\mu\rm m} = L_{12}$ (erg s^{-1})	α (8.1 − 12.5 μm)	$S_{\rm sil}$
PG 0003+199	$43.70^{+0.15}_{-0.5}$	$43.77^{+0.06}_{-0.08}$	$-1.5^{+0.6}_{-0.8}$	$0.1^{+0.4}_{-0.3}$
PG 0007+106	$44.38^{+0.14}_{-0.24}$	$44.46^{+0.06}_{-0.08}$	$-1.5^{+0.5}_{-0.7}$	$0.01^{+0.30}_{-0.30}$
PG 0050+124[a]	$44.82^{+0.03}_{-0.03}$	$44.95^{+0.02}_{-0.03}$	$-1.4^{+0.1}_{-0.3}$	$0.2^{+0.2}_{-0.2}$
PG 0804+761	$44.88^{+0.10}_{-0.14}$	$44.89^{+0.04}_{-0.05}$	$-1.1^{+0.4}_{-0.4}$	$0.3^{+0.2}_{-0.3}$
PG 0844+349	$43.92^{+0.13}_{-0.23}$	$44.04^{+0.05}_{-0.07}$	$-1.6^{+0.5}_{-0.6}$	$0.2^{+0.2}_{-0.3}$
PG 0923+129	$43.42^{+0.14}_{-0.23}$	$43.69^{+0.05}_{-0.07}$	$-1.9^{+0.5}_{-0.7}$	$-0.03^{+0.20}_{-0.30}$
PG 1211+143	$44.60^{+0.12}_{-0.22}$	$44.91^{+0.01}_{-0.01}$	$-1.9^{+0.5}_{-0.8}$	$-0.04^{+0.20}_{-0.40}$
PG 1229+204	$43.90^{+0.15}_{-0.26}$	$44.10^{+0.05}_{-0.06}$	$-1.9^{+0.5}_{-0.8}$	$-0.04^{+0.20}_{-0.40}$
PG 1351+640[a]	$44.64^{+0.01}_{-0.1}$	$44.72^{+0.06}_{-0.07}$	$-2.0^{+0.1}_{-0.1}$	$0.6^{+0.1}_{-0.1}$
PG 1411+442	$44.76^{+0.5}_{-0.33}$	$44.47^{+0.09}_{-0.11}$	$-1.4^{+0.6}_{-0.7}$	$0.0^{+0.3}_{-0.4}$
PG 1426+015	$44.49^{+0.13}_{-0.21}$	$44.64^{+0.05}_{-0.07}$	$-1.7^{+0.6}_{-0.7}$	$0.07^{+0.30}_{-0.30}$
PG 1440+356	$44.33^{+0.18}_{-0.32}$	$44.38^{+0.09}_{-0.13}$	$-1.6^{+0.7}_{-0.9}$	$-0.03^{+0.30}_{-0.40}$
PG 1448+273	$43.84^{+0.13}_{-0.62}$	$44.08^{+0.05}_{-0.07}$	$-1.8^{+0.5}_{-0.7}$	$0.0^{+0.3}_{-0.3}$
PG 1501+106	$43.80^{+0.12}_{-0.62}$	$44.10^{+0.04}_{-0.04}$	$-2.1^{+0.5}_{-0.6}$	$-0.1^{+0.3}_{-0.4}$
PG 1534+580	$43.34^{+0.14}_{-0.25}$	$43.60^{+0.05}_{-0.06}$	$-1.9^{+0.4}_{-0.7}$	$0.03^{+0.30}_{-0.30}$
PG 1535+547	$43.58^{+0.16}_{-0.27}$	$43.59^{+0.08}_{-0.09}$	$-1.4^{+0.6}_{-0.7}$	$0.07^{+0.30}_{-0.30}$
PG 2130+099	$44.38^{+0.16}_{-0.26}$	$44.50^{+0.07}_{-0.10}$	$-1.6^{+0.6}_{-0.8}$	$-0.07^{+0.30}_{-0.40}$
PG 2214+139	$44.17^{+0.19}_{-0.27}$	$44.17^{+0.09}_{-0.11}$	$-1.3^{+0.6}_{-0.8}$	$0.2^{+0.3}_{-0.4}$
Mrk 509	$44.04^{+0.17}_{-0.30}$	$44.18^{+0.07}_{-0.09}$	$-1.8^{+0.6}_{-0.8}$	$-0.03^{+0.30}_{-0.40}$

Note. [a]These objects were poorly fitted around the silicate feature, and hence we measure the feature on the spectra directly (see statistics in Table 6).

7.2 Results for individual QSOs

From fitting the unresolved NIR emission and MIR AGN spectrum we note that for the majority of QSOs (12) the spectral range between ∼5 and 8 μm cannot be reproduced by the CLUMPY models with a set of parameters consistent with a type 1 AGN. In fact, the inclusion of this range results in a poor fit of the silicate features at 9.7 μm. To reproduce this emission, previous works have included, apart from the torus emission, a hot dust component (e.g. Mor et al. 2009; Deo et al. 2011; Mor & Trakhtenbrot 2011; Mor & Netzer 2012).

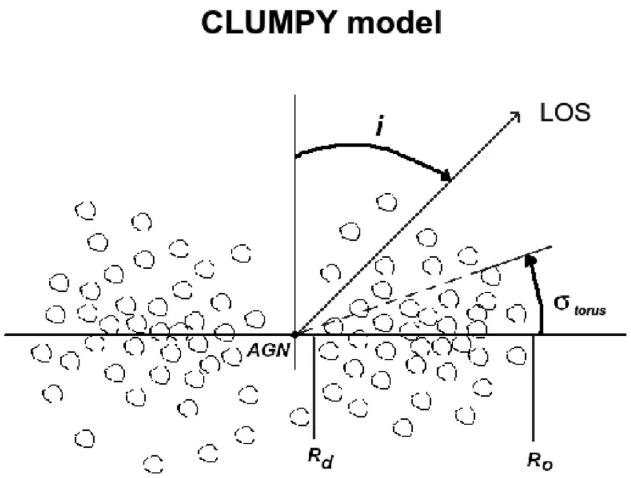

Figure 7. CLUMPY dusty torus geometry as described in Nenkova et al. (2008a,b). The radial extent of the torus is defined by the ratio between the outer radius R_o and the dust sublimation radius R_d, $Y = R_o/R_d$, with Y a free parameter. All clouds are assumed to have the same optical depth τ_ν. The angular width is given by σ, and N_{LOS} is the mean number of clouds found along a LOS at angle i.

Table 8. Parameters of the dusty CLUMPY torus model and assumed range in the prior distributions. Columns 2 to 7: angular width, radial extend, number of clouds along the equatorial line, index of the radial density profile, viewing angle and optical depth.

Parameter	σ_{torus} (deg)	Y	N_0	q	i (deg)	τ_V
Range	15–70	5–100	1–15	0–3	0–90	5–150

However, for the 20 QSOs in the sample the spectra are well reproduced by CLUMPY models when we fit in the 8–15 μm range (see Figs. 8 and 9 for and an example and Fig. E1 in Appendix E for the rest of the sample). For four objects (PG 2214+139, PG 0050+124, PG 1440+356 and PG 1411+442) a comparison of this new fitting with the spectra still shows an excess of NIR unresolved emission in the 5 to 8 μm range.

The posterior probability distributions of the CLUMPY torus model parameters are well constrained for all QSOs except for MR 2251−178, which was modelled with the narrower wavelength range spectrum of GTC/CC. In Table 9 we list the median, 1σ uncertainty and the maximum-a-posterior (MAP) values of the parameters derived from the SED modelling. In this table we also list the reduced χ^2 estimated from fitting both the median and MAP models with the MIR starburst-substrated spectrum.

We find that 50 per cent of QSOs have viewing angles between 50° and 88°, while the other 50 per cent have viewing angles that range from 17° to 47°. A similar analysis on Seyfert 1 galaxies found viewing angles between 50° and 60° with escape probabilities larger than 16 per cent (see e.g. Alonso-Herrero et al. 2011). Nevertheless, in order to better constrain the viewing angle of QSOs, we would need at least two NIR photometry points (Ramos Almeida et al. 2014).

In Table 10 we list P_{esc}, f_2 and the AGN bolometric luminosity derived from the CLUMPY modelling, and we also include the bolometric luminosity estimated from hard X-rays (2–10 keV), using bolometric corrections of Runnoe, Brotherton & Shang (2012), for comparison.

We find that Mrk 509 has an index of the radial density profile ($q \sim 1.9$) and number of clouds along the equatorial ray ($N_0 \sim 8$) consistent with those previously obtained by Hönig et al. (2010), ∼1.5 and ∼7.5, respectively, using the CLUMPY torus models and an extra contribution of hot dust in the inner region of the torus (Hönig & Kishimoto 2010). We note, however, that they did not fit their

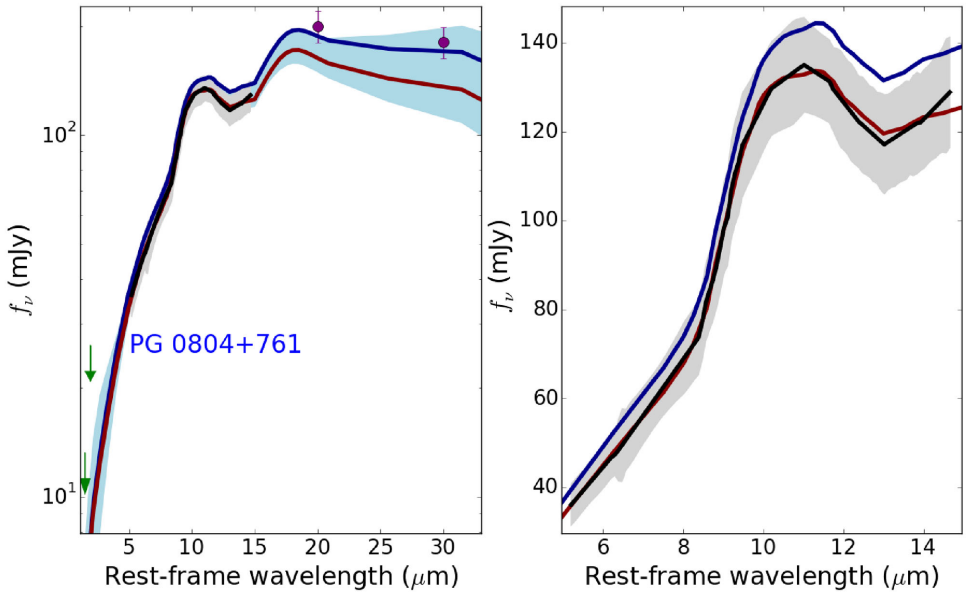

Figure 8. SED of PG 0804+761. Left panel: photometry for the unresolved component (dots and arrows) and starburst-subtracted *Spitzer/IRS* spectrum (black line). The purple dots at 20 and 30 μm are derived from the starburst-subtracted spectrum extrapolating the PAH component obtained from the decomposition analysis. We did not use these data points for the modelling. The blue solid line and blue shaded region represent the best CLUMPY torus model and the range of models within 68 per cent uncertainty in the best-fitted parameters, respectively. The red solid line is the MAP model. Right: enlarged view of the best-fitting models around the 9.7 μm silicate feature. See Appendix E for the rest of the sample.

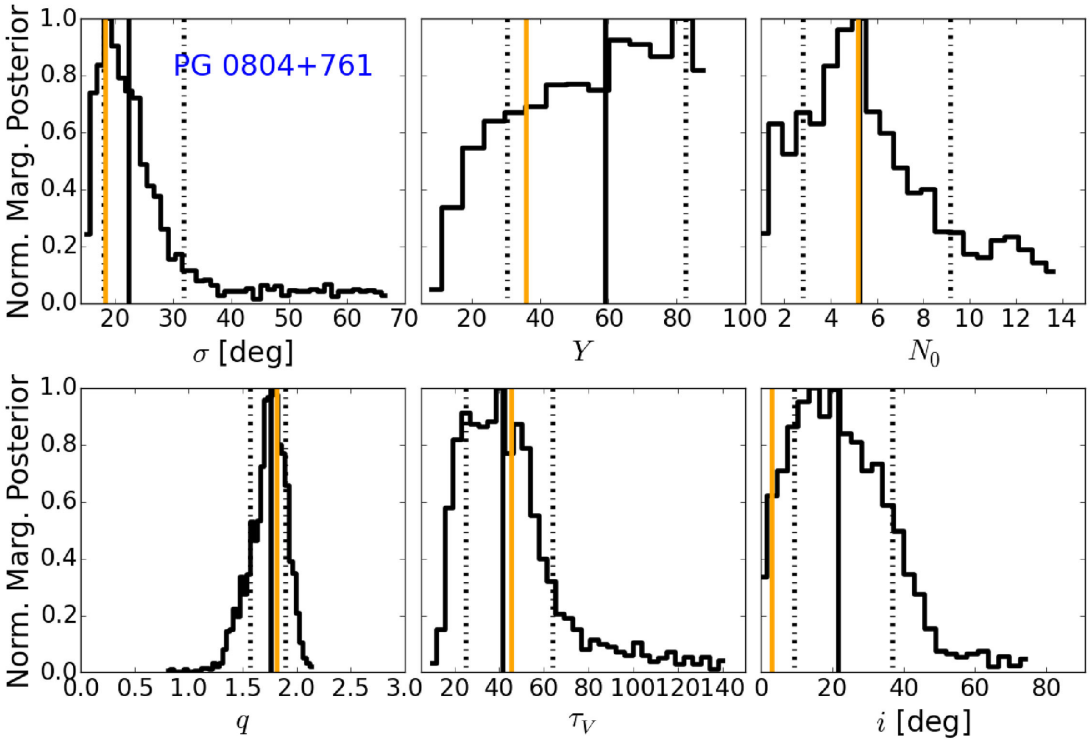

Figure 9. Posterior probability distributions of the CLUMPY parameters for PG 0804+761 in solid black lines. The vertical solid black lines mark the median of the distributions, the dotted black lines represent the 68 per cent confidence intervals, whereas the solid orange line marks the MAP values. Posterior probability distribution for the full sample can be found in Appendix E.

Table 9. Main results of the dusty CLUMPY torus model fitting. Column 1 gives the name of the QSO; columns 2, 4, 6, 8, 10 and 12 the median and the 68 per cent uncertainty level of the posterior probability distributions, while columns 3, 5, 7, 9, 11 and 13 give the MAP model parameters, and columns 14 and 15 the reduced χ^2_ν of the median and MAP models, respectively.

Name	$\sigma_{\rm torus}$		Y		N_0		q		τ_V		i		χ^2_ν	χ^2_ν
	Median (deg.)	MAP (deg.)	Median	MAP	Median	MAP	Median	MAP	Median	MAP	Median (deg.)	MAP (deg.)	(median)	(MAP)
PG 0003+199	31^{+20}_{-9}	43	54^{+27}_{-27}	82	6^{+3}_{-3}	3	$2.5^{+0.3}_{-0.4}$	1.9	77^{+25}_{-21}	67	22^{+20}_{-13}	65	2.15	0.12
PG 0007+106	24^{+4}_{-3}	24	58^{+24}_{-27}	79	6^{+2}_{-3}	3	$2.6^{+0.2}_{-0.3}$	2.1	53^{+12}_{-11}	53	64^{+14}_{-10}	80	0.15	0.09
PG 0050+124	16^{+1}_{-0}	15	67^{+15}_{-12}	58	3^{+1}_{-0}	3	$1.56^{+0.04}_{-0.03}$	1.5	54^{+4}_{-4}	54	79^{+3}_{-3}	80	1.37	1.25
PG 0804+761	22^{+10}_{-4}	18	59^{+23}_{-29}	36	5^{+4}_{-2}	5	$1.8^{+0.1}_{-0.2}$	1.8	42^{+22}_{-17}	46	22^{+15}_{-12}	3	1.37	0.03
PG 0844+349	16^{+1}_{-1}	15	77^{+15}_{-30}	96	2^{+0}_{-0}	1	$1.3^{+0.2}_{-0.1}$	1.3	77^{+25}_{-15}	66	88^{+1}_{-3}	90	0.31	0.21
PG 0923+129	43^{+12}_{-10}	36	60^{+23}_{-25}	79	10^{+3}_{-3}	13	$2.1^{+0.4}_{-0.4}$	2	120^{+10}_{-13}	117	14^{+14}_{-8}	1	1.60	0.30
PG 1211+143	45^{+12}_{-8}	36	40^{+4}_{-3}	39	2^{+0}_{-0}	2	$1.43^{+0.05}_{-0.05}$	1.4	38^{+3}_{-3}	37	80^{+6}_{-10}	88	1.27	1.24
PG 1229+204	16^{+1}_{-1}	15	59^{+20}_{-18}	64	12^{+2}_{-3}	14	$0.53^{+0.10}_{-0.07}$	0.5	20^{+9}_{-5}	14	73^{+2}_{-3}	75	0.94	0.33
PG 1351+640	17^{+3}_{-1}	15	37^{+1}_{-1}	35	8^{+1}_{-1}	9	$0.04^{+0.05}_{-0.03}$	0.01	29^{+3}_{-3}	28	47^{+4}_{-9}	51	2.13	1.77
PG 1411+442	16^{+1}_{-1}	15	58^{+25}_{-28}	74	4^{+1}_{-1}	3	$2.6^{+0.2}_{-0.2}$	2.5	72^{+10}_{-10}	73	86^{+2}_{-5}	90	0.06	0.06
PG 1426+015	19^{+3}_{-2}	19	60^{+23}_{-27}	50	9^{+3}_{-3}	6	$2.0^{+0.4}_{-0.4}$	2.7	118^{+14}_{-23}	125	64^{+9}_{-8}	88	0.80	0.62
PG 1440+356	16^{+1}_{-0}	15	55^{+26}_{-28}	60	3^{+0}_{-0}	3	$2.8^{+0.1}_{-0.2}$	2.9	70^{+9}_{-9}	76	88^{+1}_{-3}	90	0.08	0.06
PG 1448+273	30^{+7}_{-4}	24	57^{+26}_{-26}	60	13^{+1}_{-3}	15	$1.7^{+0.3}_{-0.2}$	1.5	89^{+13}_{-12}	73	10^{+10}_{-6}	1	0.35	0.17
PG 1501+106	58^{+7}_{-8}	52	40^{+32}_{-18}	21	10^{+3}_{-3}	8	$2.6^{+0.2}_{-0.2}$	2.4	113^{+16}_{-14}	110	40^{+23}_{-21}	56	0.42	0.36
PG 1534+580	28^{+15}_{-6}	18	67^{+20}_{-26}	80	11^{+2}_{-3}	15	$1.8^{+0.6}_{-0.3}$	1.5	100^{+31}_{-29}	69	12^{+11}_{-7}	2	1.54	0.35
PG 1535+547	37^{+18}_{-13}	24	52^{+26}_{-25}	30	4^{+4}_{-1}	3	$2.7^{+0.2}_{-0.3}$	2.3	80^{+13}_{-14}	66	47^{+19}_{-22}	79	0.19	0.06
PG 2130+199	17^{+2}_{-1}	16	64^{+22}_{-25}	94	5^{+1}_{-1}	4	$2.0^{+0.3}_{-0.2}$	1.8	50^{+8}_{-7}	46	86^{+3}_{-4}	88	0.07	0.04
PG 2214+139	46^{+14}_{-18}	29	54^{+25}_{-25}	45	2^{+1}_{-0}	2	$2.3^{+0.2}_{-0.2}$	2.1	64^{+25}_{-16}	50	52^{+21}_{-27}	85	2.67	0.19
Mrk 509	38^{+14}_{-10}	61	59^{+23}_{-26}	85	8^{+4}_{-3}	2	$1.9^{+0.6}_{-0.4}$	1.2	99^{+22}_{-29}	58	17^{+15}_{-10}	60	2.73	0.18
MR 2251−178	37^{+16}_{-11}	36	46^{+29}_{-26}	67	7^{+4}_{-3}	10	$1.9^{+0.6}_{-0.7}$	0.7	103^{+25}_{-43}	70	28^{+18}_{-16}	1	0.94	0.63

Table 10. Parameters derived from the CLUMPY free parameters: column 1, name of the QSO; column 2, escape probability; column 3, covering factor; and column 4, bolometric luminosity. Column 5 gives the range of bolometric luminosities estimated using hard X-ray (2–10 keV) fluxes from the literature.

Name	P_{esc} (per cent)	f_2	L_{bol} CLUMPY ($\times 10^{44}$ erg s^{-1})	$^{\star}L_{bol}$ Obs. ($\times 10^{44}$ erg s^{-1})
PG 0003+199	92^{+8}_{-51}	$0.3^{+0.2}_{-0.1}$	$3.0^{+0.4}_{-0.2}$	(3–12)
PG 0007+106	13^{+30}_{-8}	$0.20^{+0.1}_{-0.04}$	24^{+8}_{-4}	(20–90)
PG 0050+124	16^{+6}_{-4}	$0.06^{+0.01}_{-0.04}$	40^{+8}_{-8}	(10–50)
PG 0804+761	99^{+1}_{-8}	$0.2^{+0.1}_{-0.1}$	30^{+2}_{-3}	(50–190)
PG 0844+349	22^{+3}_{-3}	$0.040^{+0.01}_{-0.004}$	$2.2^{+0.3}_{-0.2}$	(10–37)
PG 0923+129	62^{+35}_{-44}	$0.7^{+0.2}_{-0.2}$	21^{+2}_{-2}	(6–23)
PG 1211+143	13^{+3}_{-2}	$0.4^{+0.1}_{-0.1}$	59^{+6}_{-9}	(9–33)
PG 1229+204	3^{+7}_{-2}	$0.1^{+0.01}_{-0.01}$	45^{+12}_{-8}	(5–21)
PG 1351+640	99^{+1}_{-1}	$0.10^{+0.04}_{-0.01}$	$8.6^{+0.7}_{-0.7}$	(3–11)
PG 1411+442	4^{+2}_{-1}	$0.10^{+0.01}_{-0.01}$	59^{+6}_{-9}	(4–17)
PG 1426+015	29^{+45}_{-25}	$0.14^{+0.02}_{-0.04}$	45^{+12}_{-8}	(20–80)
PG 1440+356	4^{+1}_{-1}	$0.070^{+0.01}_{-0.004}$	86^{+7}_{-7}	(10–40)
PG 1448+273	99^{+1}_{-19}	$0.4^{+0.2}_{-0.1}$	$5.7^{+0.5}_{-0.5}$	(3–13)
PG 1501+106	1^{+7}_{-1}	$0.9^{+0.1}_{-0.1}$	$6.1^{+0.8}_{-0.4}$	(9–33)
PG 1534+580	99^{+1}_{-35}	$0.3^{+0.3}_{-0.1}$	21^{+3}_{-4}	(4–16)
PG 1535+547	33^{+47}_{-21}	$0.4^{+0.2}_{-0.2}$	$0.23^{+0.06}_{-0.03}$	(0.4–1.6)
PG 2130+099	2^{+1}_{-1}	$0.09^{+0.02}_{-0.01}$	$5.9^{+0.7}_{-0.7}$	(6–22)
PG 2214+139	42^{+47}_{-14}	$0.3^{+0.1}_{-0.2}$	14^{+3}_{-2}	(10–40)
MR 2251−178	70^{+28}_{-51}	$0.4^{+0.3}_{-0.2}$	72^{+18}_{-12}	(50–190)
Mrk 509	84^{+7}_{-1}	$0.5^{+0.2}_{-0.2}$	76^{+10}_{-10}	(80–320)

MIR spectra but rather compared with a subset of models deemed to be appropriate for Seyfert 1 galaxies.

PG 1211+143 was also previously modelled by Nikutta et al. (2009) with the CLUMPY models. Three of the torus parameters (N_0=2–9, σ_{torus}=15–60° and $i = 0 - 70°$) are consistent within the uncertainties with our results, while we find a different index of the radial density distribution and larger optical depths (q = 0–0.5 and τ_V = 20–30). These differences probably arise because they fixed the radial extent to $Y = 20$ while we allowed this parameter to vary freely.

As a sanity check, we also performed the fits for individual QSOs with the new CLUMPY models that use 3D radiative transfer on spherical clouds, available in their web page, and found that the parameters are the same as with the 2008 models within the derived 1-sigma uncertainties.

8 DISCUSSION

8.1 Global torus properties of QSOs

In order to study the QSO sample as a whole, we build global probability distributions for each parameter by bootstrapping on the parameters returned by the MCMC procedure for each QSO 10 000 times, and creating a parent distribution of 19 QSOs 10 000 times values to derive the distributions. We exclude MR 2251−178 from the global analysis since the posterior distributions of its parameters are less constrained due to the narrower spectral range used in the analysis. We build the global probability distributions for type 1 and 2 Seyfert nuclei in the same manner, using the individual arrays of values obtained in the analysis published by Ichikawa et al. (2015) (A. Asensio-Ramos, private communication). In Fig. 10 we show the global probability distributions of QSOs, type 1 and 2 Seyferts. The median values of the distributions and their 68 per cent confidence intervals are listed in Table 11.

We observe that the global probability distributions cover a wide range of values. In particular, the escape probability for QSOs, which depends on the number of clouds along the LOS (N_{LOS}), the viewing angle (i) and the angular width (σ_{torus}), shows a peak below 0.1 (five objects with $P_{esc} < 5$ per cent), a secondary peak around 0.2 (seven QSOs with $10 < P_{esc} < 70$ per cent), and a peak above 0.7 (seven QSOs with $P_{esc} > 70$ per cent). Nevertheless, better constrains on the viewing angle (i) could result in better constrains on the escape probability distribution. The geometrical covering factor, which is independent of the viewing angle, however, is well constrained towards low values (median of $f_2 \sim 0.2$). Therefore, QSOs display a wide range of global CLUMPY model properties (σ_{torus}, N_0 and i) in combinations such that P_{esc} and f_2 allow for enough AGN-produced photons to escape the dusty structure and the broad lines to be seen in direct light, resulting in a type 1 QSO.

A qualitative comparison of the CLUMPY model parameters for QSOs with those of Seyfert 1 and 2s shows that the distribution of number of clouds N_0 is skewed in QSOs towards lower values than in Seyfert galaxies, and they are more concentrated towards the inner regions of the torus (larger q values). The optical thickness of the clouds (τ_v) is lower than in Seyfert 1s and comparable to Seyfert 2s. The values of σ_{torus} in QSOs and Seyfert 1s, however, are more similar, albeit with different parent distributions. The Y parameter peaks at lower values in Seyfert galaxies than in QSOs, although it is not possible to strictly compare the distributions since Ichikawa et al. (2015) constrain its range between 0 and 30, while we allowed it to vary between 0 and 100, and indeed, we note that the global distribution of Y for Seyfert 1s is truncated at 30. The viewing angle

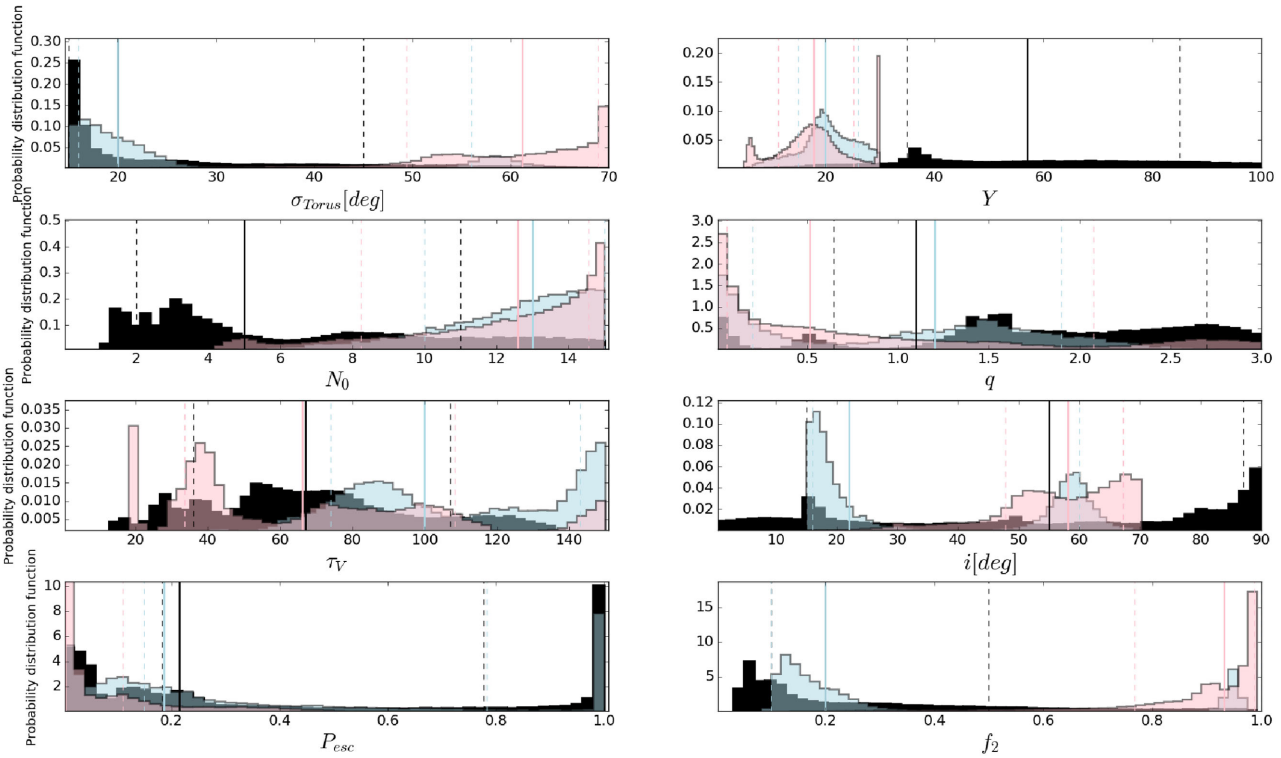

Figure 10. Global probability distributions of the CLUMPY torus parameters for our QSO sample (black) compared with those of type 1 Seyfert nuclei (blue, four objects) and type 2 Seyfert nuclei (pink) from Ichikawa et al. (2015). The solid vertical lines represent the median values of the distributions, and the dashed black line shows the 68 per cent confidence interval of the distributions around the median. For Seyfert 1 and 2 the parameter Y was fitted using a range between 5 and 30, which is different from the range used for QSOs (5–100).

Table 11. Median and 68 per cent confidence intervals of the global CLUMPY model parameters for QSOs, type 1 Seyfert nuclei and type 2 Seyfert nuclei (red). *The parameter was fitted using a range between 5 and 30, which is different from the range used for QSOs (5–100).

AGN	$\sigma_{\rm torus}$ (deg.)	Y	N_0	q	τ_V	i (deg)	$P_{\rm esc}$ (per cent)	f_2
QSO	20^{+25}_{-5}	57^{+28}_{-22}	5^{+6}_{-3}	$1.9^{+0.8}_{-0.6}$	67^{+40}_{-31}	55^{+32}_{-40}	$0.2^{+0.8}_{-0.2}$	$0.2^{+0.3}_{-0.1}$
Seyfert 1	20^{+36}_{-4}	$*20^{+6}_{-5}$	13^{+2}_{-3}	$1.2^{+0.7}_{-1.0}$	100^{+43}_{-26}	22^{+38}_{-6}	$0.2^{+0.8}_{-0.1}$	$0.2^{+0.8}_{-0.1}$
Seyfert 2	61^{+7}_{-11}	$*18^{+6}_{-7}$	13^{+2}_{-4}	$0.5^{+1.6}_{-0.5}$	66^{+42}_{-32}	58^{+9}_{-10}	$0.005^{+0.1}_{-0.005}$	$0.9^{+0.1}_{-0.2}$

is approximately 1.5 times larger in QSOs than in Seyfert 1s, but the median values of $P_{\rm esc}$ and f_2 are similar in QSOs and Seyfert 1s.

To quantitatively compare the probability distributions of the parameters, we use the two-sample Kolmogorov–Smirnov test to determine the probability of rejecting the null hypothesis that two samples are drawn from the same parent population. For all free parameters ($\sigma_{\rm torus}$, Y, N_0, q, i, τ_V) of Seyfert 1 and 2, the null hypothesis can be rejected with a negligible probability ($P < 10^{-100}$). Likewise $P_{\rm esc}$ and f_2 have statistically different parent distributions, and the null hypothesis can again be rejected with $P < 10^{-100}$. These probabilities are so small due, in part, to the large number of samples in the global distributions that map the posterior probability distributions of individual AGN, but caution is drawn to the fact that the distributions have been derived from only ∼10–20 objects for QSOs and Seyfert 2, and four for Seyfert 1.

Additionally, we use the *Mann–Whitney* (Stuart & Ord 1994) test to statistically measure the similitude between the medians of distributions. Although for QSOs and Seyfert 1s the medians look similar in $\sigma_{\rm torus}$, $P_{\rm esc}$ and f_2 parameters, they are statistically distinct ($P < 10^{-7}$), and QSOs do have a tendency for larger escape probabilities and lower covering factors than Seyfert 1 nuclei.

These results are consistent with fundamental geometrical differences between high luminosity type 1 AGN (QSOs) and their lower luminosity counterparts (Seyfert 1s), and between those type 2 AGN.

The low number of clouds along the equatorial ray (N_0), large index of the radial distribution (q) and lower optical thickness (τ_V) suggest that the clouds in the tori of QSOs might have been partially evaporated and piled away by the high radiation field of the QSOs, as proposed by the receding torus scenario (Lawrence et al. 1991).

8.2 Dependence of AGN covering factor on AGN luminosity

Several works (e.g. Ueda et al. 2003; La Franca et al. 2005; Gilli, Comastri & Hasinger 2007; Fiore et al. 2008; Hasinger 2008) have found that the fraction of type 2 AGN decreases with increasing AGN luminosity, and this result can be interpreted as giving support to a model in which the torus recedes due to the higher intensity radiation field (Lawrence et al. 1991). However, these works have used the fraction of absorbed AGN from X-ray or optical broad lines, which could be affected by absorption along the LOS due to dust

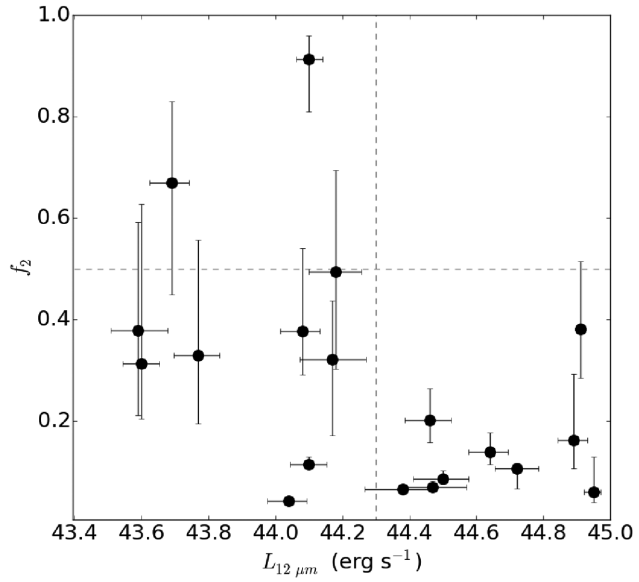

Figure 11. Geometrical covering factor f_2 as a function of the IR luminosity at 12 μm.

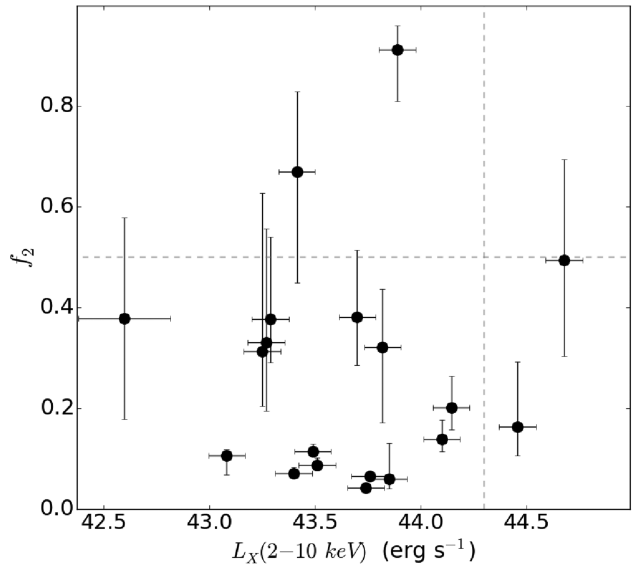

Figure 12. Geometrical covering factor as a function of the hard (2–10 keV) X-ray luminosity.

in the host galaxy or dust-free ionized gas (see Rowan-Robinson, Valtchanov & Nandra 2009, and references therein).

Using a large X-ray and IR selected sample of AGN, Rowan-Robinson et al. (2009) studied the X-ray-infrared correlation. They found that their data are well reproduced by a model in which the median covering factor decreases from high ($\log_{10}L_X > 44.5$) to moderate ($\log_{10}L_X = 42.5 - 44.5$) X-ray luminosities and then increases towards low luminosities ($\log_{10}L_X = 42.5$).

In our sample, we find that objects with lower ($\log_{10}L < 44.3$) IR and X-ray luminosity have a wide range of covering factors, reaching up to the highest values (Figs 11 and 12). These 12 μm luminosities are hence dominated by the dusty torus emission. In particular, we note that PG 1501+106, the QSO with the highest f_2 value, is among the objects with low IR and X-ray emission. The high luminosity and high covering factor region of this relationship, $f_2 > 0.5$ and $L_{12} > 44.3$, is devoid of QSOs. Although only 20 objects have been included in this comparison, the absence of QSOs in this region is significant. If both quantities were to be completely unrelated, we would expect a scatter plot covering all values, with a mean of 7.6 objects falling in the $f_2 > 0.5$ and $L_{12} > 44.2$ region in the case of f_2 versus $L_{12\,\mu m}$ relationship. The probability of finding in a sample 0 objects when 7.6 are expected is $P < 0.05$ per cent, assuming a Poisson distribution. Hence the highest-luminosity AGN have a high tendency to have cleaner LOSs. We note that the two QSOs with $f_2 > 0.5$ (PG 0923+129 and PG 1501+106) are 1.2 and 1.5 type objects. The median covering factor of QSOs is $0.2^{+0.3}_{-0.1}$ and this value is consistent, within the uncertainties, with the 35–40 per cent derived by Rowan-Robinson et al. (2008, 2009) for a sample of QSOs with $\log_{10}L_X$ in the range of 42.5 to 44.5 erg s^{-1}.

Recently, Mateos et al. (2016) used a large sample of AGN from the Bright Ultra-hard *XMM–Newton* Survey that includes type 1s, type 2s and intermediate AGN. The torus emission of this sample was modelled using the CLUMPY models of Nenkova et al. (2008a,b). All free parameters were allowed to vary within the same range as we used for our sample of QSOs, except the radial extend (Y), that was constrained a priori between 5 and 30. They found that type 2 AGN present on average higher (>0.5) geometrical covering factors than type 1 AGN (<0.5), but they also found that ∼20 per cent of type 1 AGN have covering factors larger than 0.5 and that the ∼28 per cent of type 2 AGN have covering factors lower than 0.5. These results are consistent with ours, since most QSOs in our sample have covering factors $f_2 < 0.5$.

8.3 Excess NIR and MIR emission: starburst, hot dust or accretion disc?

Since CLUMPY models only take into account the emission of the dusty torus we have done our best to exclude any extended NIR and MIR emission. However, in Section 6 we found that for some QSOs the unresolved NIR emission is not well reproduced by CLUMPY models. Among them, PG 1440+356 has the most prominent PAH emission, observed in both *Spitzer/IRS* and GTC/CC spectra (see Fig. C1), and PG 0050+124 presents clear extended emission at NIR (Surace & Sanders 1999) and MIR wavelengths (Burtscher et al. 2013, and this work, see Fig. B1). Therefore, it is likely that in these objects the extended NIR emission has not been properly accounted to estimate the unresolved emission, or it could also be hot dust associated with the NLR (Mor et al. 2009; Hönig et al. 2010; Hernán-Caballero et al. 2016; Mateos et al. 2016). Similar results have been reported in the modelling of the unresolved NIR SED of some Seyfert 1s (e.g. Alonso-Herrero et al. 2011; Ichikawa et al. 2015) suggesting that in type 1 AGN it is more difficult to constrain the emission from dust heated by the AGN. Another possible explanation is that a power law is not adequate to represent the intrinsic AGN emission in the NIR (Hernán-Caballero et al. 2016; Mateos et al. 2016).

9 CONCLUSIONS

The MIR imaging of our sample of 20 nearby QSOs reveals that the majority of them are unresolved at ∼0.3 arcsec resolution, corresponding to physical scales of $\lesssim$600 pc. We compare the *Spitzer/IRS* and the ground-based high-angular resolution spectra and find that the spectral shapes are similar, and hence adopt the former to characterize the AGN component. We find that on average the AGN contributes 85 per cent of the total MIR emission within the *Spitzer/IRS* apertures, while the rest can be attributed to starburst emission.

These results indicate that at MIR wavelengths the QSO emission is largely dominated by dust heated by the AGN.

We use the unresolved NIR emission and the starburst-subtracted MIR spectra to constrain the physical and geometrical parameters of CLUMPY dusty torus models. Using Bayesian inference we derive the posterior probability distributions of the six free parameters of the CLUMPY models and build the global probability distributions of the parameters for the QSO sample. We find that for most QSOs CLUMPY models reproduce well the AGN emission without the inclusion of a hot dust component, as proposed in the literature.

A statistical analysis reveals that the properties of the dusty torus are intrinsically different from those of Seyfert 1 and Seyfert 2 nuclei (e.g. Ramos Almeida et al. 2011; Ichikawa et al. 2015). Nevertheless, in QSOs the combination of the width of torus, number of clouds and inclination $\sigma_{\rm torus}$, N_0 and i results in escape probabilities $P_{\rm esc} \gtrsim 5$ per cent and covering factors $f_2 \lesssim 0.6$, which are consistent with the optical classification of QSOs as type 1 AGN. Higher luminosity QSOs have the lowest covering factor f_2. We conclude that the lower number of clouds, steeper radial distribution and less optically thick clouds in QSOs can be interpreted as dusty structures that have been partly evaporated and piled up by the higher intensity radiation field in QSOs, as proposed by a receding torus scenario.

ACKNOWLEDGEMENTS

We thank the referee of this article for insightful comments that allowed us to improve the manuscript. This work has been partly supported by Mexican CONACyT grant CB-2011-01-167291. MMP acknowledges support by the CONACyT PhD fellowship and UNAM-DGAPA postdoctoral fellowship. OG-M acknowledges support by the PAPIIT IA100516 grant. AA-H acknowledges financial support from the Spanish Ministry of Economy and Competitiveness through the Plan Nacional de Astronomía y Astrofísica through grant AYA2015-64346-C2-1-P and from CSIC/PIE grant 201650E036. CRA acknowledges the Ramón y Cajal Program of the Spanish Ministry of Economy and Competitiveness through project RYC-2014-15779. KI acknowledges support by JSPS fellowship for young researchers (PD). This work is based on observations made with the 10.4-m GTC located in the Spanish Observatorio del Roque de Los Muchachos of the Instituto de Astrofísica de Canarias, in the island La Palma. It is also based partly on observations obtained with the *Spitzer Space Observatory*, which is operated by JPL, Caltech, under NASA contract 1407. This research has made use of the NASA/IPAC Extragalactic Database (NED) which is operated by JPL, Caltech, under contract with the National Aeronautics and Space Administration. CASSIS is a product of the Infrared Science Center at Cornell University, supported by NASA and JPL.

REFERENCES

Alonso-Herrero A. et al., 2011, ApJ, 736, 82
Alonso-Herrero A. et al., 2016a, MNRAS, 455, 563
Alonso-Herrero A. et al., 2016b, MNRAS, 463, 2405
Antonucci R., 1993, ARA&A, 31, 473
Asensio Ramos A., Ramos Almeida C., 2009, ApJ, 696, 2075
Barvainis R., Lonsdale C., Antonucci R., 1996, AJ, 111, 1431
Bianchi S., Bonilla N. F., Guainazzi M., Matt G., Ponti G., 2009, A&A, 501, 915
Bicay M. D., Kojoian G., Seal J., Dickinson D. F., Malkan M. A., 1995, ApJS, 98, 369
Burtscher L. et al., 2013, A&A, 558, AA149
Cohen J. G., 1999, AJ, 117, 2428
Deo R. P. et al., 2011, ApJ, 729, 108
Dudik R. P. et al., 2007, ApJ, 664, 71
Edelson R. A., 1987, AJ, 94, 1150
Efstathiou A., Rowan-Robinson M., 1995, MNRAS, 273, 649
Feltre A., Hatziminaoglou E., Fritz J., Franceschini A., 2012, MNRAS, 426, 120
Fiore F. et al., 2008, ApJ, 672, 94
Fischer S., Iserlohe C., Zuther J., Bertram T., Straubmeier C., Schödel R., Eckart A., 2006, A&A, 452, 827
Fuller L. et al., 2016, MNRAS, 462, 2618
Gallo L. C., 2006, MNRAS, 368, 479
Gandhi P., Horst H., Smette A., Hönig S., Comastri A., Gilli R., Vignali C., Duschl W., 2009, A&A, 502, 457
García-Burillo S. et al., 2016, ApJ, 823, L12
Gilli R., Comastri A., Hasinger G., 2007, A&A, 463, 79
González-Martín O. et al., 2013, A&A, 553, 35
González-Martín O. et al., 2015, A&A, 578, A74
Granato G. L., Danese L., 1994, MNRAS, 268, 235
Green R. F., Schmidt M., Liebert J., 1986, ApJS, 61, 305
Guyon O., Sanders D. B., Stockton A., 2006, ApJS, 166, 89
Hao L. et al., 2005, ApJ, 625, L75
Hasinger G., 2008, A&A, 490, 905
Hernán-Caballero A. et al., 2015, ApJ, 803, 109
Hernán-Caballero A., Hatziminaoglou E., Alonso-Herrero A., Mateos S., 2016, MNRAS, 463, 2064
Heymann F., Nikutta R., Elitzur M., 2014, new CLUMPY models
Hodapp K.-W. et al., 1996, New Astron., 1, 177
Hönig S. F., Kishimoto M., 2010, A&A, 523, A27
Hönig S. F., Kishimoto M., Gandhi P., Smette A., Asmus D., Duschl W., Polletta M., Weigelt G., 2010, A&A, 515, AA23
Horst H., Smette A., Gandhi P., Duschl W. J., 2006, A&A, 457, L17
Horst H., Gandhi P., Smette A., Duschl W. J., 2008, A&A, 479, 389
Houck J. R. et al., 2004, ApJS, 154, 18
Ichikawa K., Ueda Y., Terashima Y., Oyabu S., Gandhi P., Matsuta K., Nakagawa T., 2012, ApJ, 754, 45
Ichikawa K. et al., 2015, ApJ, 803, 57
Ichikawa K., Ricci C., Ueda Y., Matsuoka K., Toba Y., Kawamuro T., Trakhtenbrot B., Koss M. J., 2017, ApJ, 835, 74
Jaffe W., Meisenheimer K., Röttgering H., Leinert C., Richichi A., 2004, The Interplay Among Black Holes, Stars and ISM in Galactic Nuclei. IAUS 222, Astron. Soc. Pac., San Francisco, p. 37
Kellermann K. I., Sramek R. A., Schmidt M., Green R. F., Shaffer D. B., 1994, AJ, 108, 1163
Krabbe A., Böker T., Maiolino R., 2001, ApJ, 557, 62
Krolik J. H., Begelman M. C., 1988, ApJ, 329, 702
La Franca F. et al., 2005, ApJ, 635, 864
Laurent-Muehleisen S. A., Kollgaard R. I., Ryan P. J., Feigelson E. D., Brinkmann W., Siebert J., 1997, A&AS, 122, 235
Lawrence A., Rowan-Robinson M., Efstathiou A., Ward M. J., Elvis M., Smith M. G., Duncan W. D., Robson E. I., 1991, MNRAS, 248, 91
Lebouteiller V., Barry D. J., Spoon H. W. W., Bernard-Salas J., Sloan G. C., Houck J. R., Weedman D. W., 2011, ApJS, 196, 8
Levenson N. A., Sirocky M. M., Hao L., Spoon H. W. W., Marshall J. A., Elitzur M., Houck J. R., 2007, ApJ, 654, L45
Lord S. D., 1992, NASA Tech. Memo 103957
Lutz D., Maiolino R., Spoon H. W. W., Moorwood A. F. M., 2004, A&A, 418, 465
Martínez-Paredes M. et al., 2015, MNRAS, 454, 3577
Mason R. E., Geballe T. R., Packham C., Levenson N. A., Elitzur M., Fisher R. S., Perlman E., 2006, ApJ, 640, 612
Mason R. E. et al., 2012, AJ, 144, 11
Mateos S. et al., 2016, ApJ, 819, 166
Meisenheimer K. et al., 2007, A&A, 471, 453
Mor R., Netzer H., 2012, MNRAS, 420, 526
Mor R., Trakhtenbrot B., 2011, ApJ, 737, L36
Mor R., Netzer H., Elitzur M., 2009, ApJ, 705, 298
Nenkova M., Ivezić Ž., Elitzur M., 2002, ApJ, 570, L9

Nenkova M., Sirocky M. M., Ivezić Ž., Elitzur M., 2008a, ApJ, 685, 147
Nenkova M., Sirocky M. M., Nikutta R., Ivezić Ž., Elitzur M., 2008b, ApJ, 685, 160
Netzer H., 2008, Mem. Soc. Astron. Italiana, 79, 1083
Neugebauer G., Green R. F., Matthews K., Schmidt M., Soifer B. T., Bennett J., 1987, ApJS, 63, 615
Nikutta R., Elitzur M., Lacy M., 2009, ApJ, 707, 1550
Packham C., Telesco C. M., Hough J. H., Ftaclas C., 2005, Rev. Mex. Astron. Astrofis. Conf. Ser., 24, 7
Packham C., Telesco C. M., 2007, Revista Mexicana de Astronomia y Astrofisica Conference Series, 29, 9
Peng C. Y., 2002, AJ, 124, 294
Piconcelli E., Guainazzi M., 2005, A&A, 442, L53
Pier E. A., Krolik J. H., 1992, ApJ, 401, 99
Radomski J. T. et al., 2008, ApJ, 681, 141
Ramos Almeida C., Pérez García A. M., Acosta-Pulido J. A., Rodríguez Espinosa J. M., 2007, AJ, 134
Ramos Almeida C. et al., 2009, ApJ, 702, 1127
Ramos Almeida C. et al., 2011, ApJ, 731, 92
Ramos Almeida C., Alonso-Herrero A., Levenson N. A., Asensio R. A., Rodríguez Espinosa J. M., González-Martín O., Packham C., Martínez M., 2014, MNRAS, 439, 3847
Reach W. T. et al., 2005, PASP, 117, 978
Rowan-Robinson M., 1977, ApJ, 213, 635
Rowan-Robinson M. et al., 2008, MNRAS, 386, 697
Rowan-Robinson M., Valtchanov I., Nandra K., 2009, MNRAS, 397, 1326
Runnoe J. C., Brotherton M. S., Shang Z., 2012, MNRAS, 426, 2677
Schinnerer E., Eckart A., Tacconi L. J., 1998, ApJ, 500, 147
Schmidt M., Green R. F., 1983, ApJ, 269, 352
Schweitzer M. et al., 2006, ApJ, 649, 79
Schweitzer M. et al., 2008, ApJ, 679, 101-117
Shu X. W., Yaqoob T., Wang J. X., 2010, ApJS, 187, 581
Stalevski M., Fritz J., Baes M., Nakos T., Popovic L. C., 2012, Publications de l'Observatoire Astronomique de Beograd, Vol. 91, Dullemond, p. 235
Stuart A., Ord J. K., 1994, Kendall's Advanced Theory of Statistics, Vol. 1: Distribution theory, 6th edn. Hodder Arnold, London
Sturm E., Lutz D., Verma A., Netzer H., Sternberg A., Moorwood A. F. M., Oliva E., Genzel R., 2002, A&A, 393, 821
Surace J. A., Sanders D. B., 1999, ApJ, 512, 162
Surace J. A., Sanders D. B., Evans A. S., 2001, AJ, 122, 2791
Telesco C. M. et al., 2003, Proc. SPIE Conf. Ser. Vol. 4841, CanariCam: A Multimode Mid-Infrared Camera for the Gran Telescopio CANARIAS. SPIE, Bellingham, p. 913
Tristram K. R. W. et al., 2007, A&A, 474, 837
Ueda Y., Akiyama M., Ohta K., Miyaji T., 2003, ApJ, 598, 886
Urry M., 2003, in Collin S., Combes F., Shlosman I., eds, ASP Conf. Ser. Vol. 290, Active Galactic Nuclei: From Central Engine to Host Galaxy. Astron. Soc. Pac., San Francisco, p. 3
Urry C. M., Padovani P., 1995, PASP, 107, 803
Veilleux S., 2006, ASP Conf. Ser. Vol. 357, Evolution of Activity in Massive Gas-Rich Mergers. Astron. Soc. Pac., San Francisco, p. 231
Veilleux S. et al., 2009a, ApJS, 182, 628
Veilleux S. et al., 2009b, ApJ, 701, 587
Véron-Cetty M.-P., Véron P., 2010, A&A, 518, A10
Werner M. W. et al., 2004, ApJS, 154, 1
Zhou X.-L., Zhang S.-N., 2010, ApJ, 713, L11

APPENDIX A: EXTENDED EMISSION

PG 0050+124 has a radial profile which is clearly more extended than the radial profile of the standard star, as can be seen in Fig. 3. Therefore, for this object we model the brightness profile using the 2D algorithm GALFIT (Peng 2002). For that we assume the following models: (1) a Sérsic and PSF components with all parameters left to vary freely; (2) a Sérsic component with all parameters allowed to vary, except the index of the brightness profile n, which we assume as $n = 1$, plus a PSF component with its parameters free; and (3) a Sérsic profile with $n = 4$ and a PSF component with free parameters. We find that the model that best reproduces the MIR emission of PG 0050+124 with a reduced $\chi^2_\nu \sim 1$ is the one that includes a Sérsic component with $n = 4$ plus a PSF. The flux in the residual image is ∼1.8 per cent. The parameters of the Sérsic component and the extended and unresolved emission are listed in Table A1. These parameters are consistent with those found by Veilleux (2006) at H band using *HST*/NICMOS images. The uncertainties reported in Table A1 are the standard deviation of the values given by all models. The unresolved plus Sérsic flux of PG 0050+124 measured with GALFIT is similar, within the uncertainties, to that measured directly on the image inside an aperture radius of 1 arcsec. The residual image (see Fig. 3) reveals the possible presence of a ring in PG 0050+124. Indeed, Schinnerer, Eckart & Tacconi (1998) detected a ring using observations of ^{12}CO(2–1) and ^{13}CO(1–0) lines with the four antennas of the Plateau de Bure interferometer from IRAM. However, the size of the apparent ring (∼1 arcsec of diameter) observed in the residual image of CC does not fit the size of the ring (1.6 arcsec of diameter) reported by Schinnerer et al. (1998). On the other hand, this extended emission could alternatively be related to the silicate extended region proposed by Schweitzer et al. (2008).

Table A1. Results from the GALFIT modelling using a PSF + Sérsic profile model for PG 0050+124 in the Si2 band (8.7 μm). Column 1, unresolved nuclear emission; column 2, integrated flux of the Sérsic component; column 3, index of the Sérsic profile (*for the 1.60 and 2.22 μm model the index was fixed); column 4, effective radius of the Sérsic component; column 5, axis ratio of the Sérsic component; column 6, PA of the major axis of the Sérsic component measured East to North.

$f_{\rm unresol}$ (mJy)	$f_{\rm Sersic}$ (mJy)	n	$r_{\rm eff}$ (pc)	a/b	PA (deg)
57 ± 1	173 ± 1	4*	1520 ± 210	0.99 ± 0.03	35 ± 6

APPENDIX B: RADIAL PROFILES

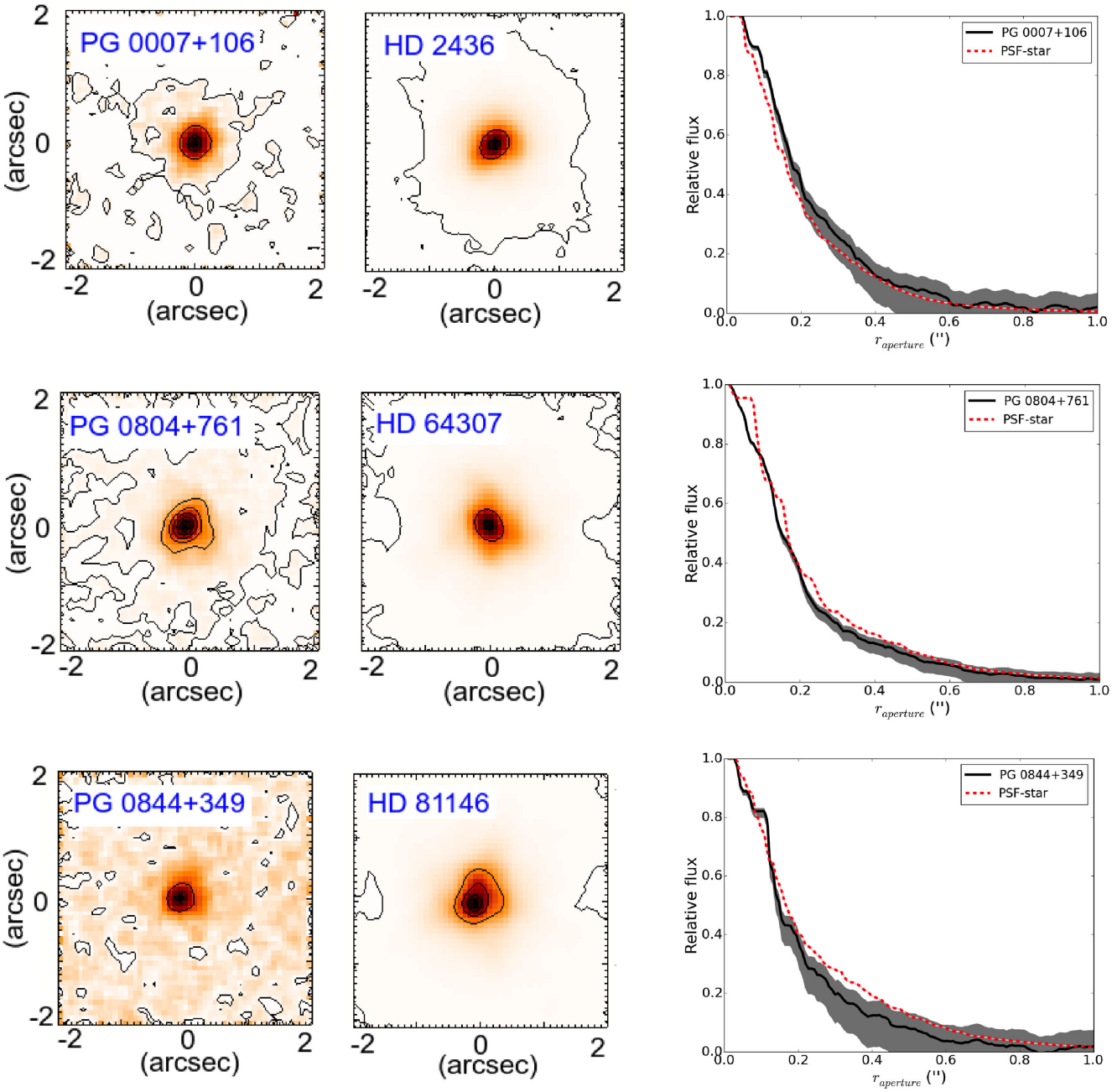

Figure B1. Si2 image for the target (left), standard star (middle) and radial profiles (right). Each object in our sample is shown in a different line.

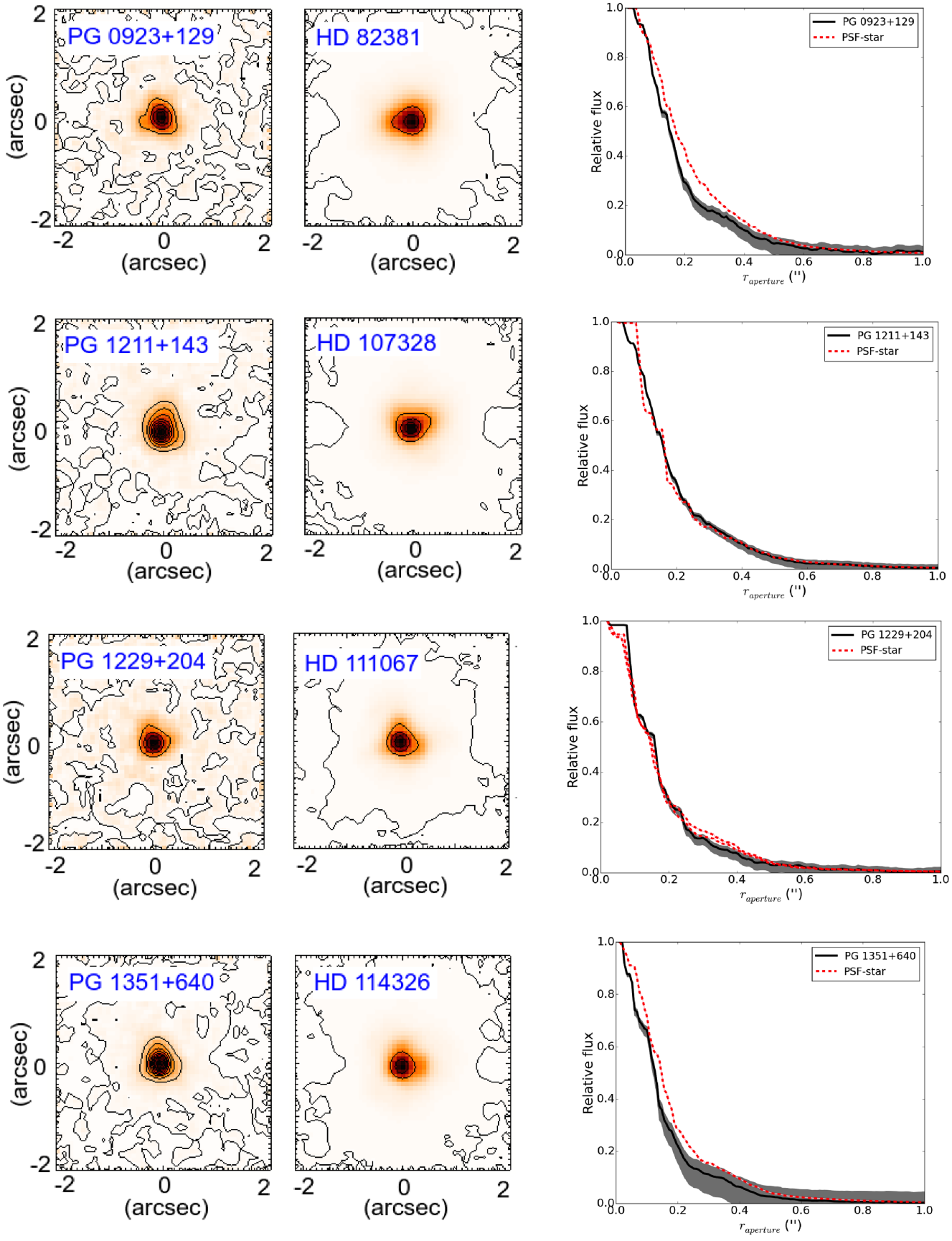

Figure B1 – *continued*

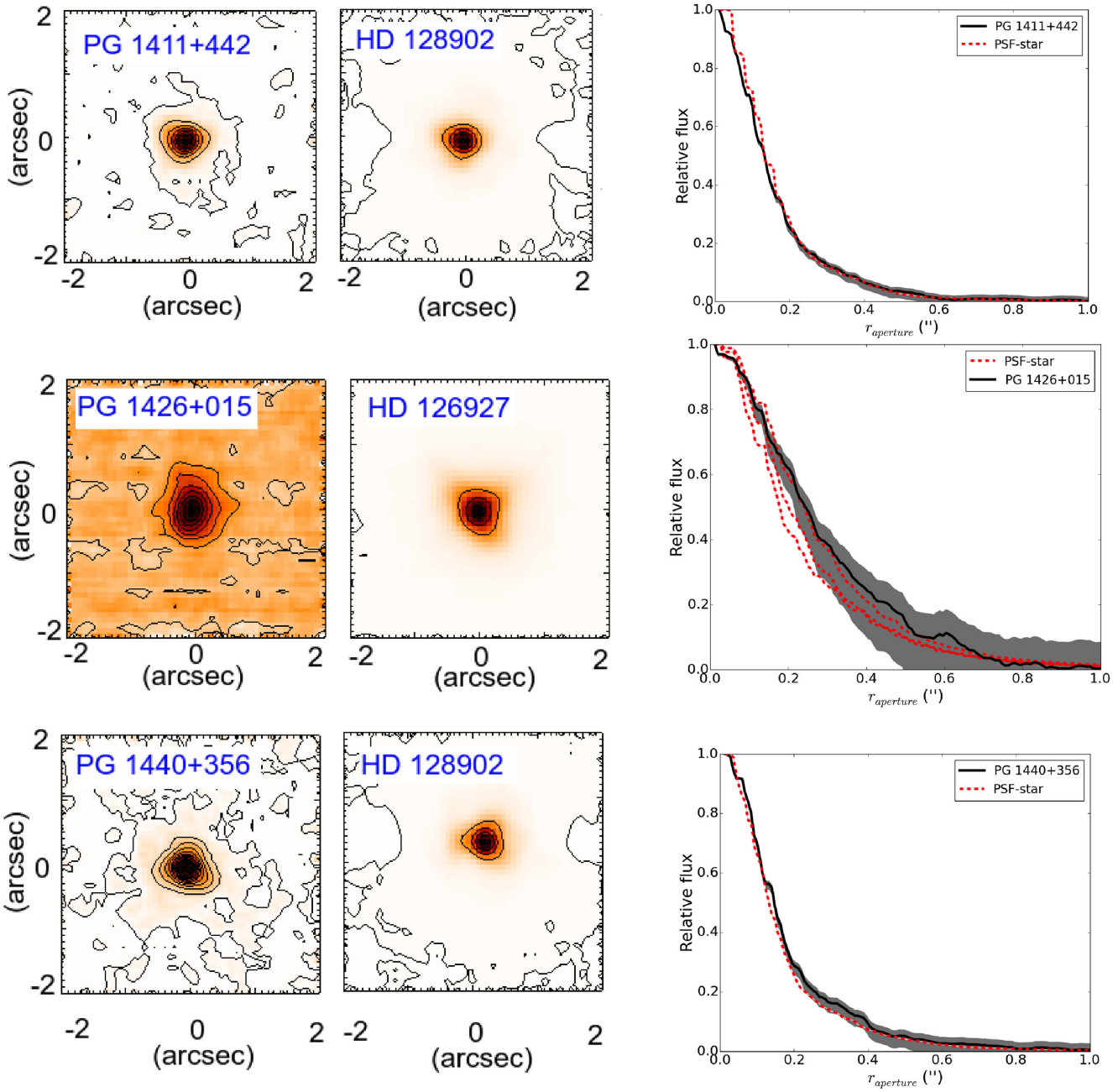

Figure B1 – *continued*

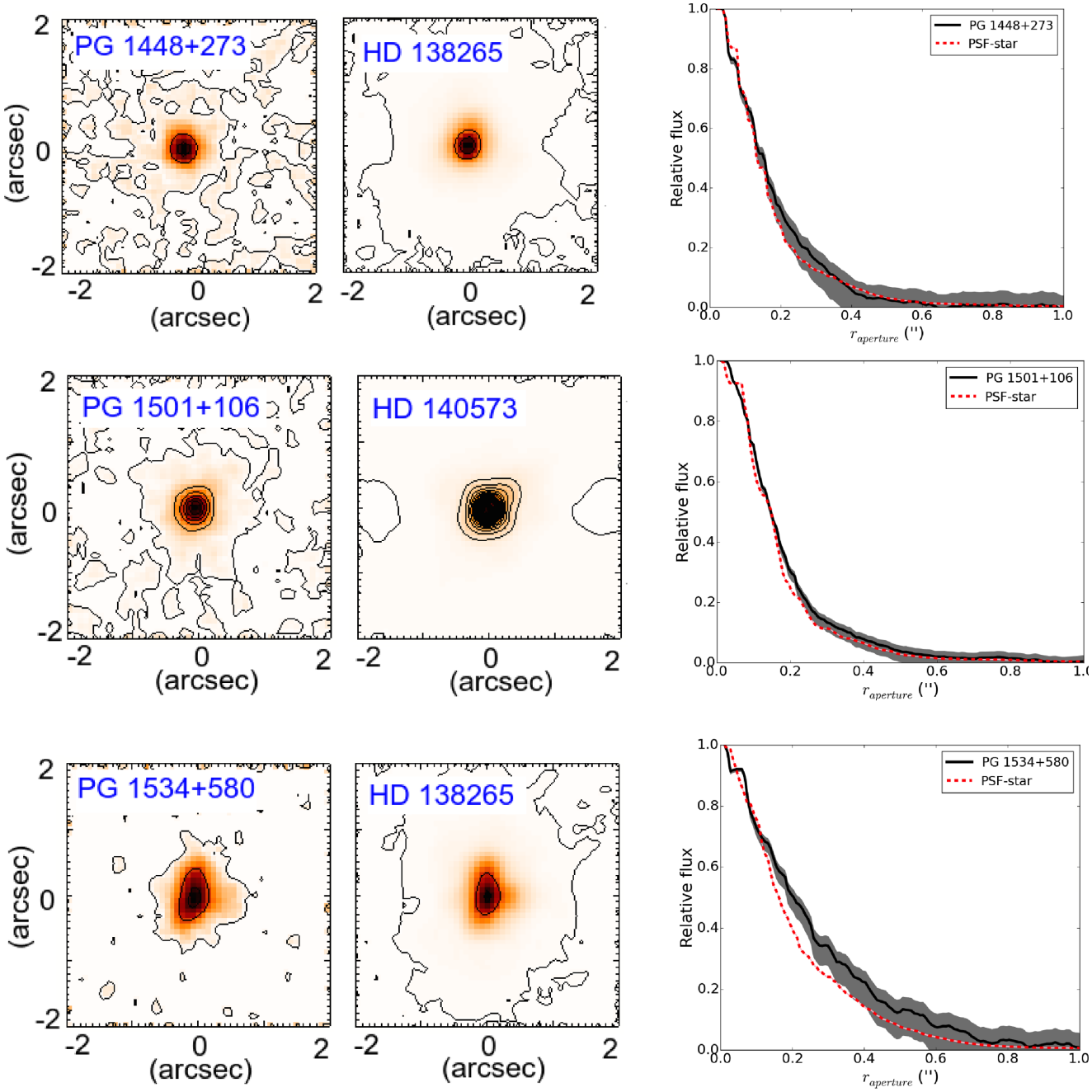

Figure B1 – *continued*

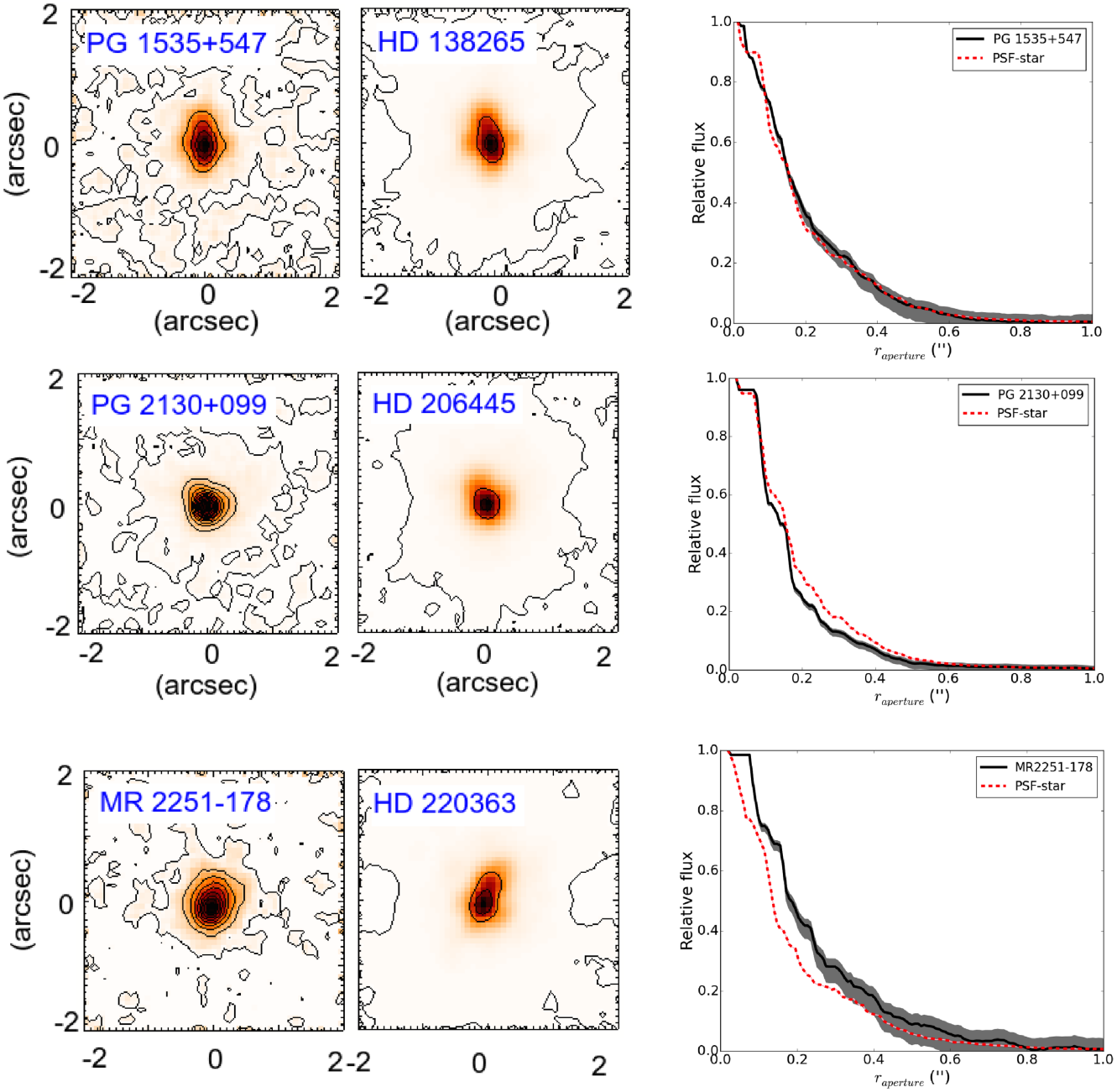

Figure B1 – *continued*

APPENDIX C: OBSERVED NIR TO MIR SEDS

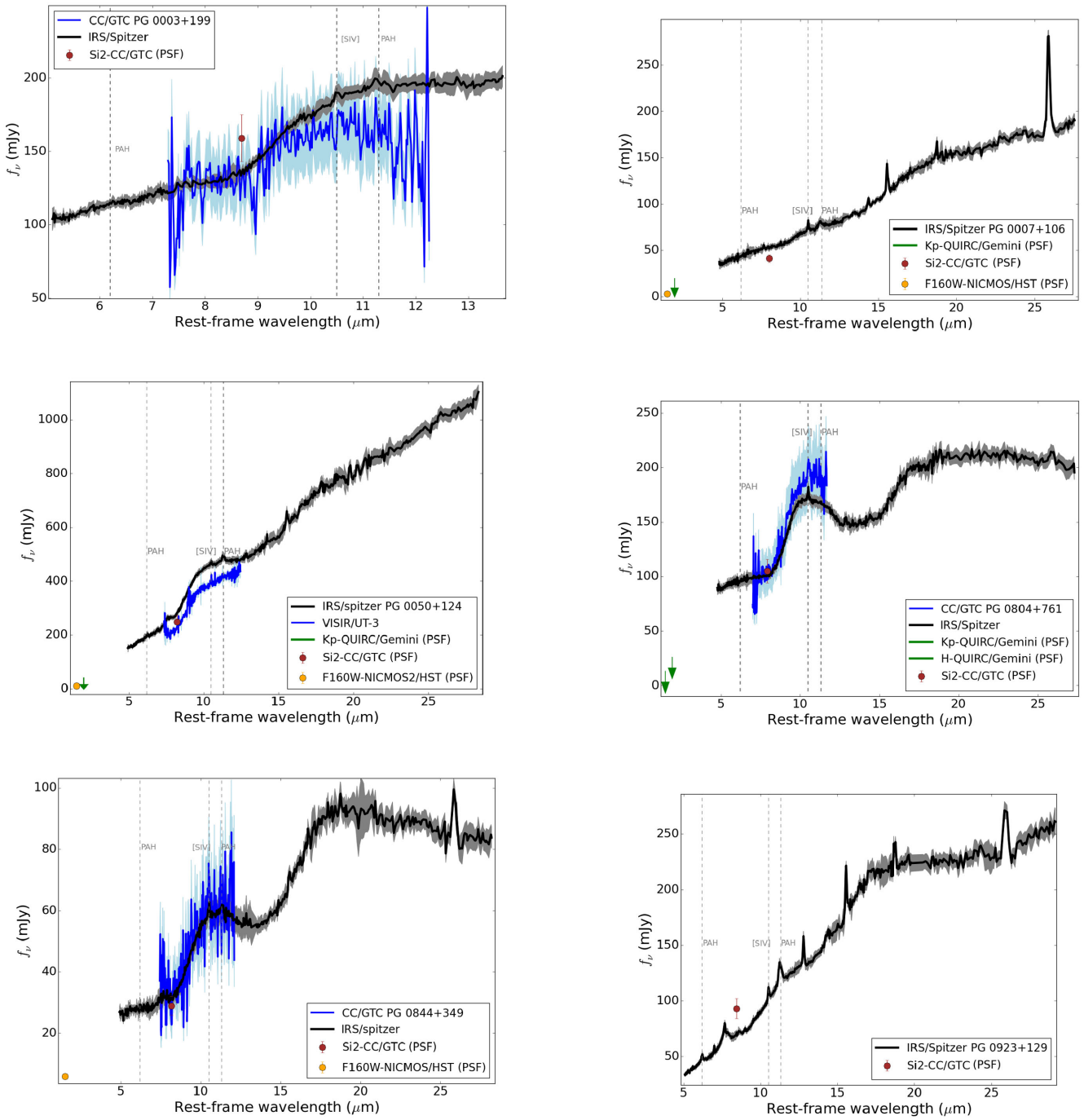

Figure C1. Spectra of the QSOs. The NIR unresolved emission from the literature is shown as orange points and green arrows, and the red point is the MIR unresolved emission reported in this work. In black is the *Spitzer/IRS* spectrum obtained from the CASSIS data base and in blue the CC spectrum at *N* band obtained by us. The 1σ uncertainty of the spectra is the corresponding shadow areas.

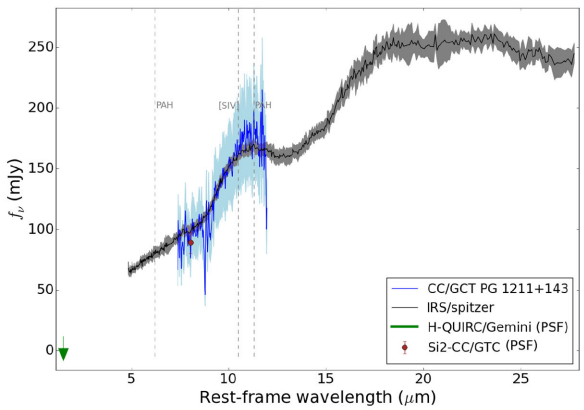

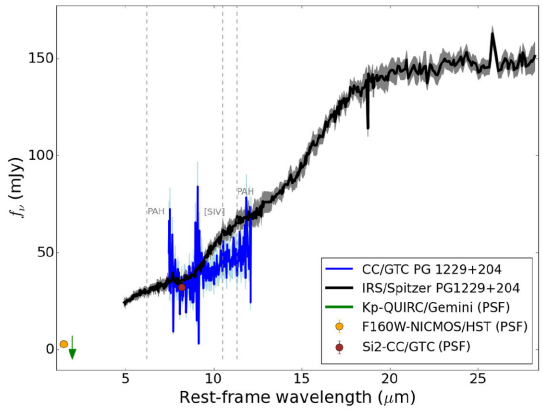

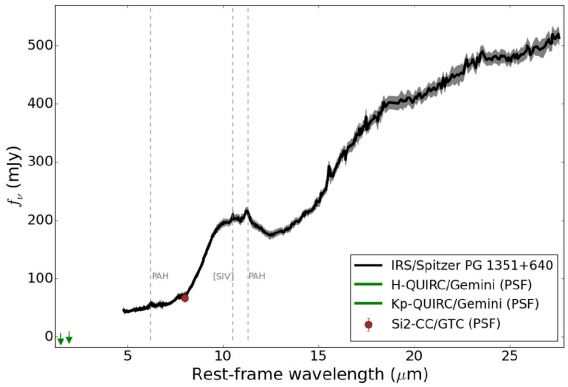

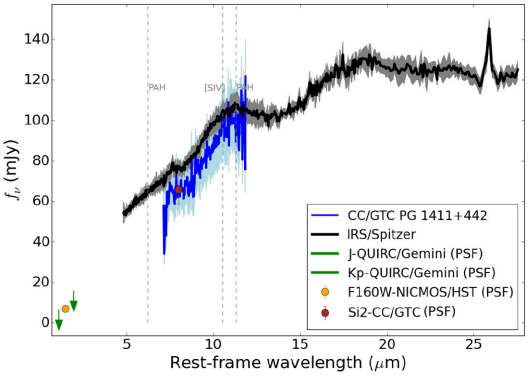

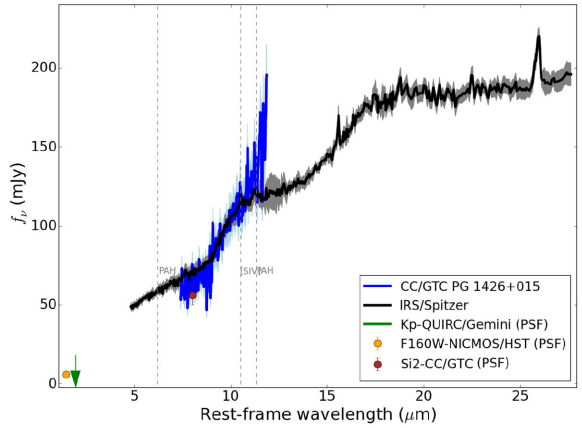

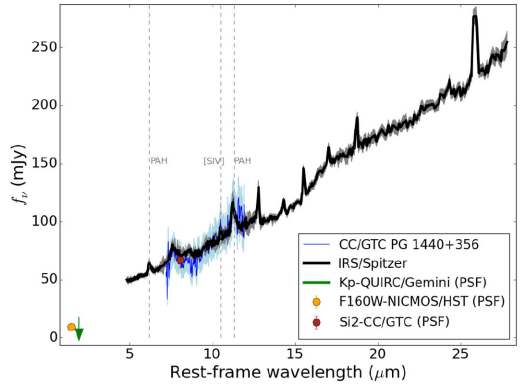

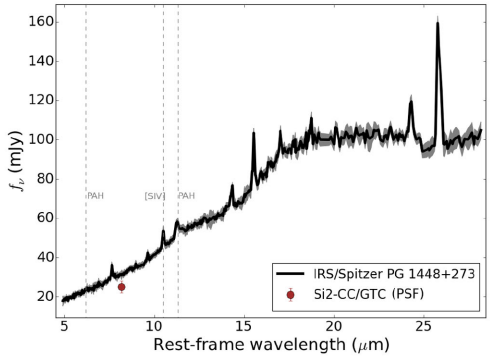

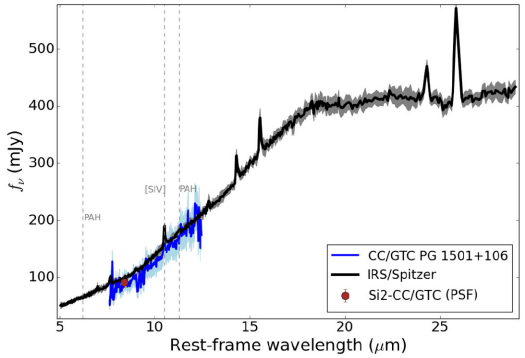

Figure C1 – *continued*

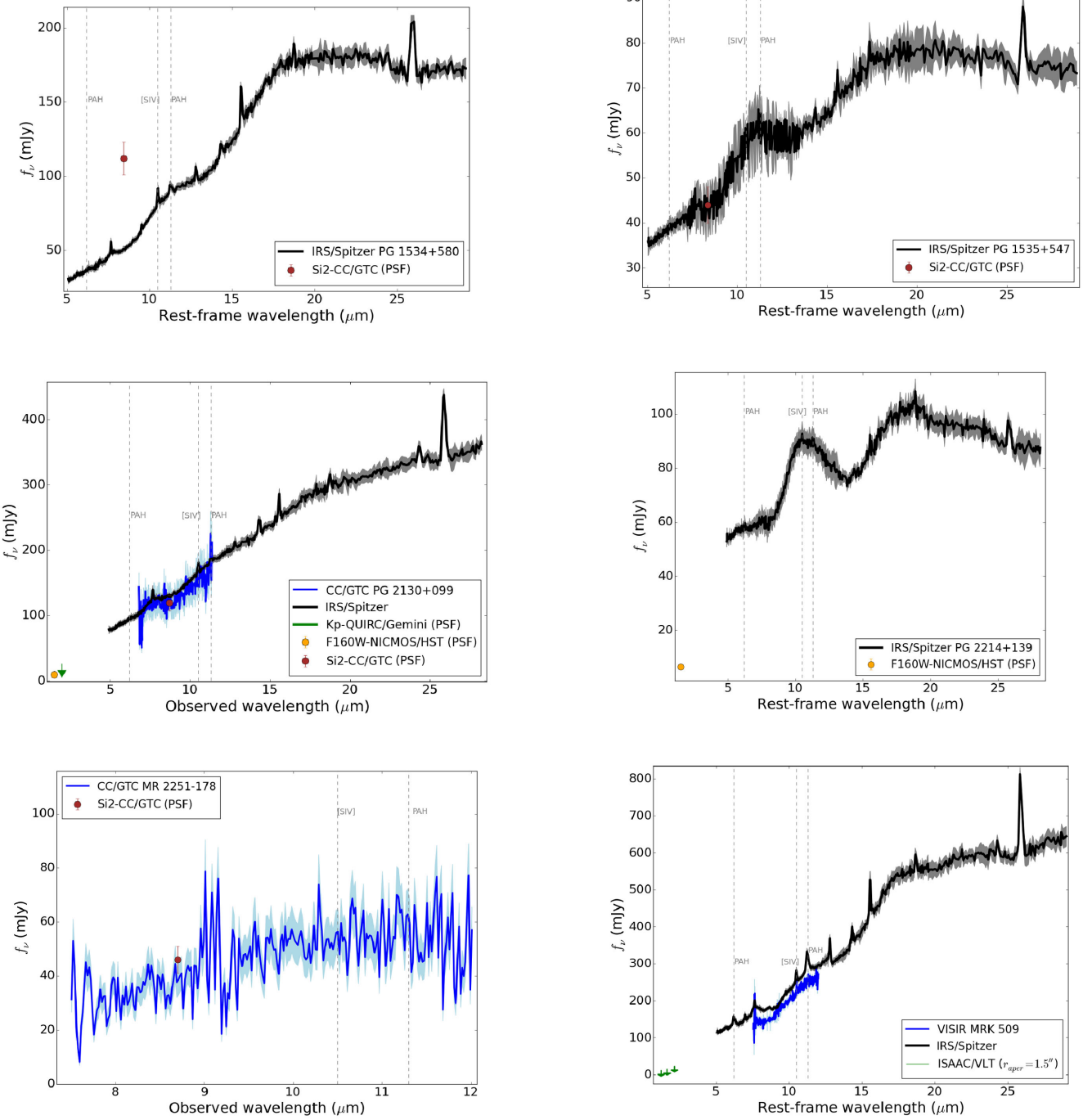

Figure C1 – *continued*

APPENDIX D: *SPITZER/IRS* SPECTRAL DECOMPOSITION

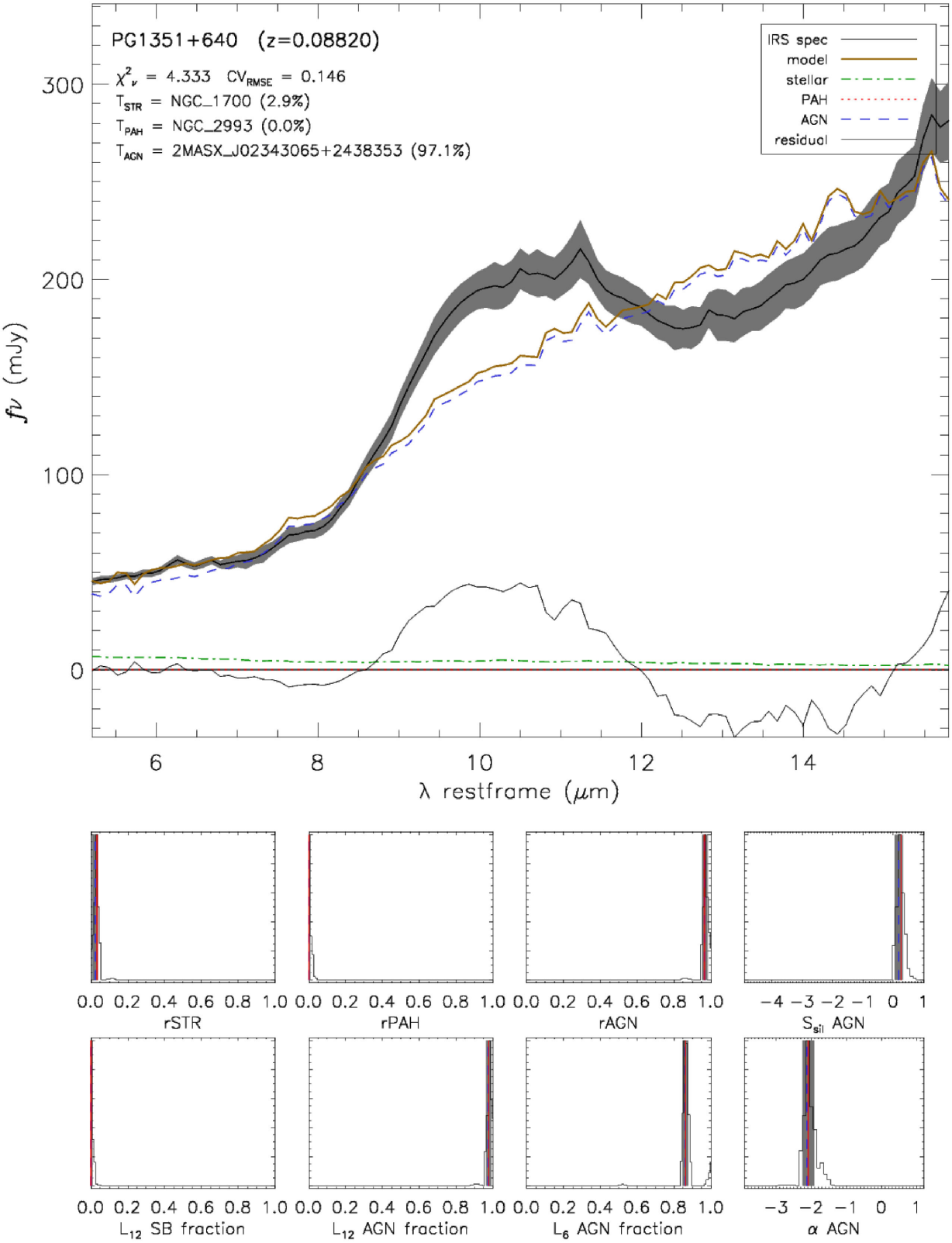

Figure D1. PG 1351+640: as in Fig. 5. Due to the prominent emission of the silicate at 9.7 μm the spectrum cannot be reproduced by the spectral decomposition method.

APPENDIX E: MODELED SPECTRAL ENERGY DISTRIBUTIONS

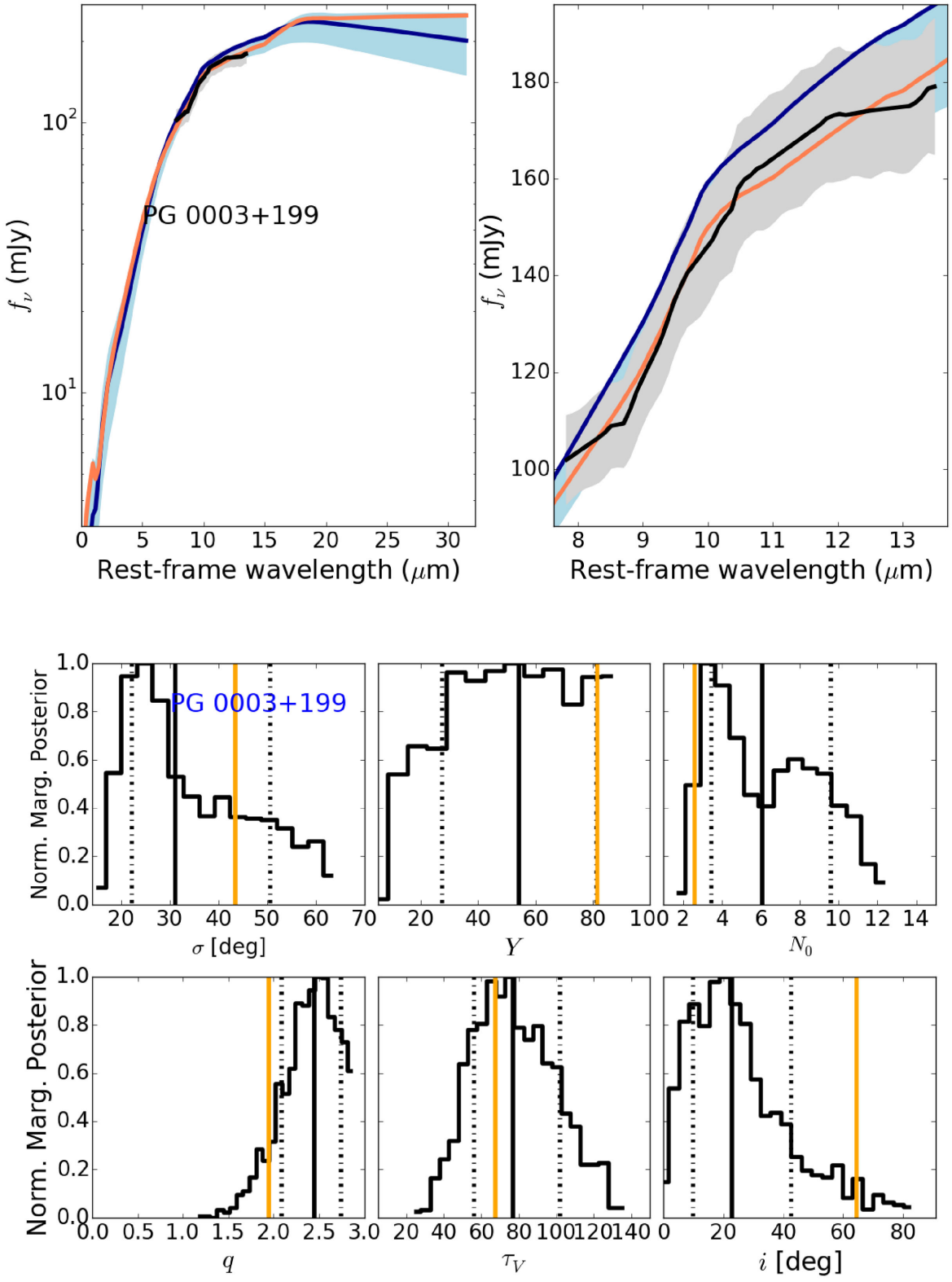

Figure E1. Upper panels: as in Fig. 8. Middle and lower panels: as in Fig. 9.

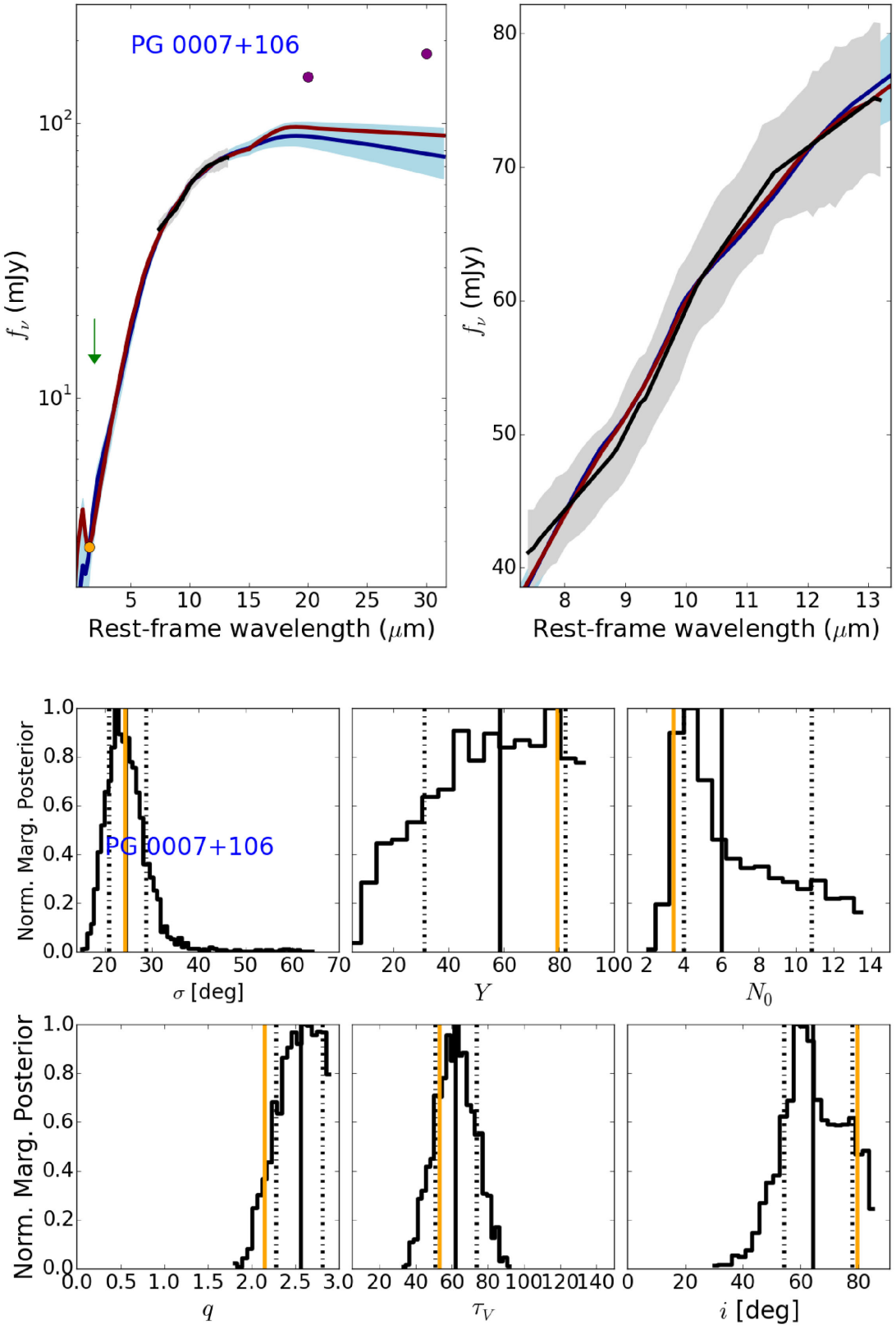

Figure E1 – *continued*

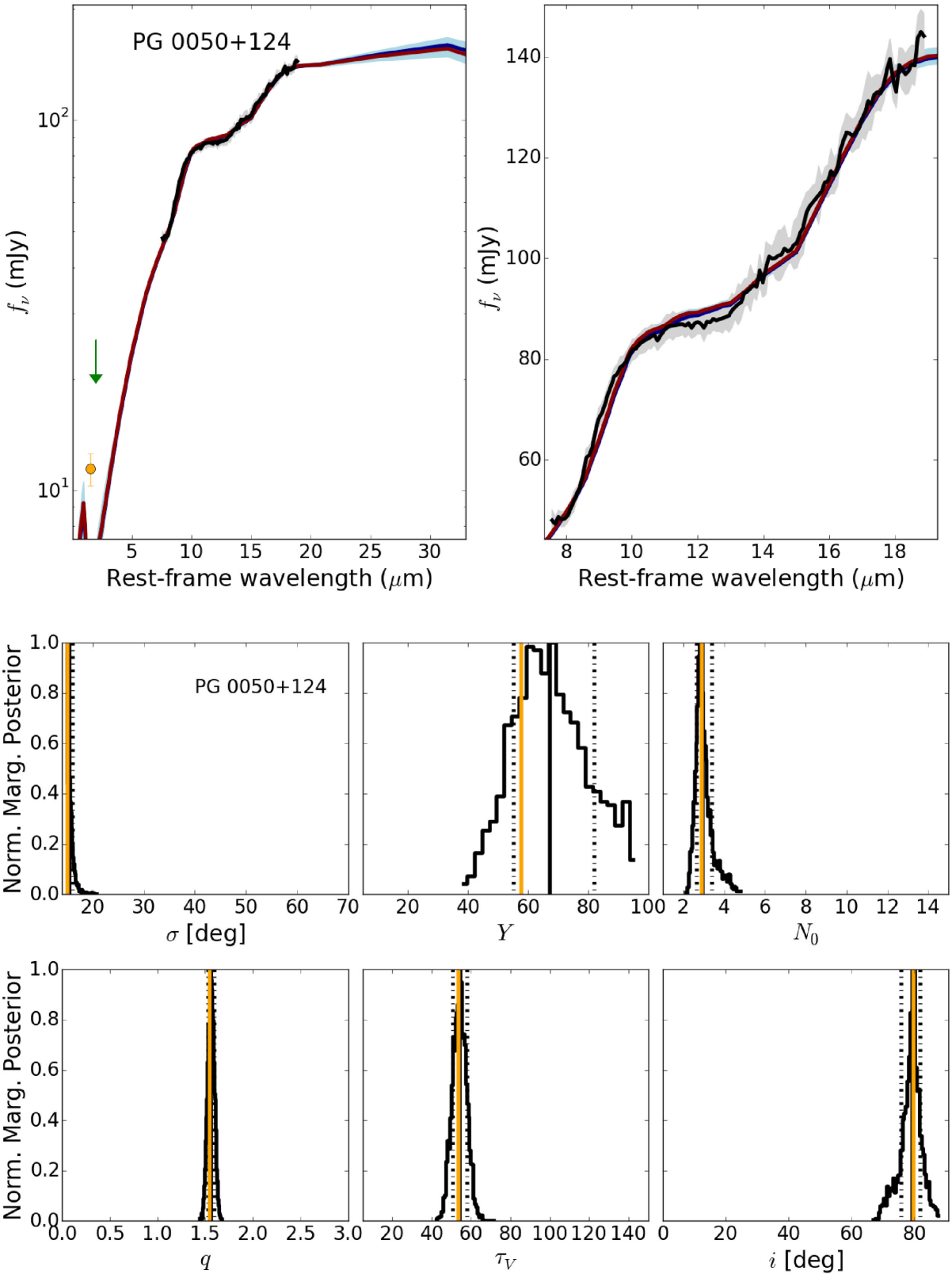

Figure E1 – *continued*

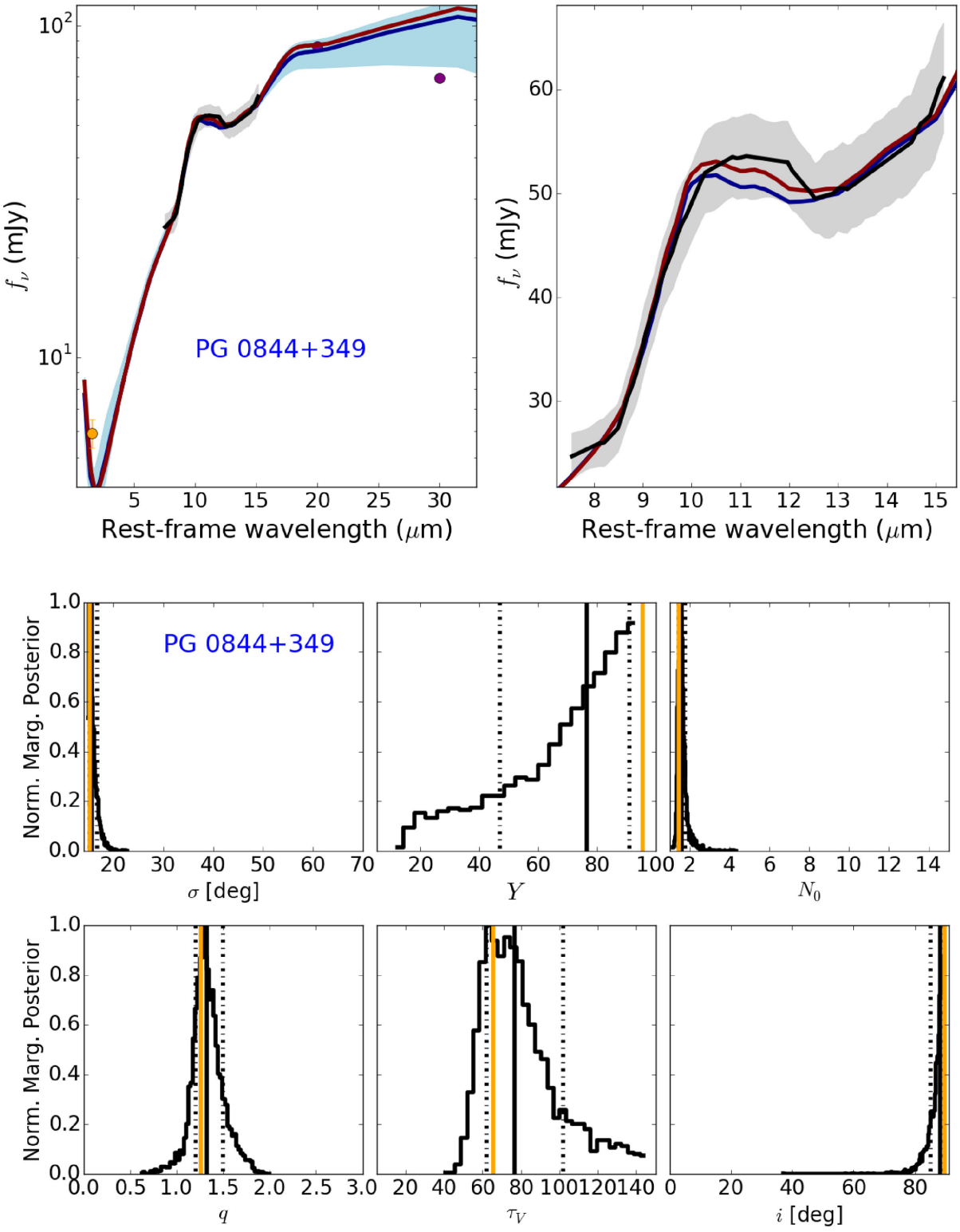

Figure E1 – *continued*

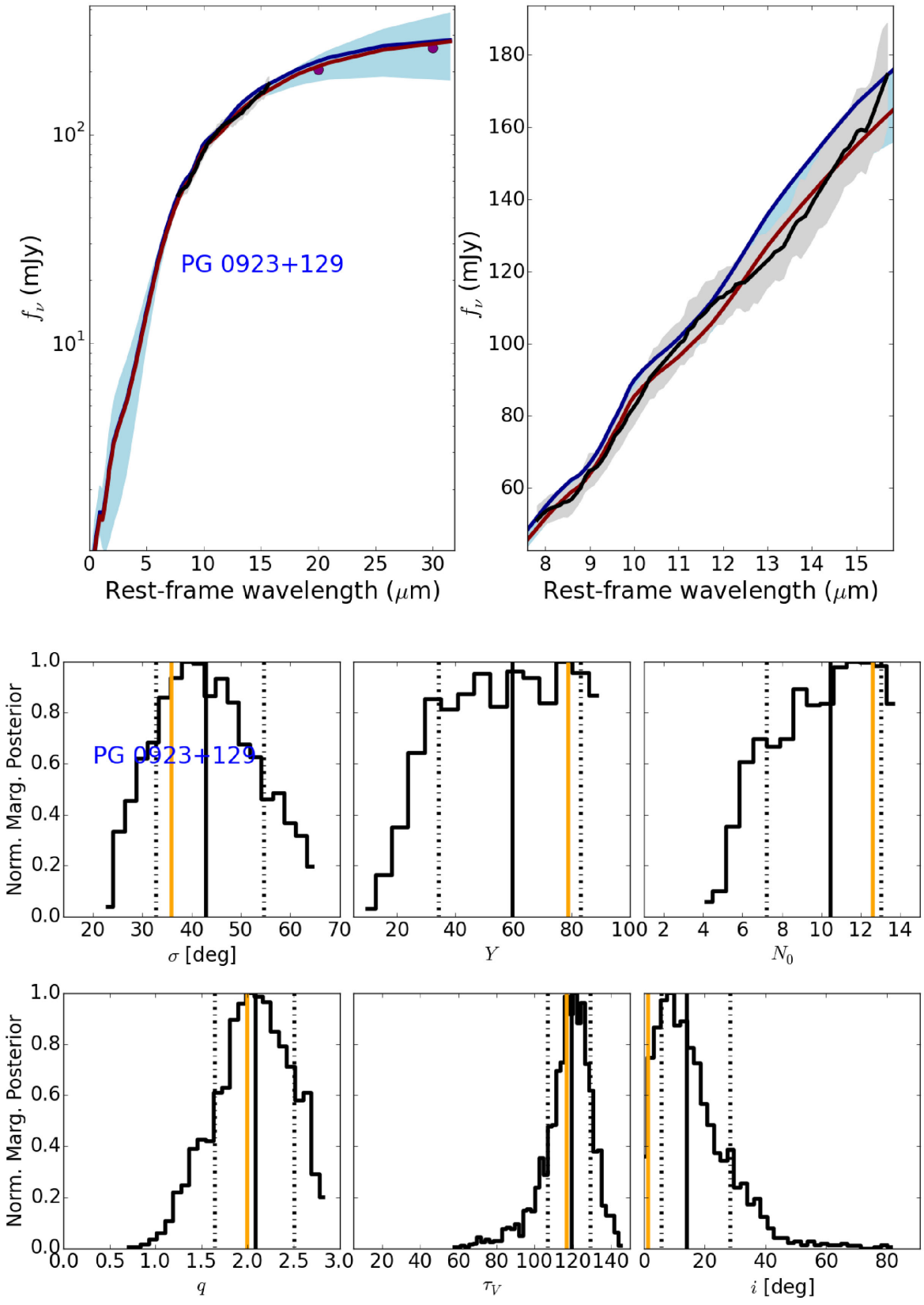

Figure E1 – *continued*

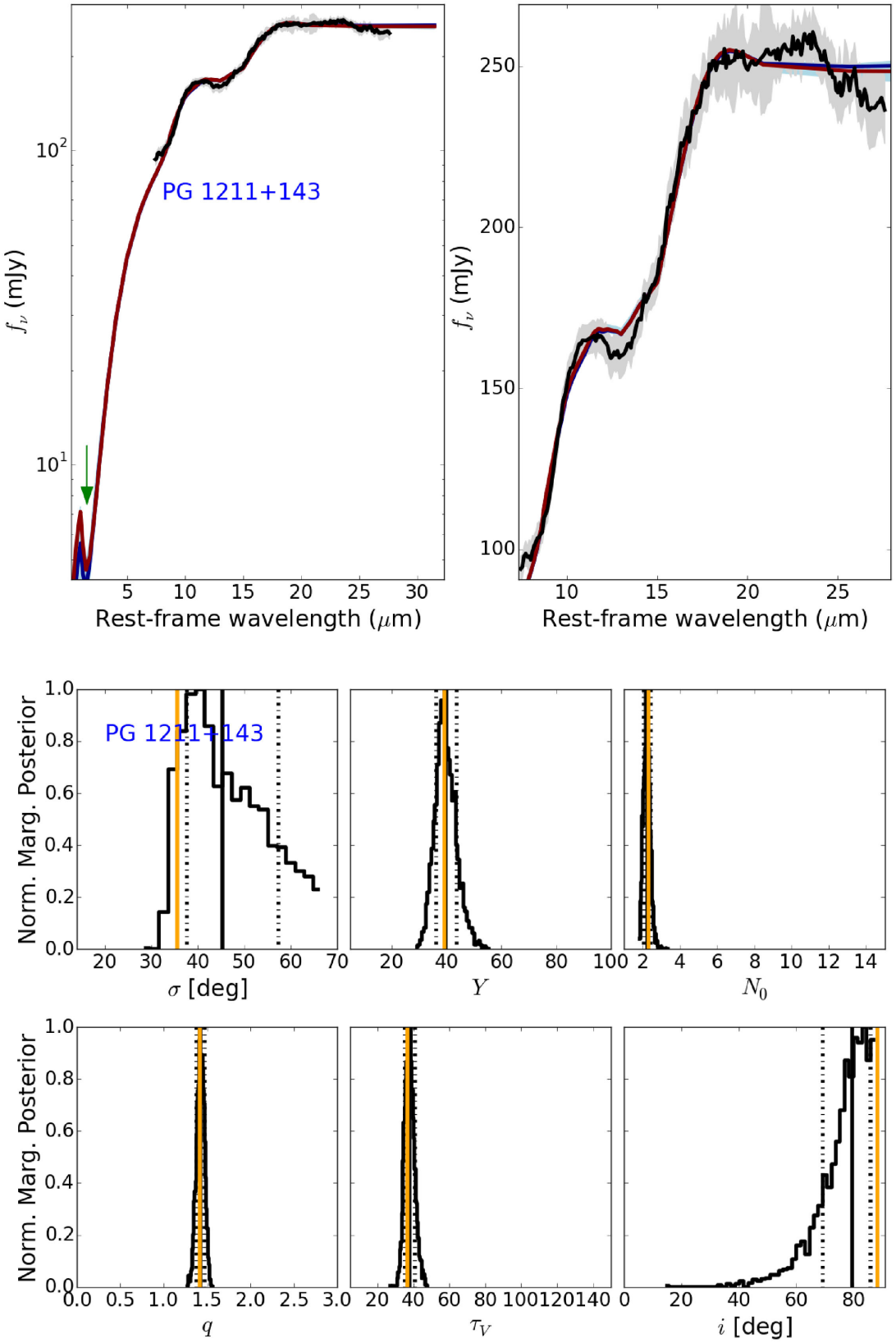

Figure E1 – *continued*

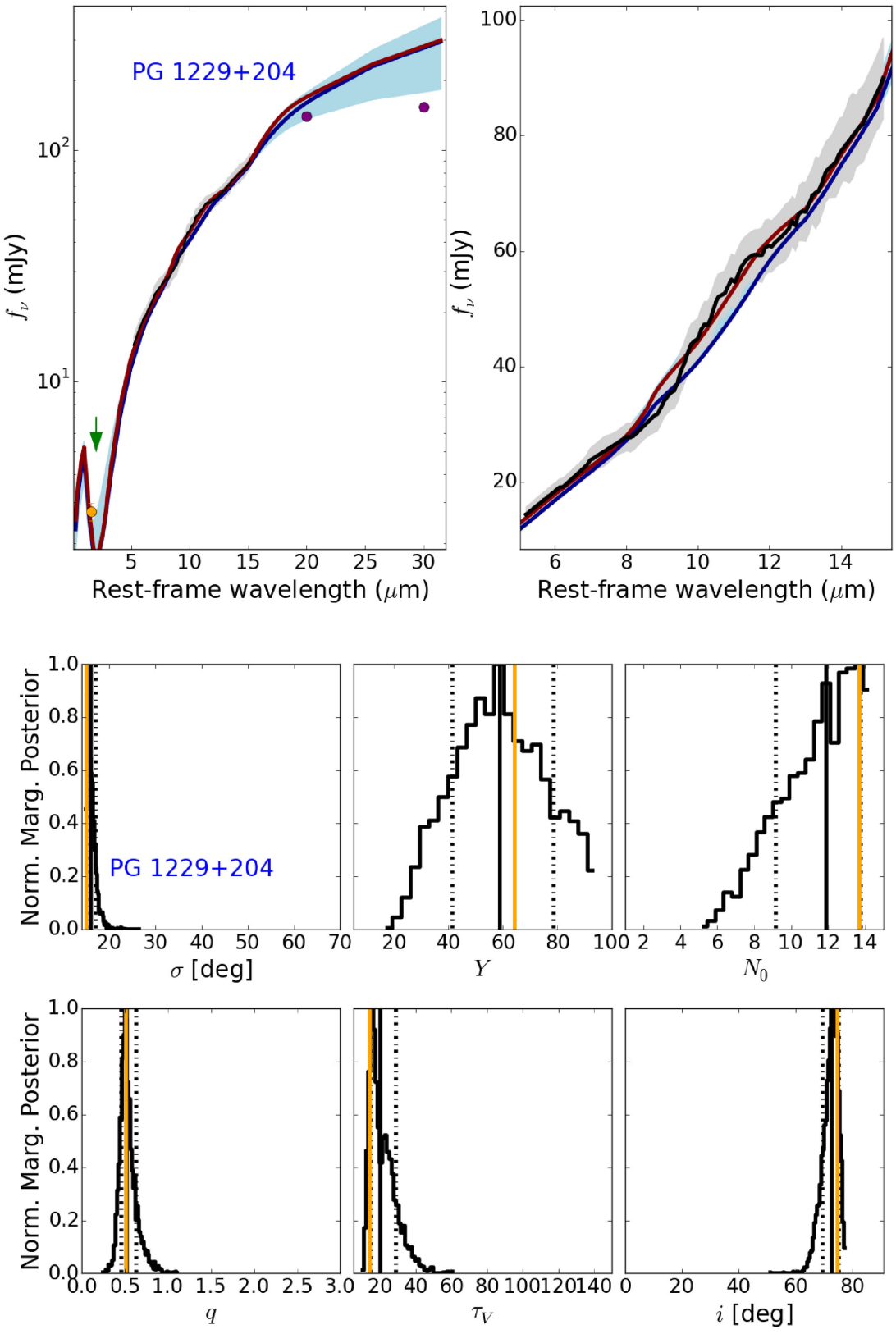

Figure E1 – *continued*

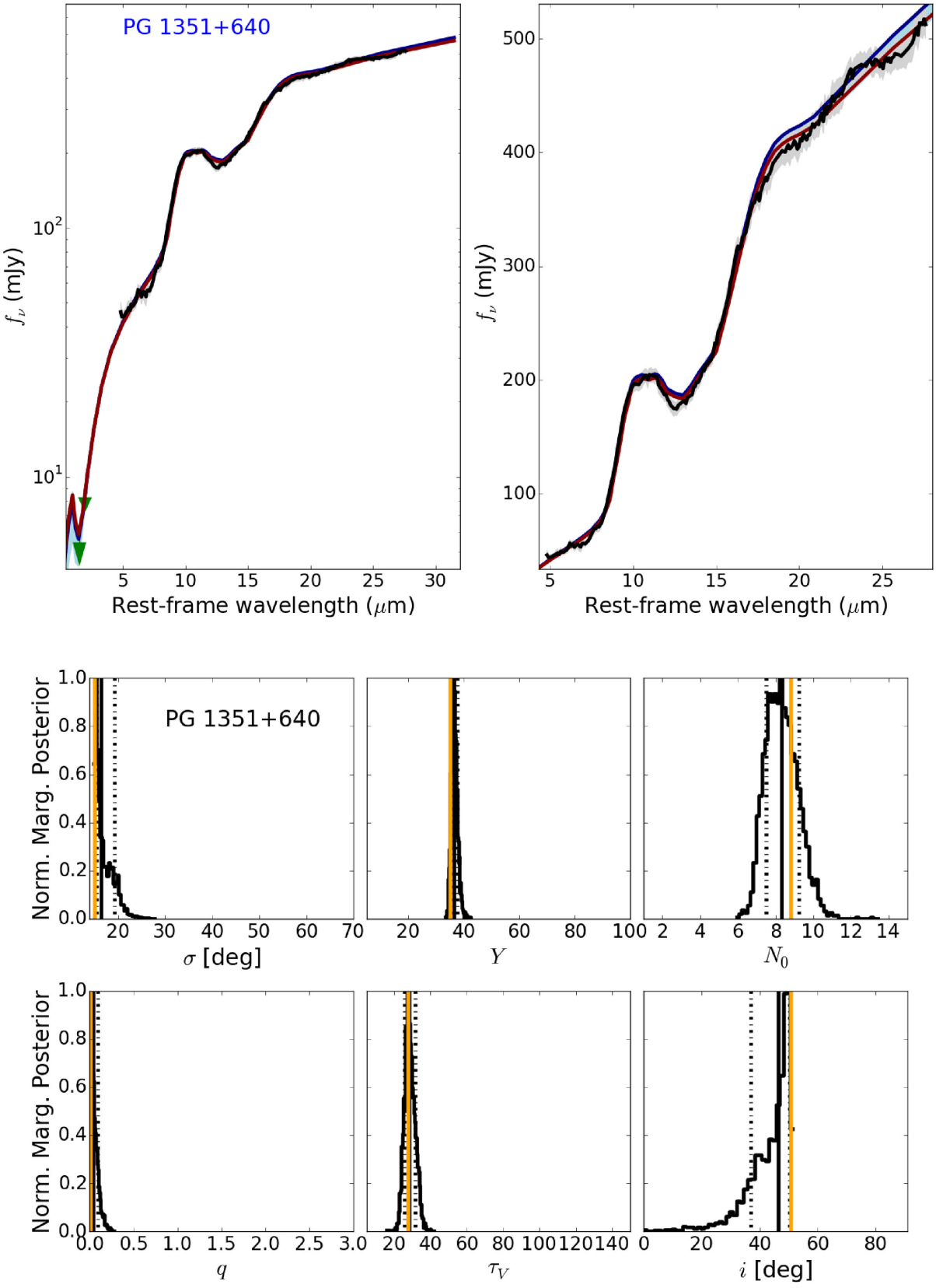

Figure E1 – *continued*

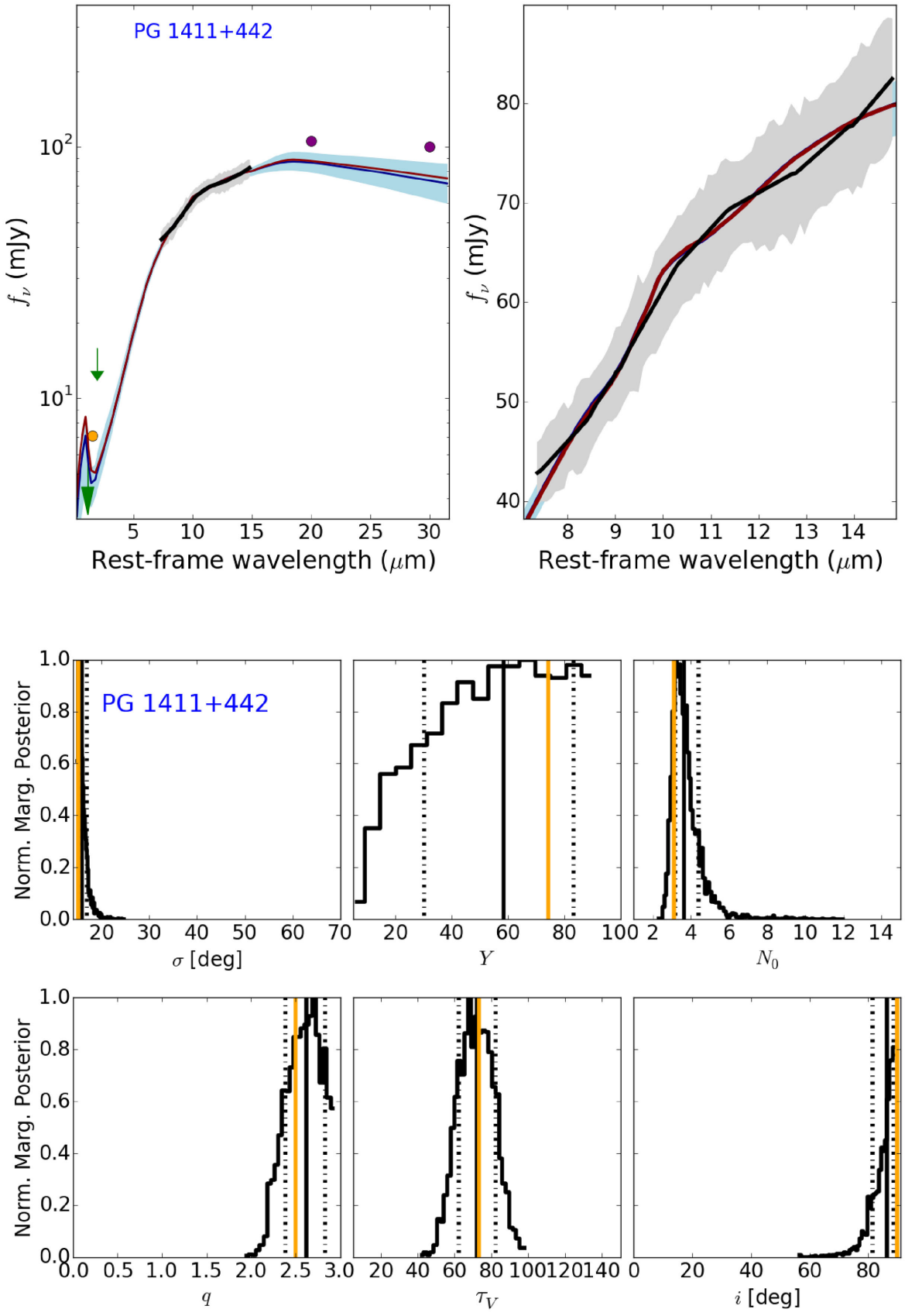

Figure E1 – *continued*

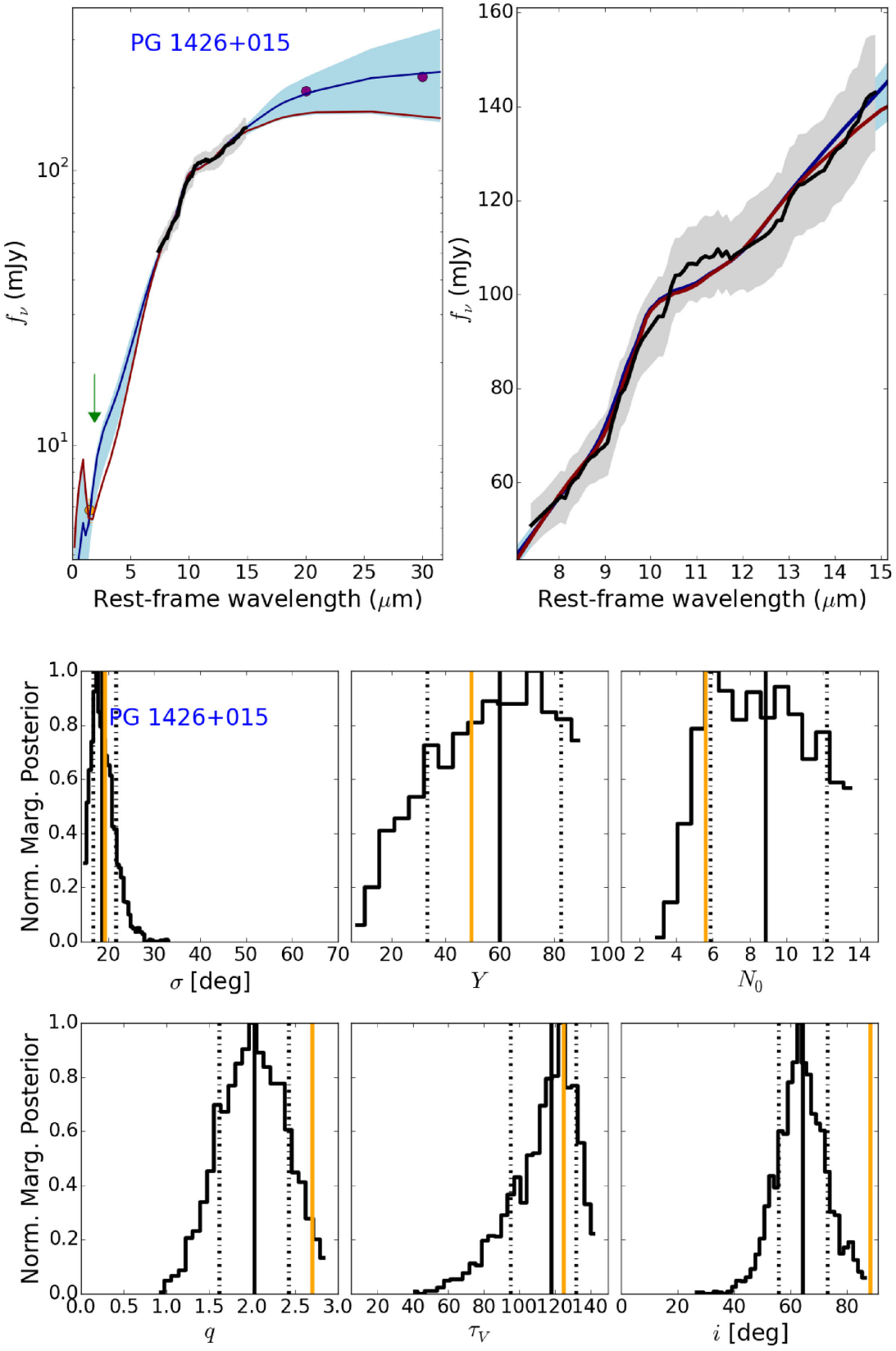

Figure E1 – *continued*

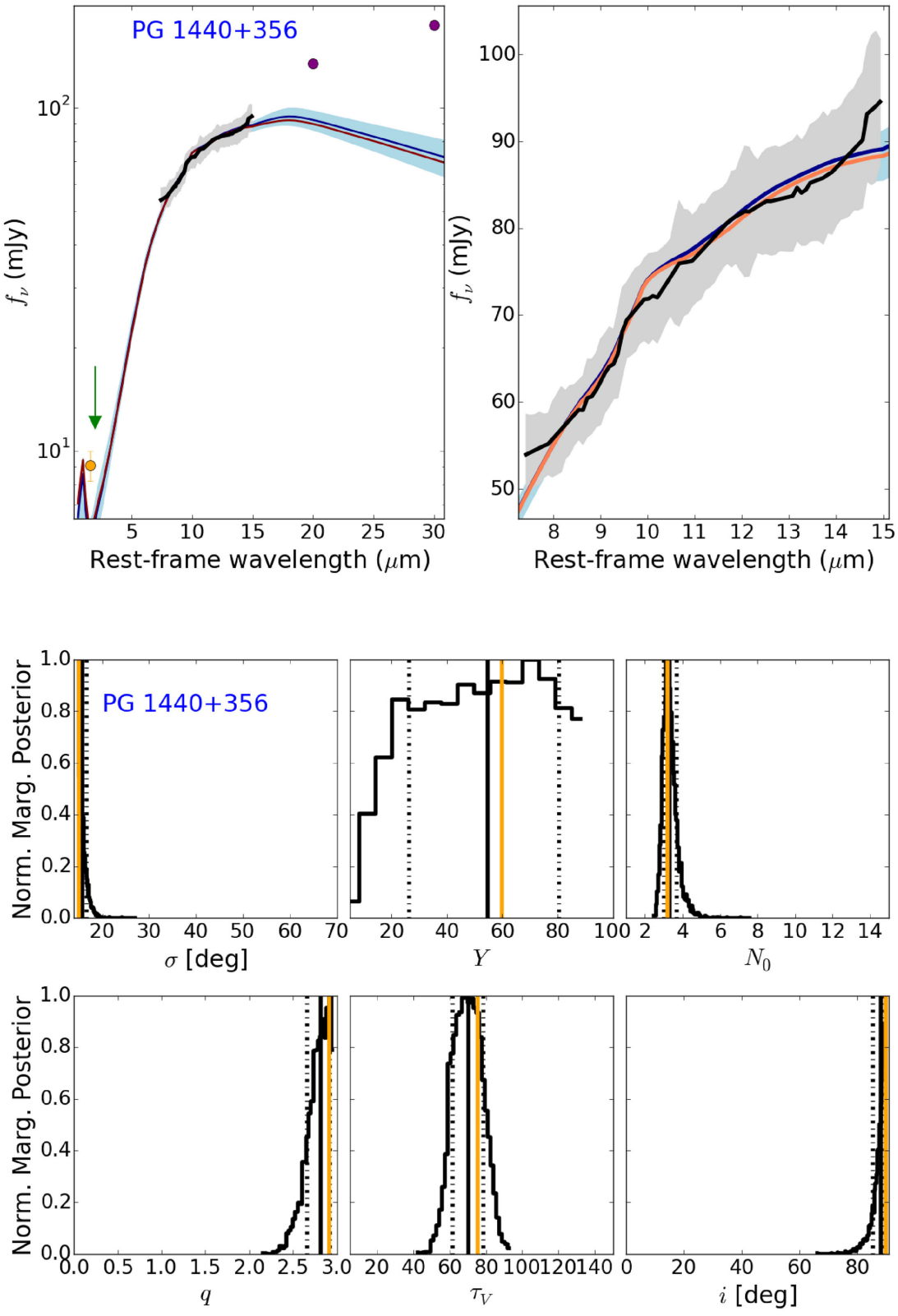

Figure E1 – *continued*

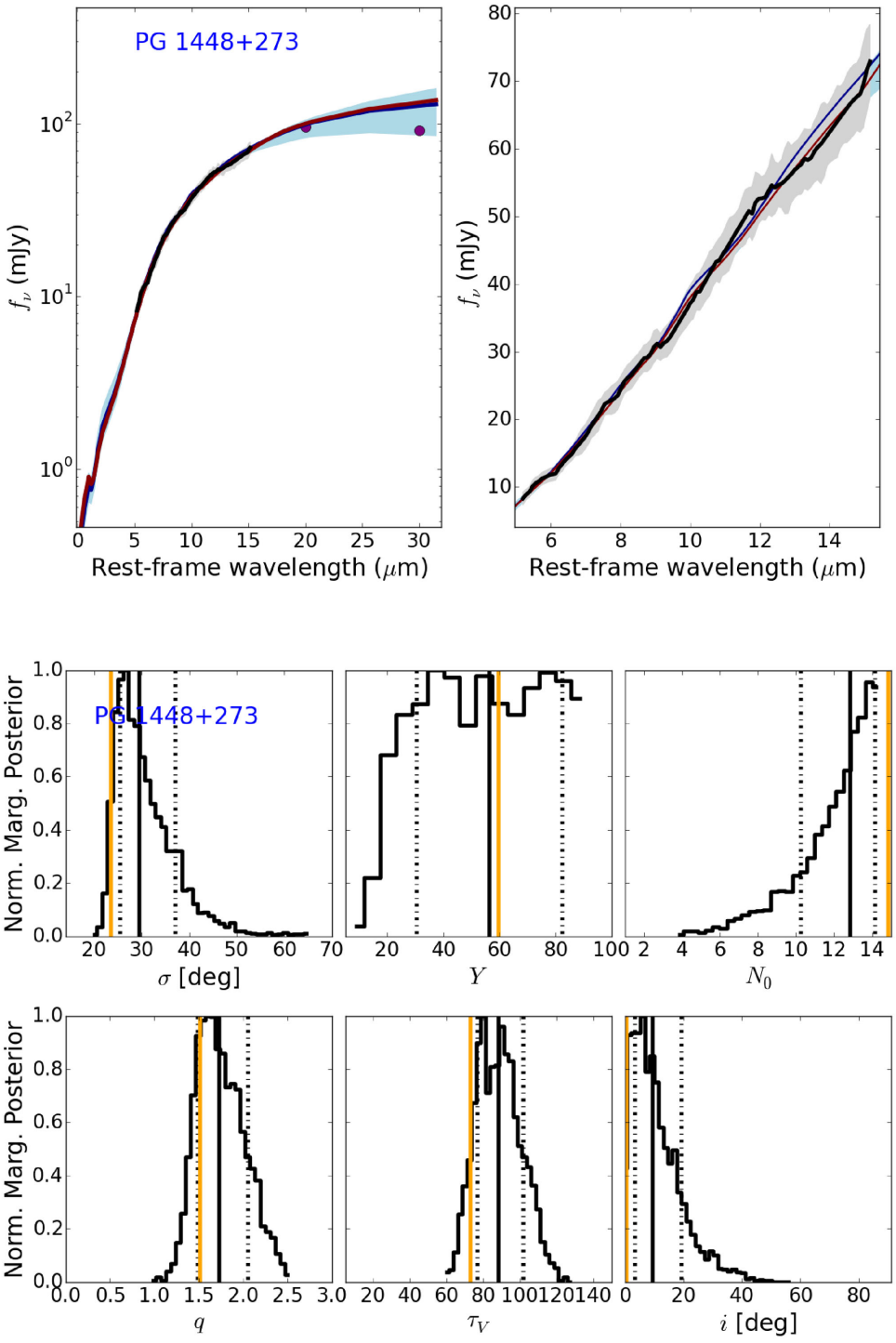

Figure E1 – *continued*

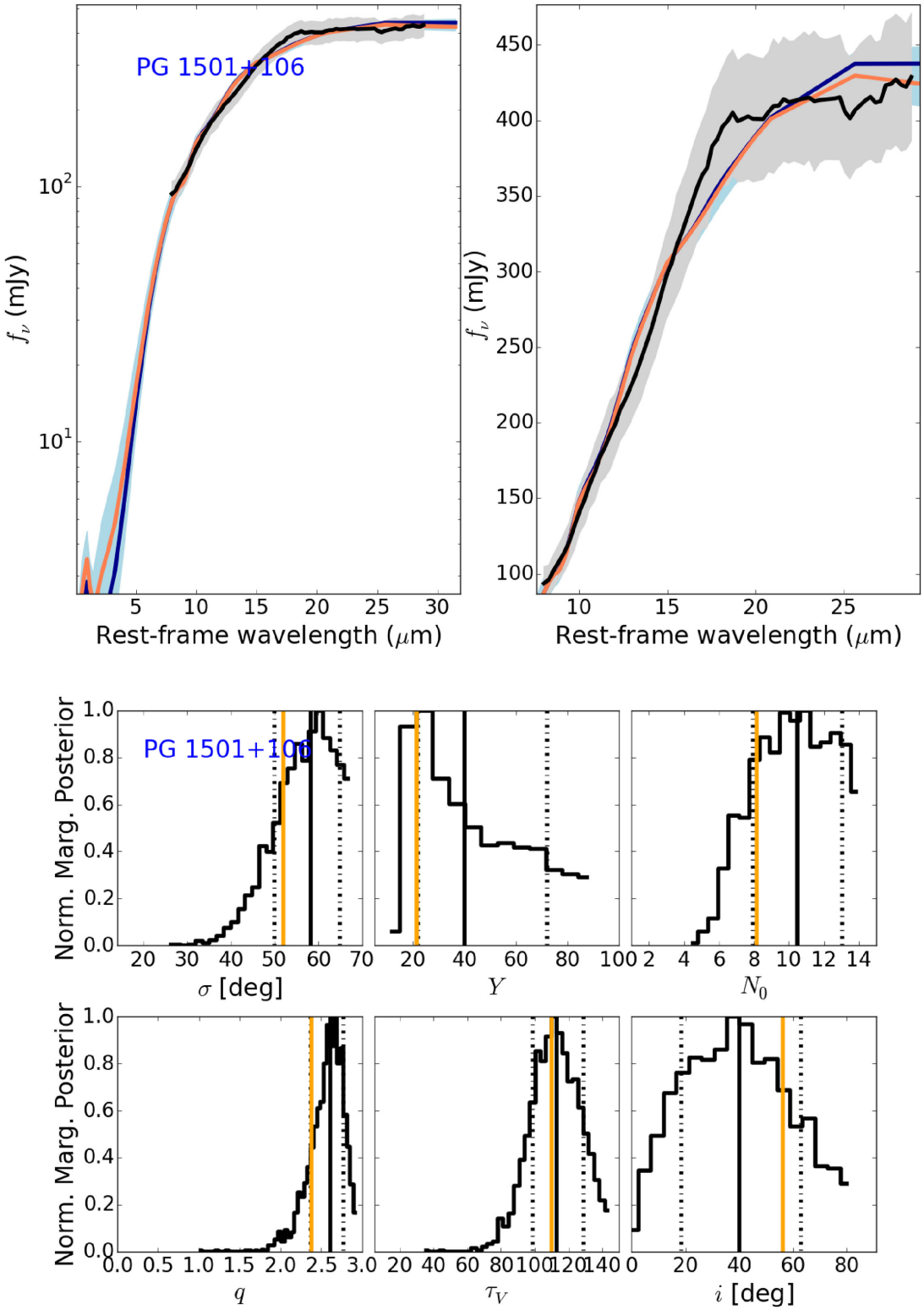

Figure E1 – *continued*

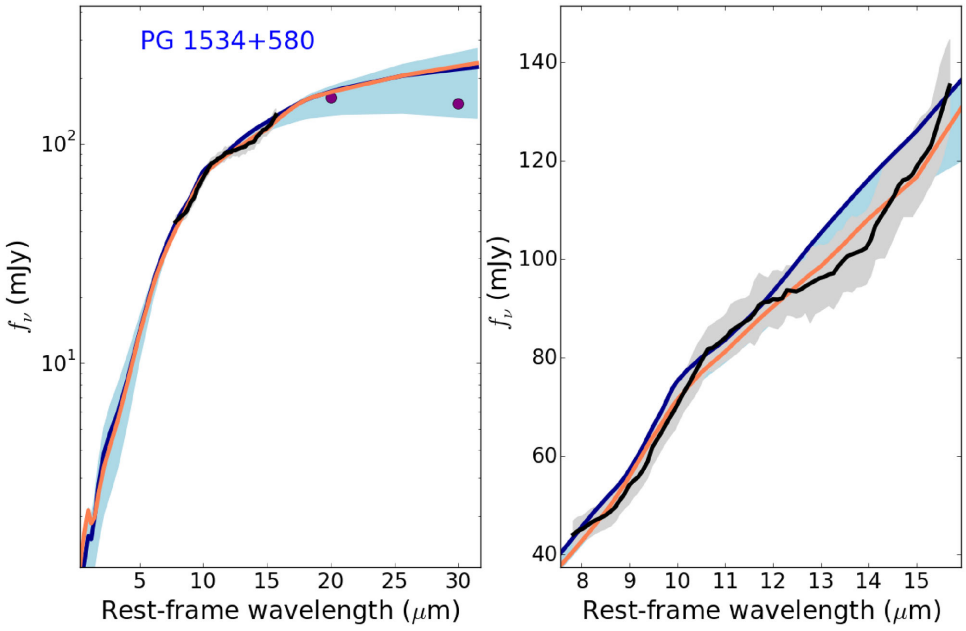

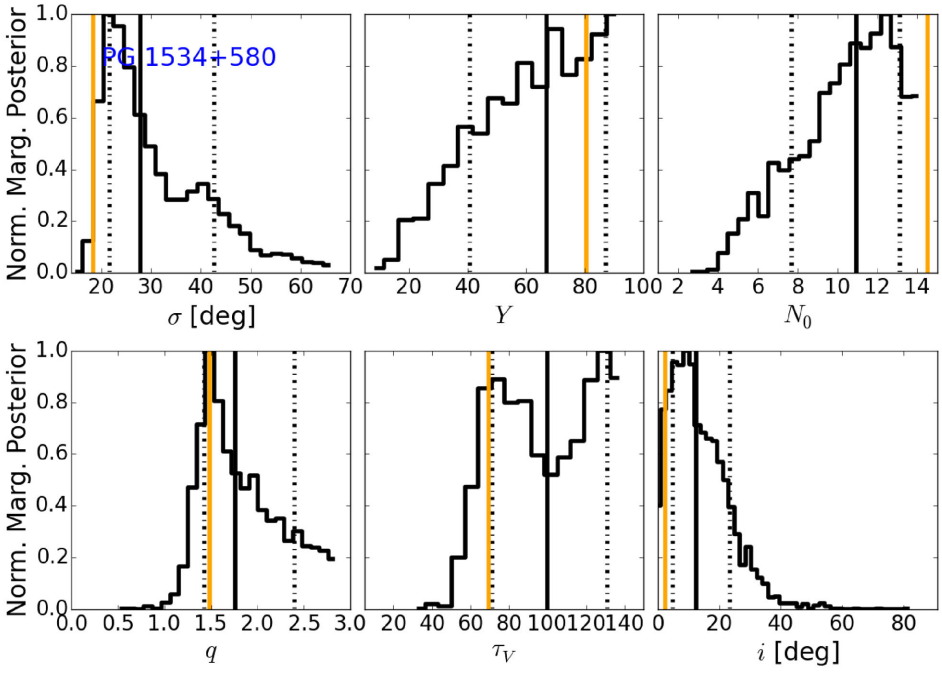

Figure E1 – *continued*

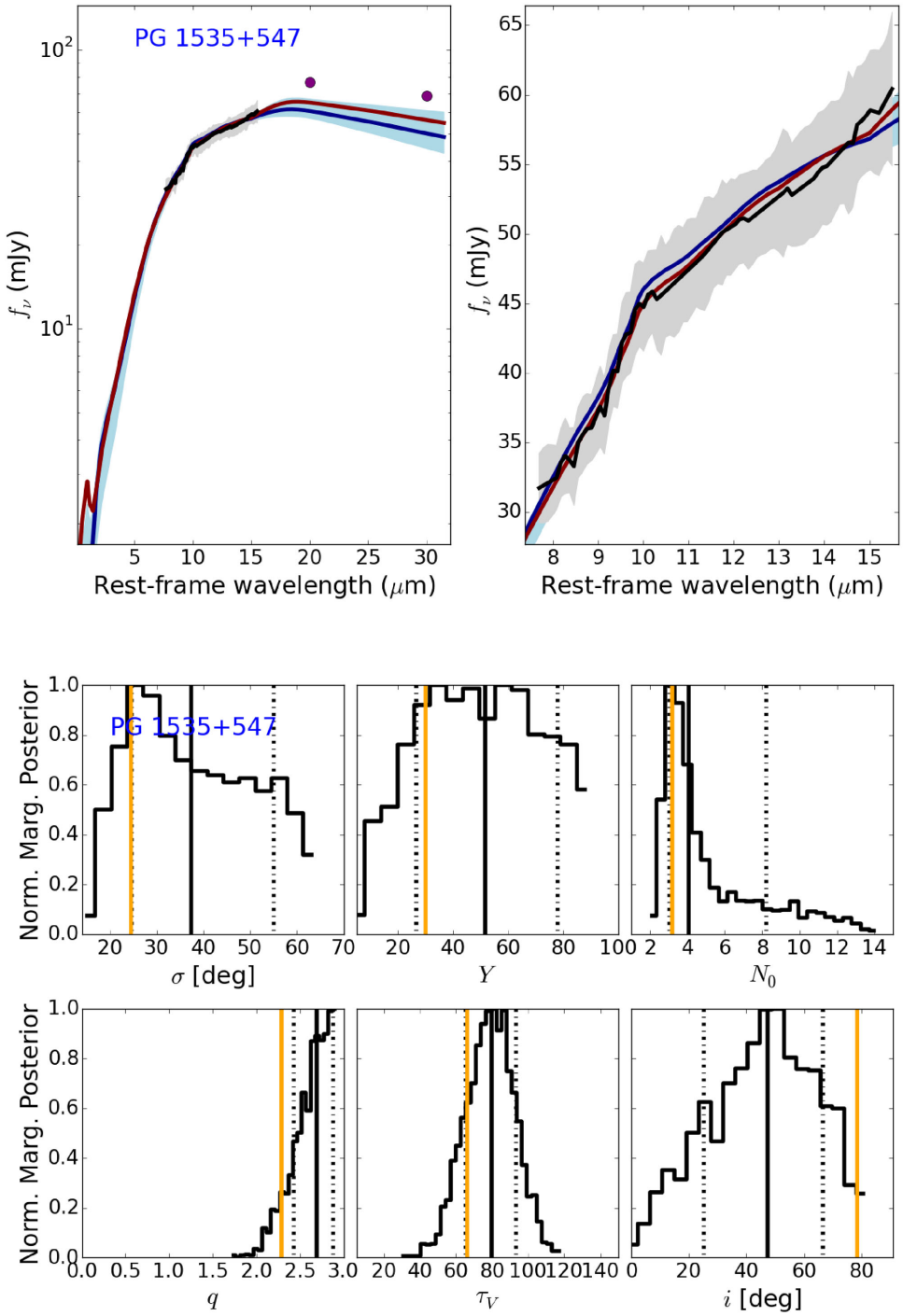

Figure E1 – *continued*

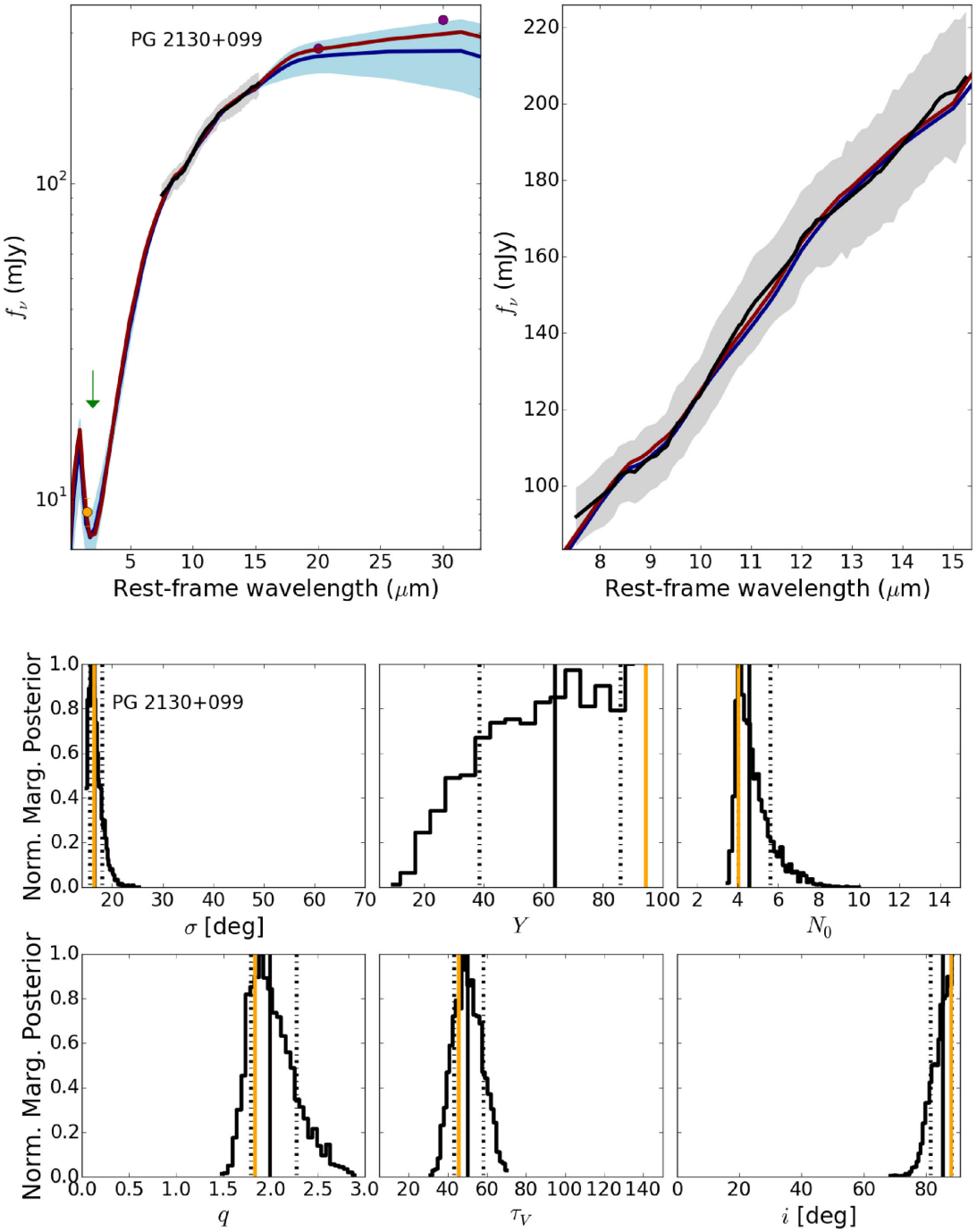

Figure E1 – *continued*

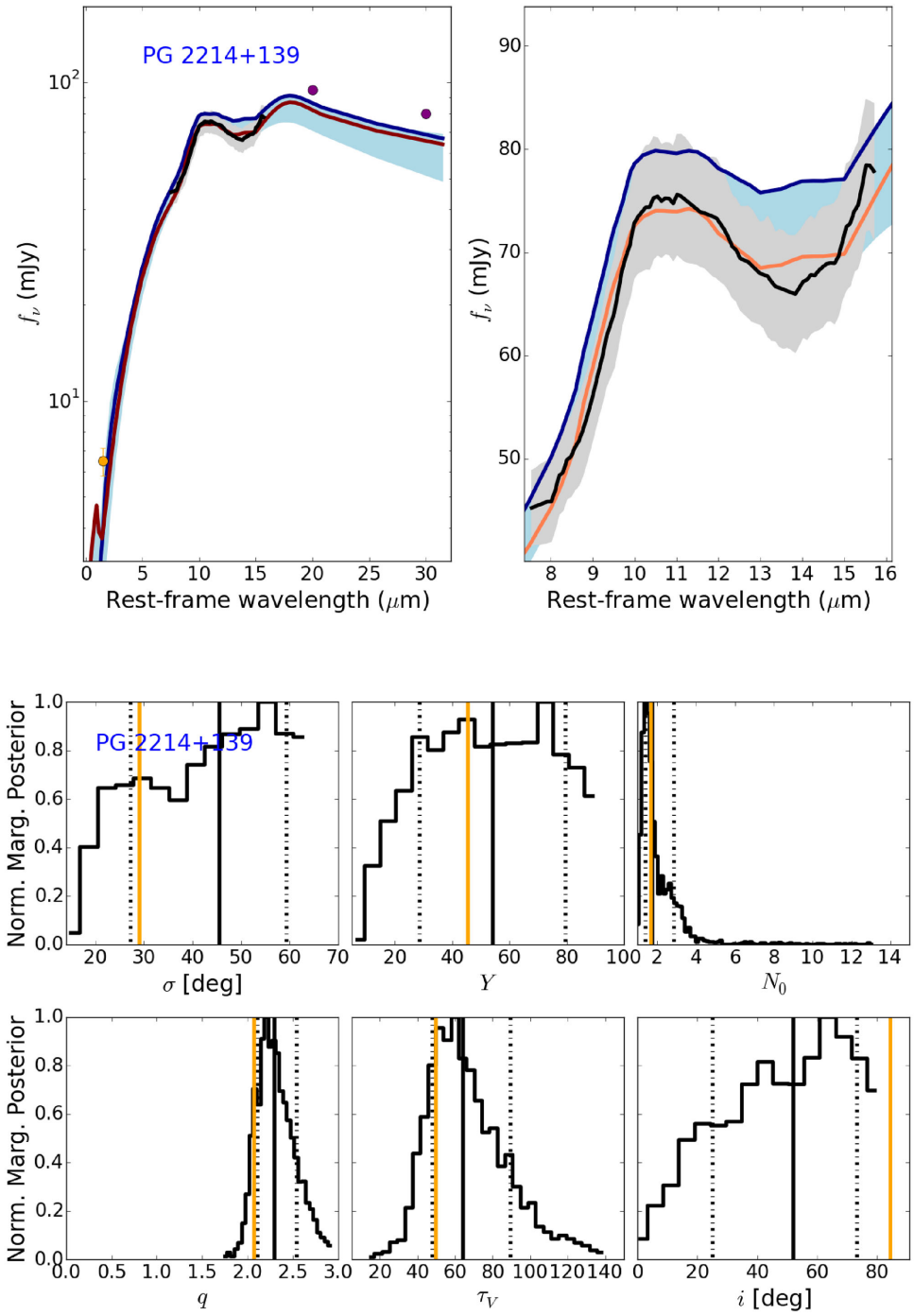

Figure E1 – *continued*

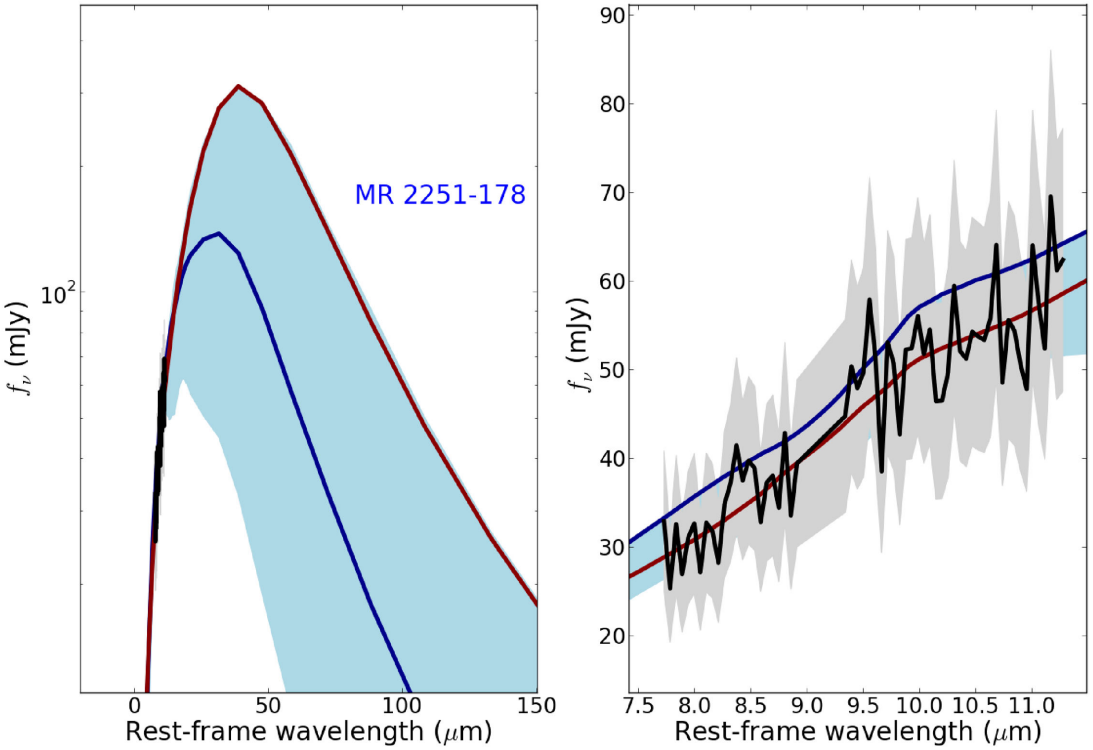

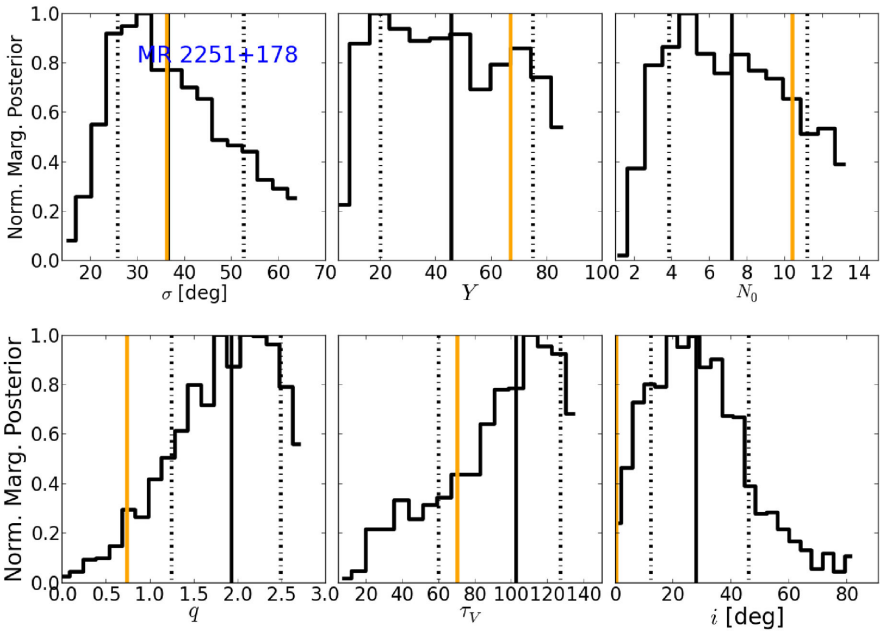

Figure E1 – *continued*

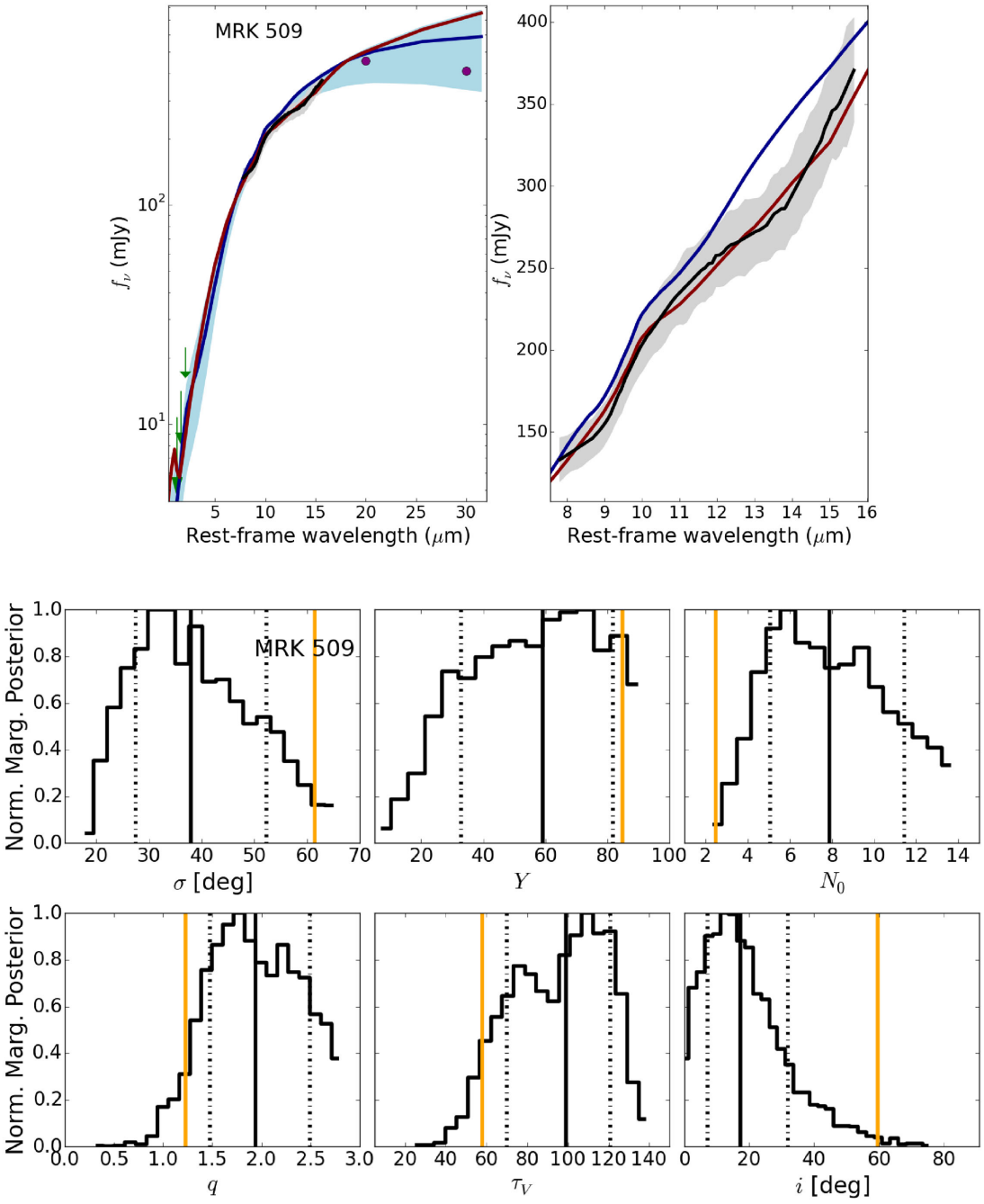

Figure E1 – *continued*

This paper has been typeset from a TEX/LATEX file prepared by the author.